Doctoral thesis submitted in partial fulfillment of the requirements for the degree of Doctor in Physics

A complex networks perspective of the past and future coupling between the tropical oceans and precipitation over Southeastern South America

A dissertation by: Verónica Martín Gómez

Advisor: Marcelo Barreiro

Instituto de Física, Facultad de Ciencias

Universidad de la República, Montevideo, Uruguay

February, 2017

Signatures:

Verónica Martín Gómez	Marcelo Barreiro

ABSTRACT

A complex network perspective of the past and future coupling between the tropical oceans and precipitation over Southeastern South America

Sea surface temperature (SST) anomalies over the tropical oceans generate extratropical atmospheric circulation anomalies that can induce rainfall variability and changes in the moisture sources over these regions. Several previous studies have shown that Southeastern South America (SESA) is impacted by SST anomalies in the tropical Pacific, Atlantic and Indian oceans. In addition, these tropical oceans can interact with each other inducing SST anomalies in remote basins through atmospheric and oceanic teleconnections. However, nowadays it is not clear: (1) how SST anomalies over the tropical oceans can collectively interact with each other and, in turn, induce rainfall variability over SESA, (2) how this collective interaction could change during the next century as consequence of an anthropogenic forcing, and (3) how moisture sources of SESA could change considering different periods in terms of the degree of collective interaction among the tropical oceans and SESA precipitation.

We address these issues from a complex network perspective. We construct a climate network considering different indices that characterize the tropical oceans and a precipitation index over SESA as network's nodes. We investigate their collective interaction focusing on the detection of synchronization periods, which are defined through the mean network distance and can be understood as those periods of time in which the network's nodes are most connected with each other.

Results show that during the last century there were two synchronization periods characterized by different interactions among the network's nodes (30s and 70s). Moreover, an analysis of the network behavior under a global warming scenario suggests that an anthropogenic forcing would increase the number of synchronization periods per century, their time length, and the nodes connectivity. The stronger connectivity of SESA precipitation would suggest an increase of the tropical ocean's influence on rainfall over SESA as result of anthropogenic forcing, which could enhance its seasonal predictability. These results are based on the grand ensemble mean of seven CMIP5 (Coupled Model Intercomparison Project Phase 5) models and should be taken with caution because of the large disparity in individual model behavior.

Finally, an analysis of the moisture sources during summertime suggests that the main sources of SESA rainfall are the regional recycling, the central-eastern shore of Brazil together with the surrounding Atlantic ocean, and the southwestern South Atlantic surrounding the SESA domain. A comparison of SESA moisture sources during a non-synchronized period with another synchronized one shows that the principal differences are in the intensity of the recycling and in the strength of the central-eastern shore of Brazil. Moreover, it is also found that the region centered at (20ºS, 300ºE), close to the core of the Low Level Jet, is a moisture source of SESA during the synchronized period.

RESUMEN

Una perspectiva de redes complejas del acoplamiento pasado y futuro entre los océanos tropicales y las precipitaciones sobre el Sudeste de Sudamérica

Las anomalías de la temperatura de la superficie del mar (TSM) en los océanos tropicales generan patrones anómalos de circulación atmosférica en los extratropicos que pueden inducir cambios en las precipitaciones y fuentes de humedad de tales regiones. Varios estudios previos han mostrado que las anomalías de la TSM en latitudes tropicales del Pacífico, Atlántico e Índico impactan en la variabilidad de las precipitaciones sobre el Sudeste de Sudamérica (SESA). Además, estas tres cuencas tropicales pueden interaccionar entre sí induciendo anomalías en la TSM de las otras cuencas remotas a través de teleconexiones atmosféricas y oceánicas. Sin embargo, a día de hoy no está claro: (1) cómo esas anomalías en la TSM en los trópicos pueden interaccionar entre sí y, a su vez, colectivamente inducir variabilidad en las precipitaciones sobre SESA, (2) cómo esa interacción colectiva entre los océanos tropicales y la variabilidad de las precipitaciones sobre SESA podría cambiar en el próximo siglo como consecuencia de un calentamiento antropogénico, y (3) cómo las fuentes de humedad de SESA podrían variar considerando diferentes periodos en términos del grado de interacción colectiva entre los océanos tropicales y las precipitaciones sobre SESA.

En este trabajo, estas cuestiones son abordabas desde una perspectiva de redes complejas, construyendo una red climática en la que se consideran como nodos de la misma tres índices que caracterizan a los océanos tropicales (Niño3.4, Atlántico tropical Norte (TNA) y el dipolo del Índico (IOD)) y un cuarto que representa la variabilidad de las precipitaciones (PCP) sobre SESA. El comportamiento colectivo de estos nodos (representados por índices) es investigado a través de la detección de periodos de sincronización, los cuales son definidos a través de la distancia media de la red, una herramienta de la teoría de redes complejas que permite trabajar con varios procesos a la misma vez y detectar periodos de máxima interacción entre los nodos de la red.

Los resultados muestran que durante la primavera del siglo pasado, la distancia media de la red media (grado de sincronización entre los nodos de la red) presenta una gran variabilidad interannual e interdecadal, existiendo dos periodos de sincronización: uno que se desarrolla durante la década de los 30 y otro durante la de los 70. Del mismo modo,

se pudo ver que los océanos tropicales que interaccionan entre sí y, a su vez, influyen a la variabilidad de las precipitaciones en SESA cambian de un periodo de sincronización al siguiente. Mientras que durante la década de los 30 fueron el TNA y el Nino3.4, durante la década de los 70 fueron el IOD y el Nino3.4.

Un análisis de las proyecciones climáticas a futuro de siete modelos CMIP5 diferentes bajo los escenarios de cambio climático RCP4.5 y RCP8.5 sugiere que un forzamiento antropogénico incrementaría el número de periodos de sincronización por siglo, su longitud temporal y la conectividad de los nodos (con la excepción del TNA e IOD en RCP8.5). El aumento de la conectividad de las precipitaciones en SESA en ambos escenarios sugeriría un incremento de la influencia de los océanos sobre las precipitaciones como consecuencia de un forzamiento antropogénico, lo cual podría aumentar su predictibilidad estacional. Estas conclusiones basadas en el *grand CMIP5 ensemble mean* deben ser tomadas con cautela dada la alta dispersión existente entre los modelos.

Finalmente, en este trabajo también se analizó la variabilidad interdecadal de las fuentes de humedad de SESA durante el verano austral. Los resultados sugieren que las principales fuentes de humedad de SESA son el reciclaje de agua, la costa central-este de Brasil junto con el océano Atlántico circundante, y la región del océano Atlántico situada al suroeste del dominio de SESA. Una comparación entre las fuentes de humedad de un periodo no sincronizado (80's) con las de otro sincronizado (90's) muestra que las principales diferencias se encuentran en la intensidad del reciclado de agua en SESA y de la fuente de humedad de la costa central-este de Brasil. Además, se encontró que la región centrada en los (20ºS, 300ºE), cerca del núcleo del Jet de Capas Bajas, es una fuente de humedad sólo durante la década de los 90. Estas diferencias parecen estar asociadas al desarrollo de una circulación anticiclónica (ciclónica) anómala sobre la costa central-este de Brasil que favorece el transporte de humedad desde la parte central de Brasil (costa central – este de Brasil) hacia SESA en los '80 ('90).

AGRADECIMIENTOS

Quiero agradecer a mi director de tesis, el Dr. Marcelo Barreiro, toda la dedicación y orientación a lo largo de estos 4 años de doctorado. Siempre se mostró como una persona accesible y con la puerta abierta al diálogo ante cualquier tipo de duda o problema que se me presentara en el transcurso de mi investigación.

Del mismo modo, también me gustaría agradecerle a Emilio Hernández García la dirección durante mis estadías en el Instituto de Física Interdisciplinar y Sistemas complejos (IFISC) de la Universidad de las Islas Baleares (UIB).

A todos mis compañeros del instituto de física, y en particular a los del departamento de Ciencias de la Atmósfera (Santiago, Fernando, Stefanie, Matilde, Gianina, Made, Javier, Gastón, Romina, Juan y Natalia). Gracias a todos ellos (tanto físicos como atmosféricos) por toda la acogida que desde un principio me brindasteis y por todo el apoyo mostrado durante estos años de estudio. Gracias por los momentos de charla, por las "juntadas" para tomarnos unas cervezas y por las tardes/noches de asado que se prolongaban hasta horas intempestivas. Gracias. Sin duda alguna, habéis hecho de esta oportunidad una de las experiencias más bonitas que siempre recordaré con cariño.

A mis compañeros del proyecto LINC (Miguel Bermejo, Hisham Ihshaish , Marc Segond, Veronika Stolbova, Enrico Ser Giacomi, Dong Zhou, Liubov Tupikina, Giulio Tirabassi, Qingyi Feng, Fernando Arizmendi, Juan Ignacio Deza, Víctor Rodríguez, Alexis Tantet y Yang Wang), gracias por los momentos de discusión, por el apoyo y por el compañerismo.

A la familia Rosso – Rodríguez (Mario, Magali, Leticia, Daniela, Magali, Corina, Laura, Agustina, Matías, Valeria), quienes me abrieron las puertas de su casa como si fuera una más del clan desde el primer día. Sin duda alguna, fue ese lindo e inesperado regalo que

la vida me puso en el camino. Gracias por la acogida, por el hueco que me hicisteis entre vosotros, por el apoyo incondicional y el respaldo durante todo este tiempo.

A Susana. Gracias por el apoyo.

A Gabi. Gracias también por todo el apoyo y los momentos de ensayo en la recta final.

Gracias al *European Community's Seventh Framework* (FP7/2007-2011) y a la comisión académica de posgrado (CAP) de Uruguay, quienes financiaron el desarrollo de esta investigación.

Y finalmente, a los más importantes. Gracias a mis familiares y amigos de España. Gracias por estar siempre ahí, día tras día, mes tras mes, año tras año…. Gracias por ser ese punto de apoyo fijo, clave e incondicional que a pesar del paso del tiempo y de la distancia siempre está ahí.

Contents

i. List of acronyms

AGCM --- Atmospheric Global Circulation Model

AH --- Atlantic High

BH --- Bolivian High

CMIP5 --- Coupled Model Intercomparison Project Phase 5

DJF --- December – January – February

EOF1 --- First Empirical Orthogonal Function

ERSSTv2 --- Extended Reconstructed Sea Surface Temperatures version 2

ERSSTv3b --- Extended Reconstructed Sea Surface Temperatures version 3b

GPCCv5 --- Global Precipitation Climatology Center

HadSST --- Hadley Center Sea Surface Temperatures

IOD --- Indian Ocean Dipole

ITCZ --- Intertropical Convergence Zone

Nino3.4 --- Niño3.4 index: defined as the horizontal SST anomaly averaged over the region (5N, 5S) and (170W, 120W).

SA --- South America

SACZ --- South Atlantic Convergence Zone

SALLJ --- South American Low Level Jet

SAMS --- South American Monsoon System

SESA --- Southeastern South America

SON --- September – October – November

SST --- Sea Surface Temperatures

TNA --- Tropical North Atlantic

u --- zonal wind

uXXXmb --- zonal wind at XXX mb

v --- meridional wind

vXXXmb --- meridional wind at XXX mb

$\vec{v}_{\varphi}$--- purely divergent part of the wind

$\vec{v}_{\psi}$--- purely rotational part of the wind

V--- horizontal wind $\left(\vec{V} = u\vec{\imath} + v\vec{\jmath}\right)$

PCP --- Precipitation

PC1 --- First Principal Component

PH --- Pacific High

Z --- geopotential height

ψ--- streamfunction

φ--- velocity potential

1| Introduction

1.1. Motivation

Located to the south of the Amazon basin, Southeastern South America (SESA) is one of the most densely populated regions in South America (SA) covering Uruguay and small portions of northeastern Argentina and Southern Brazil. The economy of these regions is mainly based on the exploitation of natural resources, and their growth is particularly linked to intensification and expansion of the agriculture, ranching, dairy and afforestation (Bidegain et al., 2012). To get an idea of the importance of these sectors in the region, only livestock and agriculture represent more than 70% of the total Uruguayan exportations (Bidegain et al., 2012). However, the production and performance of these sectors are strongly vulnerable to climate -mainly to precipitation (PCP) variability- which impacts a wide range of sectors besides those mentioned above including commerce, power generation, water resources and many others (e.g., Robertson and Mechoso, 1998; Berbery and Barros, 2002, Hidalgo and Taddei, 2014; Podesta et al., 2002). Therefore, the development of an early warning system based on seasonal climate predictions may help to mitigate the negative impacts and take advantage in the opportunities. In order to build such a system, it is first necessary to understand the causes of the PCP variability and their associated physical mechanisms.

Overall, there exist two kinds of sources of PCP variability: one internal and another one external (see Figure 1.1). While the internal variability is related to the chaotic dynamics of the atmosphere and cannot be predicted beyond a couple of weeks (Lorenz, 1963), the external variability (or external forcing) is associated with the systematic atmospheric response to a boundary forcing that varies more slowlywith time (e.g., sea surface temperature (SST) anomalies and soil moisture). The latter type of variability source is the one that gives rise to the possibility of predicting PCP at much longer time scales than two weeks.

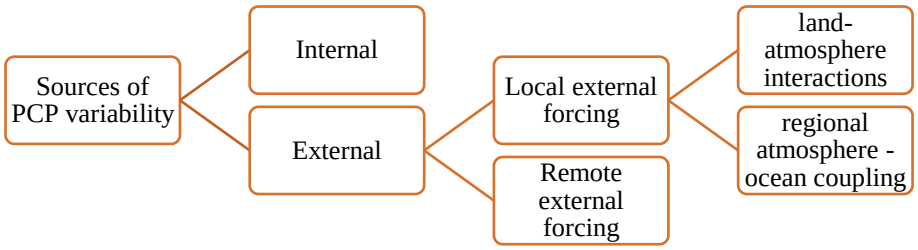

Figure 1.1. Flow diagram of the PCP variability sources.

The external forcing can be subdivided into two: local–external forcing and remote–external forcing (see Figure 1.1). The local-external forcing encompasses the regional atmosphere-ocean coupling and the land-atmosphere interactions, while the remote-external forcing refers to the influence that SST anomalies (mainly in the tropics) exert on subtropical/extratropical regions.

The aforementioned regional atmosphere-ocean coupling refers to the interaction between the oceans surrounding the region of study and the atmosphere located just aloft. Focusing on SESA, some studies have presented simultaneous correlations between PCP over SESA and the SST anomalies in the surrounding South Atlantic Ocean during late spring and early summer (e.g., Diaz et al., 1998). However, a causal relationship between them is not obvious because the anomalies in both places can be induced by the same

forcing, for example by the El Niño – Southern Oscillation (ENSO); an anomalous warming of the equatorial Pacific that arise from the coupling between the ocean and the atmosphere. To better understand the possible connection between SESA PCP and SST anomalies over the surrounding South Atlantic Ocean, Robertson et al., 2003 used Atmospheric Global Circulation Model (AGCM) simulations forced with prescribed patterns of south Atlantic SST anomalies and found a very weak response of PCP over SESA. Most recently, using ensembles of AGCM simulations and focusing on the role of the South Atlantic on SESA PCP, Barreiro 2010 showed for the first time that the south Atlantic can play a secondary role in affecting climate anomalies over SESA through the modulation of the persistence of the ENSO influence. He found that the ocean off Brazil and Uruguay responds to the ENSO signal by warming (cooling) during warm (cold) ENSO events through changes in the surface heat fluxes. This oceanic warming in turn alters the evolution of the atmospheric anomalies through a local thermodynamic feedback, resulting in increased persistence of the original atmospheric disturbance and thus affecting climate predictability over SESA.

The land-atmosphere interactions, on the other hand, are a kind of local–external forcing that refer to interactions between land-surface and the atmosphere located just aloft the region of study. Some examples of land–atmosphere interactions that can take place in the climate system are the coupling between: soil moisture and PCP (e.g., Koster et al., 2006), soil moisture and evapotranspiration (e.g., Guo et al., 2006), soil moisture and temperature (e.g., Senevirante et al., 2006) and/or the coupling between soil moisture and surface sensible and latent heat fluxes (e.g., Guo and Dirmeyer, 2013). The coupling between soil moisture and PCP tends to be the least robust because there are many processes that influence PCP at different spatial scales. Despite this, several studies have shown that the main regions of the Earth's surface for which soil moisture anomalies have

a substantial impact on PCP are found in transition regions between wet and dry climate conditions, where the evapotranspiration variations are high but still sensitive to soil moisture (e.g., Koster et al., 2004; Sörensson and Menéndez, 2011). Over these regions, the inclusion of land-atmosphere interactions in climate models is needed for a correct representation of the regional climate (e.g., Barreiro and Diaz, 2011). Focusing on SA, the main hotspot of soil moisture–PCP coupling appears over SESA, when soil moisture conditions are dry during the austral summer months (Ruscica et al., 2015).

The remote–external–source of PCP variability is represented by the influence that SST anomalies can exert on SESA PCP variability. According to the literature, SST anomalies over the tropical oceans play the most important role in predicting SESA PCP, being the state of the tropical Pacific the main predictor (e.g., Nobre et al., 2006; Barreiro 2010). SST anomalies over the extratropical regions, such as the South Atlantic Ocean, may also influence the predictability of climate over SESA (Diaz et al., 1998; Robertson et al., 2003; Barreiro 2010). However, as mentioned before, SST anomalies in the South Atlantic Ocean do not directly influence rainfall over SESA but play a secondary role in increasing/decreasing PCP predictability through the modulation of the ENSO influence over the region (Barreiro 2010). Therefore, the literature supports the view that only the tropical SST anomalies play an important role for the seasonal forecast of SESA PCP.

Finally, although both, soil moisture and tropical SST anomalies can increase PCP predictability over the region of study, the lack of observational soil moisture data over SESA results on a seasonal forecast that can only be based on tropical SST anomalies.

At this point, it is important to introduce and answer three important questions: (1) What is it known about the tropical SST anomalies influence on SESA PCP variability nowadays?, (2) what is not yet clear about this tropical oceanic influence on SESA PCP?, and (3) what are the main objectives of this work? Regarding the first question, there exist

several studies that show how SST anomalies over the tropical Pacific, Atlantic and Indian oceans can influence SESA PCP through different mechanisms that basically include the generation of quasi-stationary Rossby waves that propagate to higher latitudes (e.g., Vera et al., 2004) and anomalous changes in the Hadley and Walker regional cells (Ambrizzi et al., 2004). Moreover, there are other (studies) which analyze how the tropical oceans can interact between each other inducing SST anomalies in remote basin through atmospheric and oceanic teleconnections (Meyers et al., 2007; Annamalai et al., 2003; Wu and Kirtman, 2004; Yoo et al., 2013; Enfield and Mayer, 1997; Saravannan et al., 2000). However, most of these studies focus on the impact that one particular basin (or a combination of two) can have on SST anomalies over another remote basin, or on SESA PCP variability, not being clear nowadays how SST anomalies over the tropical oceans can interact between each other and, in turn, collectively influence SESA PCP variability (second question). Therefore, the main goal of this thesis is to analyze how the tropical oceans can interact between each other and, in turn, collectively influence SESA PCP variability.

1.2 Objectives

As it was mentioned, the main goal of this thesis is to analyze how the SST anomalies over the tropical oceans can interact between each other and, in turn, collectively influence SESA PCP variability. In particular, the specific objectives of this work are:

(1) To investigate how SST anomalies over the tropical oceans have interacted between each other over the last century, and in turn, collectively induce rainfall anomalies over SESA. In order to address this issue, we consider a complex network perspective and focus on the detection of synchronization periods, understanding synchronization as those periods of time in which the tropical oceans and the PCP over SESA were most connected.

(2) To determine how the collective interaction among the tropical oceans and SESA PCP observed during the last century could change during the next one as consequence of an anthropogenic forcing, and

(3) To assess the possible changes on the SESA moisture sources considering different periods in terms of the degree of collective interaction among the tropical oceans and SESA PCP. SST anomalies over the tropical oceans generate anomalies in the extratropical atmosphere circulation that can induce not only changes on PCP but also in the moisture sources because anomalies on the low level winds could introduce changes in the origin and intensity from where the water vapor is transported toward SESA.

1.3 Organization of the thesis.

This thesis is organized in seven chapters, and the methodology used is described in the corresponding chapter. In chapter 2 we present a review of South American climatology during the austral and summer seasons. In chapter 3, we present the main interannual variability modes that characterized the tropical oceans and that can induce rainfall variability over SESA. In turn, we introduce the two possible physical mechanisms through which the tropical oceans can influence SESA PCP. In chapter 4, we investigate the first specific objective, namely, the collective behavior among the three tropical oceans and SESA springtime precipitation during the 20th century. We focus on the detection of synchronization periods and hypothesize the possible physical mechanisms through which the tropical oceans interact among them, and in turn, influence SESA PCP variability. In chapter 5 we study how this collective behavior could change in the 21st century under a scenario of global warming (second specific objective). We consider seven climate models from the Coupled Model Intercomparison Project Phase 5 (CMIP5) and different climate change scenarios. In chapter 6, we address the last specific objective

by studying the variability of summertime SESA moisture sources, considering a period of synchronization and a period of no synchronization. Finally, in chapter 7 we present a summary and discuss several open issues that arose from the research carried out in this thesis.

2| The South American climatological patterns during spring- and summer-time

Owing to its large meridional extension, from 10ºN to 55ºS approximately, South America (SA) presents features from tropical, subtropical and extratropical climates. An example of these contrasting climates is given by the Amazon forest and the Atacama desert. While the Amazon forest represents one of the world's most humid climates, occupying about 35% of the continent and 65% of its tropical area (Satyamurty et al., 1998), the Atacama desert in northern Chile represents a region with very dry and arid climate conditions.

The regional circulation patterns that characterize SA at low levels during the austral spring and summer seasons are strongly influenced by its prominent topography, being the Andes, the Brazilian highlands and the Guiana shield the most important orographic structures (e.g., Gandu and Geisler 1991; Kodoma et al., 2012; Junquas et al., 2015). In upper levels, however, the orographic influence is smaller and the regional circulation depends seasonally on the varying horizontal temperature gradients, which arise from differential heating due to the difference in thermal capacity between land and water (Viviane et al., 2012).

In this work, we focus on the austral spring, which corresponds to September – October – November (SON) months, and the austral summer, which corresponds to December – January – February (DJF) months. The reasons why we focus our work on these two

austral seasons are because it is during these periods when the sowing and harvesting of many of the agricultural products takes place, and in addition, when the influence of the tropical oceans on Southeastern South America (SESA) precipitation (PCP) is stronger (during the austral winter), and when the peak of El Niño phenomenon occurs (during the austral summer).

In this chapter the climatological features that characterized SA during spring and summer are shown in terms of patterns of PCP and atmospheric circulation. Before showing the climatological features, we first introduce the data and methodology employed to describe them.

2.1 Data and Methodology.

The main features of the SA climatology are presented considering the monthly mean of the horizontal wind (u) at 850mb, the horizontal divergence of the wind ($\nabla \cdot \vec{V}$) at 200mb, the streamfunction (ψ) at 200mb and the PCP field. The monthly means of the horizontal wind components at 850mb and the horizontal divergence at 200mb are obtained from the ERA – Interim reanalysis data (Dee et al., 2011) and cover the period (1979 – 2006), while the monthly mean values of PCP data are obtained from the Global Precipitation Climatology Center version 5 (GPCCv5) and cover the period (1901 – 2006).

The streamfunction is computed by solving the 2D Poisson equation:

$$\Delta\psi = \vec{\nabla} \cdot \vec{V} \quad (2.1)$$

Where $\vec{V} = (u, v)$.

The seasonal means of the horizontal wind circulation at 850mb, horizontal divergence of the wind at 200mb, streamfunction and PCP fields are computed by averaging the

September – October – November months for the case of the spring, and December – January – February for the case of the austral summer.

Finally, in order to present the PCP variability of SA at interannual time scales, we compute the first Empirical Orthogonal Function (EOF1) and it associated Principal Component (PC1) of the PCP during each season. More information about the principal component analysis can be found on von Storch and Zwiers, (2002).

2.2 Atmospheric circulation patterns that characterize the South American climatology during springtime (September – November).

Figure 2.1 (a) shows the springtime low-level atmospheric circulation pattern together with the horizontal wind divergence ($\nabla \cdot \vec{V}$) at 200mb over the period (1979 – 2006). At lower levels, the regional atmospheric circulation presents two high pressure systems, one found over the western subtropical South Pacific (PH on Figure 2.1(a)) and the other one over the Subtropical South Atlantic (AH on Figure 2.1(a)). North of AH and over the southern hemisphere tropics, the easterlies penetrate into the continent flowing as far west as Colombian's and Peruvian's Andes, where they are deflected southward turning into northerly or northwesterly (Figure 2.1 (a)). This northerly/northwesterly low level flow located east of the Andes transports moisture toward the extra-tropics, particularly to La Plata basin. A regional intensification of this circulation is commonly known as the South American Low level Jet (SALLJ; Vera et al., 2006).

Over the equatorial Pacific and Atlantic oceans, the trade winds convergence induces mid-tropospheric rising motions, and by continuity, divergence at upper-levels (see Figure 2.1 (a)). This upper-level divergence is observed in Figure 2.1 (a) as two narrow bands of brownish colors over the equatorial Pacific and Atlantic Oceans which mark the presence of the Intertropical Convergence Zones (ITCZs). There are also positive values

of the horizontal wind divergence over SA north of 20ºS (Figure 2.1 (a)), associated with continental precipitation maximum values (Figure 2.1 (c)). Overall, as shown in Figure 2.1 (b), the upper-level tropospheric circulation is characterized by a westerly flow over the whole SA continent.

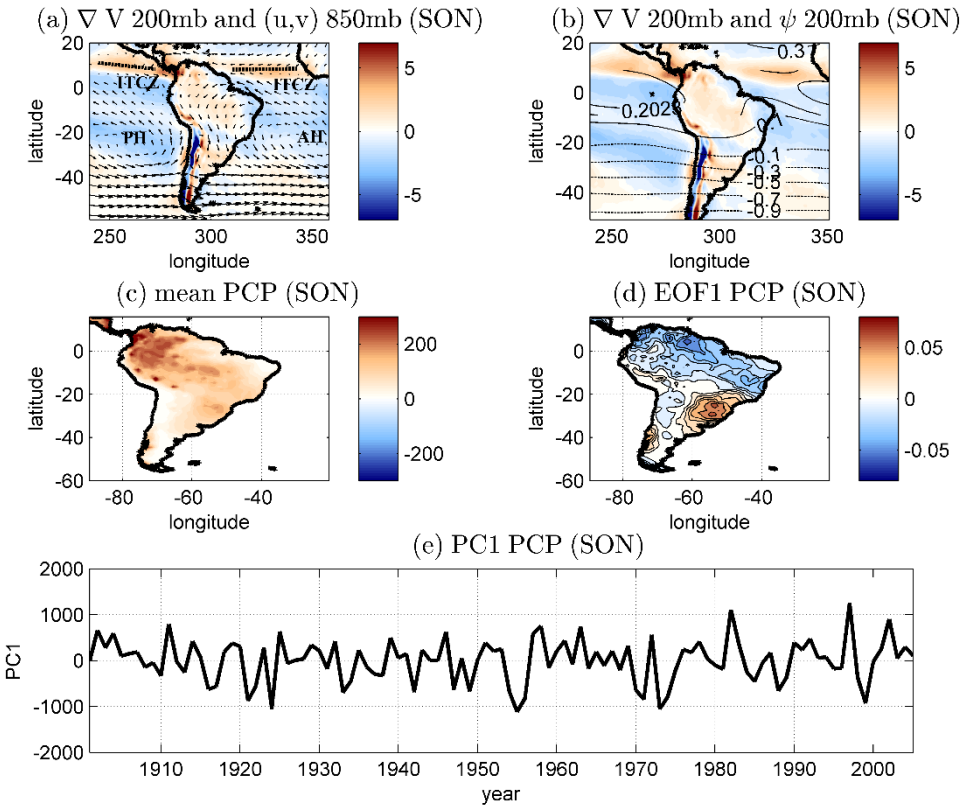

Figure 2.1. Mean values of (a) horizontal wind divergence at 200mb in 10^{-6} s^{-1} (shaded regions) and horizontal wind pattern at 850mb in $m \cdot s^{-1}$ (vectors); (b) horizontal wind divergence at 200mb in 10^{-6} s^{-1} (shaded regions) and streamfunction at 200mb (contours), (c) mean PCP over SA, (d) the EOF1 component of PCP over SON and (e) its associated PC1.

Interannual variability is characterized by calculating the Empirical Orthogonal Functions (EOFs) of seasonal mean rainfall. The first principal component (EOF1) associated to the PCP field presents a dipole mode with centers of opposite rainfall anomalies over central-

east Brazil and SESA (Figure 2.1 (d)). The negative (positive) phase of this dipole is characterized by an enhanced (suppressed) convection over the central-east Brazil and suppressed (enhanced) convection over SESA. This suggests that while positive (negative) precipitation anomalies develops over the central-east Brazil, negative (positive) anomalies take place over SESA. Changes in the strength and direction of the SALLJ control the moisture transport from the Amazon basin into SESA (Nogués-Paegle and Mo, 1997). Strong (weak) SALLJ events are associated with a westward (eastward) shift of the AH which lead to increased (decrease) southward moisture transport and convective activity in SESA (Nogués-Paegle and Mo, 1997).

2.3 Atmospheric circulation patterns that characterize the South American climatology during summertime (December – February).

The atmospheric circulation over SA during summertime is strongly linked to the South American Monsoon System (SAMS), whose main features are shown on Figure 2.2. During this season, as the solar declination decreases, temperatures over the continent become warmer that neighboring oceanic regions due to the difference in thermal capacity between land and water. This induces a direct thermal circulation with low-level (upper-level) convergence (divergence), mid-tropospheric rising motions and precipitation over the continent, and low-level (upper-level) divergence (convergence), mid-tropospheric sinking motions and dry conditions over the neighboring oceanic areas (Figures 2.2 (a) and (c))

The upper-tropospheric circulation is characterized by a quasi-stationary anticyclone-trough system with two actions centers: the Bolivian High (BH on Figure 2.2 (b)), located over the Altiplano, and the Nordeste Low, located over the tropical/subtropical South Atlantic near the coast of northeast Brazil.

Several studies have shown that the origin of the BH is a Rossby wave response to the condensational heating over the Amazon Basin. Its position, southwest of the region of maximum diabatic heating, is consequence of a southwestward propagation and subsequent decay of this Rossby wave during repeated episodes of convection (Lenters and Cook, 1997; Figueroa et al., 1995; Silva Dias et al., 1983). This result is in agreement with the theory of the atmospheric response to tropical diabatic heating forcing given by Webster (1972) and Gill (1980).

Lenters and Cook (1997) also showed that BH's strength is most strongly influenced by the PCP over the central Andes and that the role of the topography (and in particular of the Andes mountains) on both, the origin and strength of the BH, seems to be secondary.

Regarding the climatological low-level atmospheric circulation, Figure 2.2(a) shows the main features that characterize the SA circulation pattern during summer. The low-level features include: (1) two surface high pressure systems, one located over the subtropical southwestern South Pacific (SP on Figure 2.2(a)) and the other one over the subtropical South Atlantic (AH on Figure 2.2(a)), (2) the Chaco thermal low over northern Argentina, (3) the South Atlantic convergence zone (SACZ on Figure 2.2(a)), and (4) the South American Low Level Jet (SALLJ).

As in spring, north to the AH and over southern hemisphere tropics, the easterlies penetrate into the continent flowing as far west as Colombian's and Peruvian's Andes, where they are deflected towards the south turning into northerly or northwesterly east of the Andes (Figure 2.2 (a)). Regional intensification of this northerly/northwesterly low level flow east of the Andes is the SALLJ, which is mechanically forced by the Andes mountains all-year round, transports moisture from the tropics to extratropical latitudes, presents larger activity during the austral summer and is considered to close off the South

Atlantic subtropical anticyclone located east of the continent (Rodwell and Hoskins 2001; Berbery and Barros, 2002; Campetella and Vera, 2002).

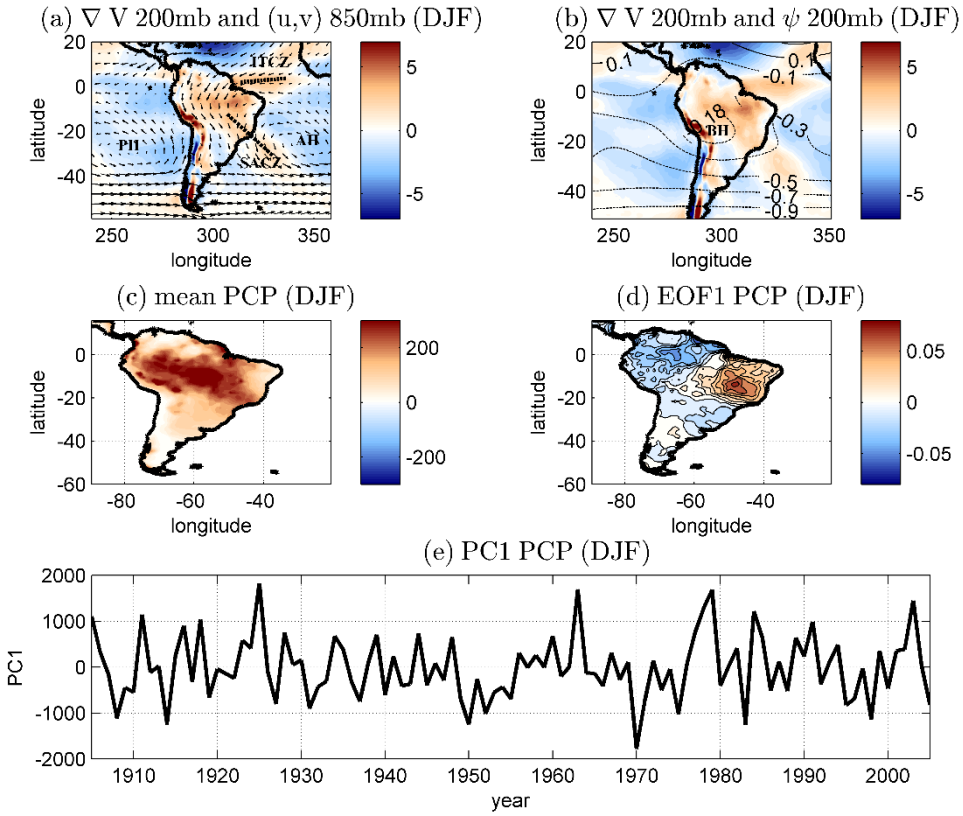

Figure 2.2. Mean values of (a) horizontal wind divergence at 200mb in 10^{-6} s^{-1} (shaded regions) and horizontal wind pattern at 850mb in $m \cdot s^{-1}$ (vectors); (b) horizontal wind divergence at 200mb in 10^{-6} s^{-1} (shaded regions) and streamfunction at 200mb (contours), (c) mean PCP over SA, (d) the EOF1 component of PCP over DJF and (e) its associated PC1.

The southwestward band of positive divergence that extends from the southern Amazon towards Southeastern Brazil and surrounding Atlantic Ocean marks the position of the SACZ (Figure 2.2 (a)). It consists of a band of cloudiness and strong PCP, whose location and intensity are influenced by the Andes and the Brazilian highlands in such a way that, a suppression of either would induce a weakening and northward shift of SACZ (e.g.,

Kodoma et al., 2012; Junquas et al., 2015; Grimm et al., 2007). For its maintenance, it needs transient moisture flux from the Amazon through the SALLJ and represents the hallmark of the mature monsoon across SA (Marengo et al., 2012).

The equatorial convergence of the trade winds at low-levels and divergence in upper-levels mark the ITCZs positions. Positive values of the upper-level divergence are also found over most Brazil (Figure 2.2 (a)) with maximum mean values associated with the PCP over the Amazon forest (see Figure 2.2 (c)). In turn, if we compare Figures 2.1 (c) and 2.2 (c), the maximum PCP amount is displaced to the southeastern in summer with respect to spring. This is associated with the solar declination decrease from spring to summer and the deep convection activation over the Amazon.

The EOF1 of summer rainfall over SA presents a dipole-like structure with two centers of action, one located over the continental part of the SACZ and central-east Brazil, and the other one over SESA (Figure 2.2 (d)). Once again, the negative (positive) phase of the dipole is characterized by an enhanced (suppressed) SACZ and suppressed (enhanced) convection over SESA. This suggests that when positive (negative) PCP anomalies develop over SACZ, negative (positive) anomalies take place over SESA. As it was previously mentioned, changes in the strength and direction of the SALLJ control the moisture transport from the Amazon basin into SESA (Nogués-Paegle and Mo, 1997), in such a way that, strong (weak) SALLJ events are associated to a westward (eastward) shift of the South Atlantic subtropical high, leading to an increase (decrease) of moisture transport and convective activity in SESA and to a weakened (enhanced) SACZ (Nogués-Paegle and Mo, 1997). This pattern is similar to the one observed in spring but with an additional strong center in northwestern SA (compare Figures 1.2 (d) and 1.3(d)), in agreement Grimm et al., 2007; Grimm 2010).

The patterns shown on Figures 2.1 (a), (b) and 2.2 (a), (b) represent the climatological features that characterize the SA circulation on spring- and summer-time. However, climate over SA has been shown to depend on the conditions of the tropical oceans. For example, several authors have shown that sea surface temperature (SST) anomalies in the tropics can affect the position and intensity of the AH and PH as well as the intensity of the SALLJ and the SACZ through atmospheric teleconnections. In the next section we present the main variability modes that characterize the tropical oceans and that can influence the features of the SA climate, and in particular SESA PCP. We also show their associated tropical – extratropical atmospheric teleconnection patterns.

3| Interannual variability modes in the tropical oceans and the tropical – extratropical atmospheric teleconnection

Several previous studies have already shown that sea surface temperature (SST) anomalies over some specific regions in the tropics can influence precipitation (PCP) variability over South America (SA), and in particular, over Southeastern South America (SESA). Grimm et al., 2010, Grim et al., 2000; Yulaeva and Wallace, 1994; Chan et al., 2008; Mo and Berbery, 2011 and Yoon and Zeng, 2010 are some of the works which have previously shown that SST anomalies over the Indian Ocean Dipole (IOD), the Tropical North Atlantic (TNA), the equatorial Atlantic (ATL3) and the Niño3.4 (see their spatial domains on Table 3.1) can influence SESA PCP. In this section, we describe these interannual variability modes of tropical oceans (IOD, TNA, ATL3 and Niño3.4) and show the associated tropical – extratropical atmospheric teleconnections patterns in the Southern Hemisphere. We also introduce the physical mechanism through which these teleconnections patterns arise and affect SESA PCP variability.

3.1. Data and Methodology

We consider the monthly mean of SST from ERA Interim reanalysis data (Dee et al., 2011) in order to describe the main modes of tropical variability. The description is made by computing the regression maps of the each mode's index (Niño3.4, or TNA, or IOD, or ATL3) onto the SST anomalies over the period (1979-2006). Each one of the oceanic indices (Niño3.4, TNA, IOD and ATL3) are computed as follows: we first average

latitudinal and longitudinally the monthly mean values of SST in the domains specified in Table 3.1. We then eliminate the trends of each one and compute their monthly anomalies removing the climatological cycle from 1979 to 2006. In the case of the IOD, we subtract the average between the two boxes to construct the index.

In turn, we also consider the monthly mean of geopotential height at 200mb, horizontal wind components at 200mb and meridional wind at 850mb from ERA Interim reanalysis data (Dee et al., 2011) during the period (1979 – 2006). From the horizontal wind components at 200mb, we calculate the velocity potential in order to analyze the divergent circulation in upper levels. Then, the tropical – extratropical atmospheric teleconnections patterns in the Southern Hemisphere are described by computing the regression maps of each index onto the geopotential height at 200mb (Z200mb), velocity potential at 200mb ($\varphi 200\mathrm{mb}$) and meridional wind at 850mb ($v850\mathrm{mb}$).

Index short name	Long name index	Earth's region	
		Latitude range	Longitude range
NINO3.4	Niño3.4	5ºN-5ºS	170ºW-120ºW
TNA	Tropical North Atlantic	10ºN-30ºN	60ºW-30ºW
IOD	Indian Ocean Dipole	10ºS-10ºN 10ºS-0ºN	50ºE-70ºE 90ºE-110ºE
ATL3	Equatorial Atlantic	3ºN-3ºS	0ºW-20ºW

Table 3.1. Geographical regions that represent the oceanic indices. Each index is computed through the spectral average of the SST in the specified regions.

3.2 Interannual variability modes in the tropical oceans.

3.2.1 El Niño – Southern Oscillation.

The El Niño – Southern Oscillation (ENSO) phenomenon is the largest variability mode at interannual timescales that strongly affects climate in tropical and extratropical areas.

According to the National Oceanic and Atmospheric Administration (NOAA), the positive (negative) phase of ENSO phenomenon, usually called El Niño (La Niña), consists in an anomalous spatially-averaged warming (cooling) in the equatorial Pacific larger than or equal to 0.5ºC over three consecutive months (see Figure 3.1 (b)). The maximum warming usually takes place on late December and its frequency varies from 3 to 7 years.

There exist several indices to monitor the tropical Pacific (Niño 1+2, Niño 3, Niño 4 and Niño 3.4), all of which are based on SST anomalies averaged across a given region (see Table 3.2). Figure 3.1(a) represents the Nino3.4 index time series during the period 1979 – 2006, that is computed as the horizontal average of SST anomalies over the region specified on Tables 3.1. The Niño3.4 index is the most commonly used index to define El Niño and La Niña events and it is the index considered throughout this work.

During El Niño events, the anomalous warming over the equatorial Pacific (see Figure 3.1 (b)) induces anomalous low – level convergence, mid tropospheric rising and upper – level divergence over the central equatorial Pacific (see Figure 3.1 (d)). Once the air diverges in upper - levels, part moves to the east and other part to the west. The anomalous upper – level westerly flow converges over the northeast Brazil (see Figure 3.1 (d)), inducing subsidence and low – level divergence. On the other hand, the anomalous upper – level easterly flow converges over the Indonesian area (see Figure 3.1 (d)), inducing air subsidence and lower –levels divergence. This upper – level configuration induces a shift to the east of the maximum convection area situated over the western Pacific Ocean warm pool in normal conditions, bringing rainy periods over the central equatorial Pacific (where there is an anomalous upper – level divergence on Figure 3.1 (d)) and dry periods over the Indonesia and Northeast Brazil (where on Figure 3.1 (d) an upper – level convergence develops).

Index	Longitude domain	Latitude domain	Description
Niño1+2	90W – 80W	0 – 10S	It corresponds with the region of coastal South America where El Niño was first recognized by the local populations.
Niño3	150W – 90W	5N – 5S	This region was once the primary focus for monitoring and predicting El Niño, but researchers later learned that the key region for coupled ocean-atmosphere interactions for ENSO lies further west
Niño4	160E – 150W	5N – 5S	The Niño 4 index captures SST anomalies in the central equatorial Pacific. This region tends to have less variance than the other Niño regions.
Niño3.4	170W – 120W	5N – 5S	The Niño 3.4 anomalies may be thought of as representing the average equatorial SSTs across the Pacific from about the dateline to the South American coast.

Table 3.2. Geographical areas used to define different El Niño indices. Information copied from (Trenberth et al., 2016): https://climatedataguide.ucar.edu/climate-data/nino-sst-indices-nino-12-3-34-4-oni-and-tni

Focusing on figure 3.1 (c), it is possible to see Z200mb anomalies resembling Rossby wave trains propagating from the tropics to extratropical latitudes. These anomalies generate advection of cyclonic vorticity toward SESA which constitutes a dynamical forcing that favors ascent motions and a PCP increase. The physical mechanism for understanding this atmospheric response to an anomalous warming over the tropical ocean is explained in section 3.3.

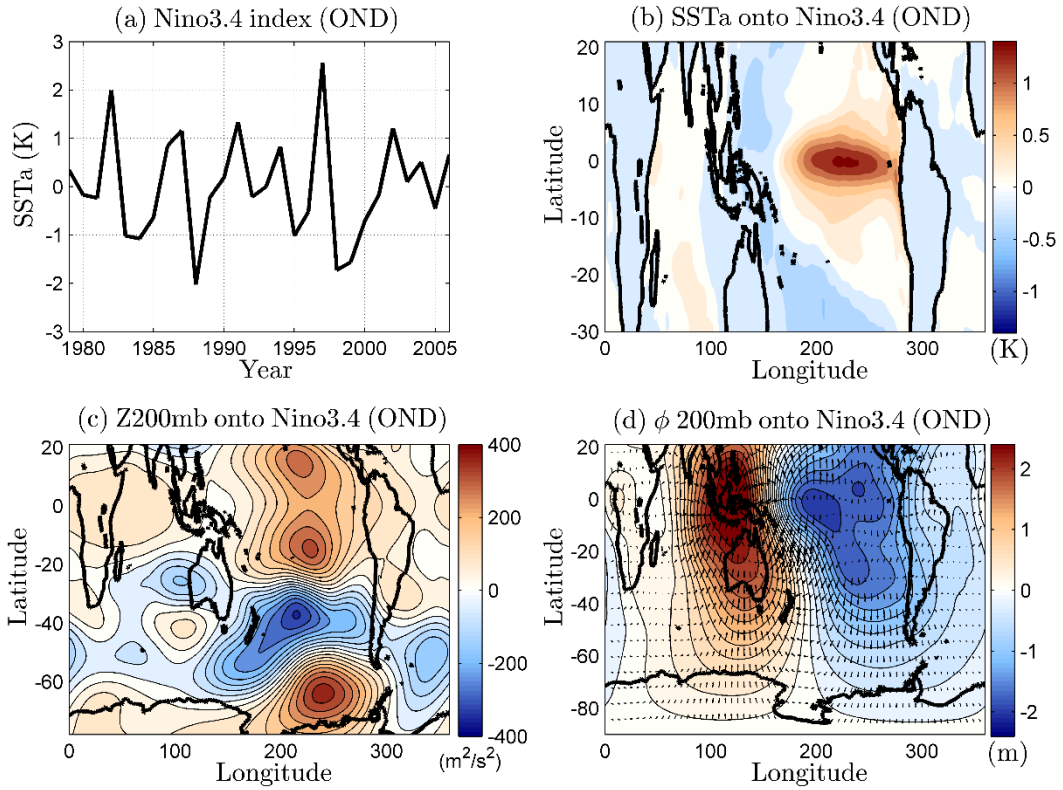

Figure 3.1 (a) Niño3.4 index as the OND (October – December) SST anomalies, (b) regression map of SST anomalies onto Nino3.4 index (both centered on OND), (c) regression map of the anomaly geopotential high at 200mb onto Nino3.4 index (both centered on OND), and (d) regression map of the anomaly velocity potential (shaded regions) and anomaly divergent velocity (vectors) onto Niño3.4 index (all of them centered on OND). Periods: 1979 – 2006.

3.2.2 The Indian Ocean Dipole.

The Indian Ocean Dipole (IOD) is a coupled ocean-atmosphere phenomenon in the Indian Ocean that peaks on austral spring. Its positive phase is characterized by anomalous warming of SST in the western equatorial Indian Ocean and anomalous cooling of SST in the south eastern equatorial Indian Ocean (see Figure 3.2 (b)). While the positive SST anomalies over the western tropical Indian Ocean (see Figure 3.2 (b)) have associated

mid-tropospheric rising motions and upper – level divergence aloft (see Figure 3.2 (d)), the negative SST anomalies over the eastern equatorial part of the Indian Ocean inhibit the vertical ascent motions turning into an anomalous upper-level convergence, air subsidence, and lower–level divergence. Associated with these anomalous changes, the normal convection situated over the eastern Indian Ocean warm pool is shifted to the west, bringing heavy rainfall over east Africa and severe droughts/forest fires over the Indonesian region.

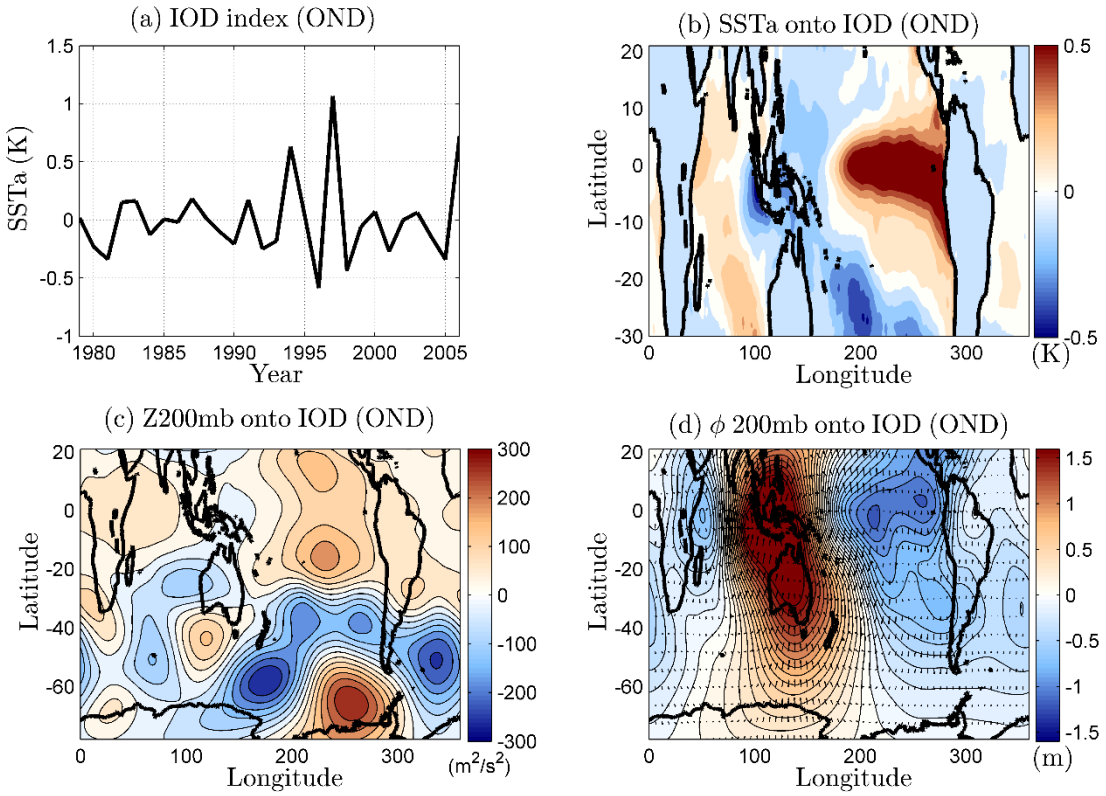

Figure 3.2. (a) IOD index as the OND (October – December) SST anomalies, (b) regression map of SST anomalies onto IOD index (both centered on OND), (c) regression map of the anomaly geopotential high at 200mb onto IOD index (both centered on OND), and (d) regression map of the anomaly velocity potential (shaded regions) and anomaly divergent velocity (vectors) onto IOD index (all of them centered on OND). Periods: 1979 – 2006.

The IOD influence on extratropical regions takes place through the generation of Rossby waves that propagate from tropical latitudes toward higher latitudes in an arc-like trajectory. Figure 3.2 (c) reflects upper–level cyclonic vorticity advection toward SESA through an anomalous Rossby wave train that propagates from the tropics to SESA. The IOD is influenced by ENSO as several authors have shown (Annamalai et al., 2003; Meyers et al., 2007; Wang and Wang, 2014), and can be seen in Figure 3.2(a) as the coexistence of SST anomalies in the tropical Indian and Pacific basins. Thus, anomalies in Figure 3.2 (c) may be result of SST anomalies in both ocean basins.

3.2.3. The Tropical North Atlantic.

Here Tropical North Atlantic (TNA) is defined as the area within the coordinates (10N-30N, 60W-30W) that extends over the Atlantic Ocean (see Figure 3.3 (b)). Its variability is strongly influenced by the strength of the northern trades, such that a weakening of the trade winds induces warming due to a decrease in surface heat fluxes. This region also represents the tropical part of the Atlantic Multidecadal Oscillation. Although there are few studies analyzing the influence of this oceanic region on the Southern Hemisphere climate, and in particular, over SESA, some authors have found a possible connection with rainfall over the Amazon Basin through anomalies in the divergent circulation (e.g., Yoon and Zeng, 2010).

Figure 3.3 (d) shows the regression map of the potential velocity and divergent velocity onto TNA index, suggesting that an anomalous warming over the tropical north Atlantic would induce and anomalous upper–level wind divergence aloft and upper–level convergence over the northeast of Brazil. In turn, Figure 3.3 (c) suggests that an anomalous warming of the TNA would increase the low – level transport of moisture toward SESA.

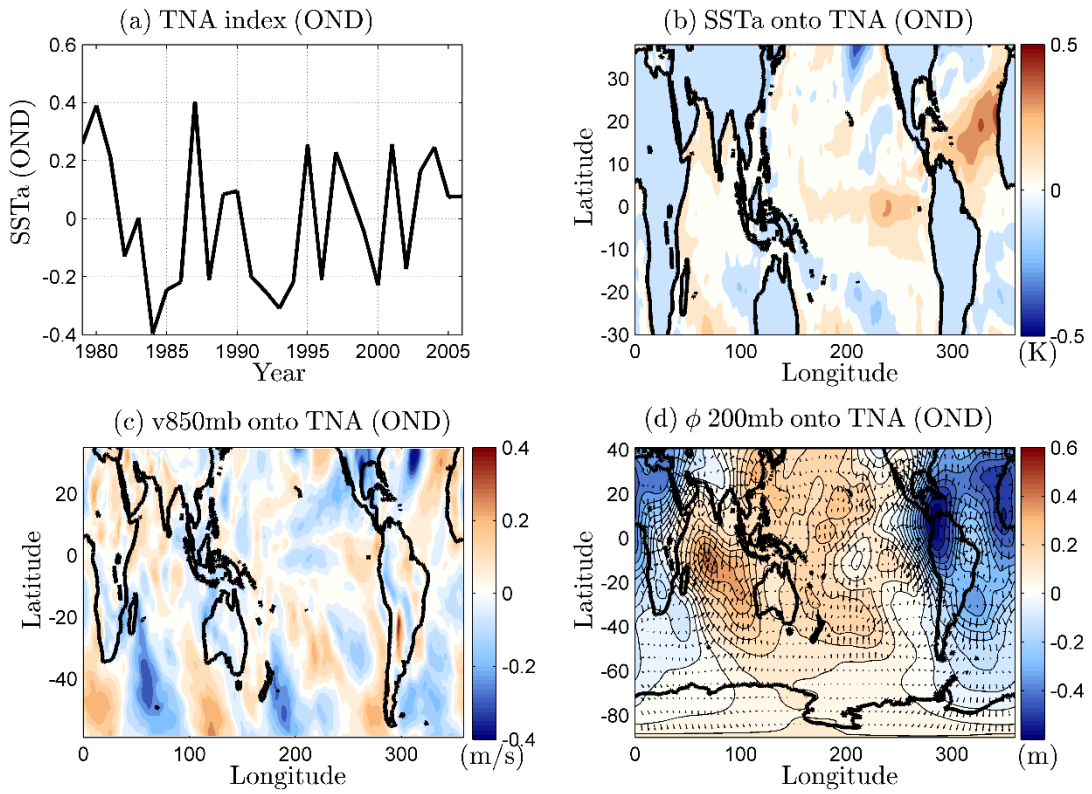

Figure 3.3. (a) TNA index as the OND (October – December) SST anomalies, (b) regression map of SST anomalies onto TNA centered on OND, (c) regression map of the anomaly meridional wind at 850mb onto TNA index (both centered on OND), and (d) regression map of the anomaly velocity potential (shaded regions) and anomaly divergent velocity (vectors) onto TNA index (all of them centered on OND). Periods: 1979 – 2006.

3.2.4 The Atlantic Niño.

The Atlantic Niño (ATL3) is a phenomenon analogous to the Pacific El Niño. It represents the main variability mode of SST over the equatorial Atlantic at interannual timescales (see Figure 3.4 (b)), and is characterized by irregular episodes of warming, which peak during boreal summer with a secondary peak during winter (Zebiak, 1993). The ATL3 index is plotted on Figure 3.4(a)).

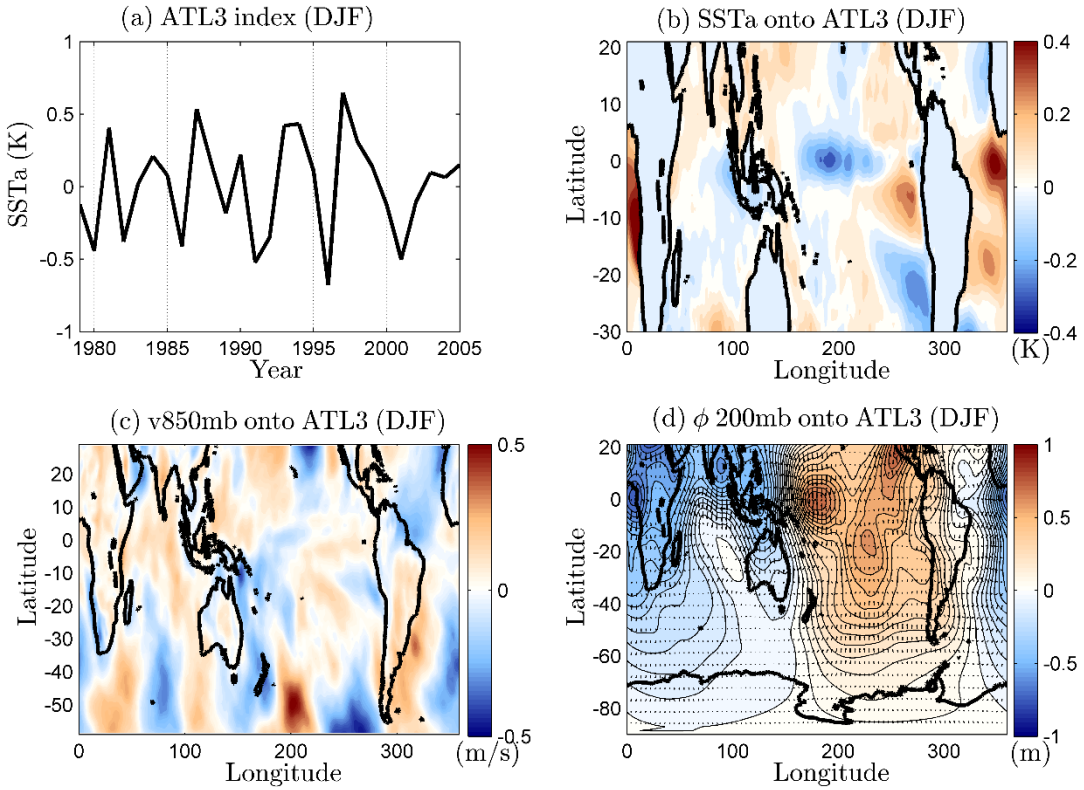

Figure 3.4. (a) ATL3 index as the DJF (December – February) SST anomalies, (b) regression map of SST anomalies onto ATL3 index centered on DJF, (c) regression map of the anomaly meridional wind at 850mb onto ATL3 index (both centered on OND), and (d) regression map of the anomaly velocity potential (shaded regions) and anomaly divergent velocity (vectors) onto ATL3 index (all of them centered on OND). Periods: 1979 – 2006.

To our knowledge, there are no studies which analyze the direct influence of the equatorial Atlantic SST anomalies onto SESA precipitation variability. Barreiro and Tippmann (2008) studied the effect of Atlantic SST anomalies on rainfall over SESA during January – February, with special focus on El Niño years. They found that the state of the equatorial Atlantic can modulate the influence of the El Niño years on rainfall over SESA, in such a way that when the equatorial Atlantic is warm, the El Niño influence is weaker. This influence seems to occur through the response of the low–level wind to SST

anomalies over the ATL3 region. The convergence of the westerly anomalies onto the warm anomaly over the equatorial Atlantic decreases the equatorial trades and the moisture flow into the Amazon and reduces the northerly flow that brings moisture to SESA. This physical mechanism agrees with Figure 3.4 (c), which shows a decrease in of the northerly flow almost over the whole SA when the ATL3 region is warm.

Finally, from Figure 3.4 (d), it is possible to see that the warm equatorial Atlantic seems to occur when the equatorial Pacific is cold. Therefore, Figures 3.4 (b), (c) and (d) also have influence from the equatorial Pacific, being difficult to separate, using this methodology, the signal coming from the Atlantic and that one from the equatorial Pacific.

3.3 Physical mechanisms for tropical – extratropical teleconnections.

There are two different mechanisms through which the tropical oceans influence the extratropical SA climate. They include anomalous changes in the Hadley and Walker regional cells (e.g., Ambrizzi et al., 2004) and/or the generation of quasi-stationary Rossby waves that propagate to higher latitudes (e.g., Vera et al., 2004). In this section, we introduce an explanation of the anomalous changes in the Hadley and Walker regional cells and then we focus on the linear theory that explains the Rossby waves generation.

3.3.1 Anomalous changes in the Hadley and Walker regional cells.

The Walker cell is an atmospheric circulation confined to the equatorial plane which is driven by the equatorial zonal SST gradient along the Pacific Ocean (Lau and Yang, 2003). Its characteristics are largely determined by the coupling between the tropical atmosphere and the oceans. Figure 3.5 shows a schematic diagram of the Walker circulation during DJF under ENSO – neutral conditions. The trade winds which flow from east to west at the equator, push sea waters towards the west side of most ocean

basins and induce relative warmer surface water in the west and cooler in the east. The relative warmer surface waters over the western Pacific is commonly known within the scientific community as the Pacific warm pool. Above this large Pacific warm pool, air converges and rises (see Figure 3.5). Above the cooler surface water in the east Pacific there is subsidence of dry air (see Figure 3.5). This configuration favors more (less) convection and precipitation over the large warm pool and equatorial – South America (central equatorial Pacific).

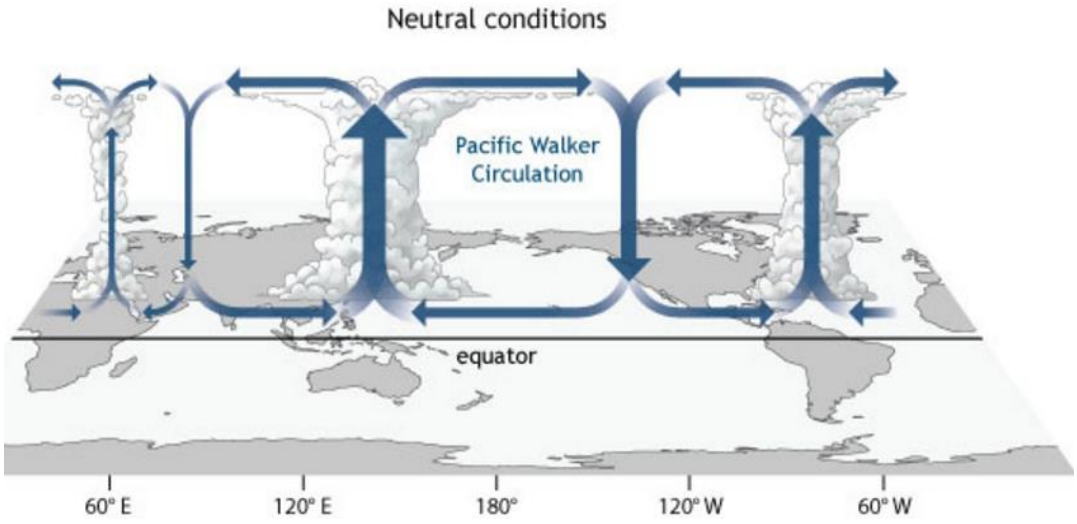

Figure 3.5. Pacific Walker circulation during DJF ENSO – neutral conditions. Figure taken from NOAA Climate: https://www.climate.gov/news-features/blogs/enso/walker-circulation-ensos-atmospheric-buddy

Interannual variations in the Walker circulation are associated with ENSO. Figure 3.6 shows a schematic diagram of the anomalous Walker circulation which develops during an El Niño event. The positive SST anomalies over the central and east equatorial Pacific induce low level wind convergence and upward movement aloft, helping to shift the upward branch of the Walker circulation to the east with respect to neutral conditions. By continuity, the mid-tropospheric rising over the central east equatorial Pacific induces an upper-level divergence aloft and strong precipitation. The upper-level divergence

generates two flows, one to the east and another to the west. The flow moving to the east converges over the equatorial SA, where it sinks. The flow which moves to the west converges over Indonesia and sinks. As result there are negative precipitation anomalies during El Niño over Indonesia and equatorial South America.

Anomalies in the Walker circulation can also alter the Hadley circulation. In particular, under El Niño, the anomalous sinking branch of the Walker circulation over equatorial South America inhibits the regional rising branch of the meridional circulation associated with the regional Hadley cell which, in turn, could affect subsidence over the subtropics.

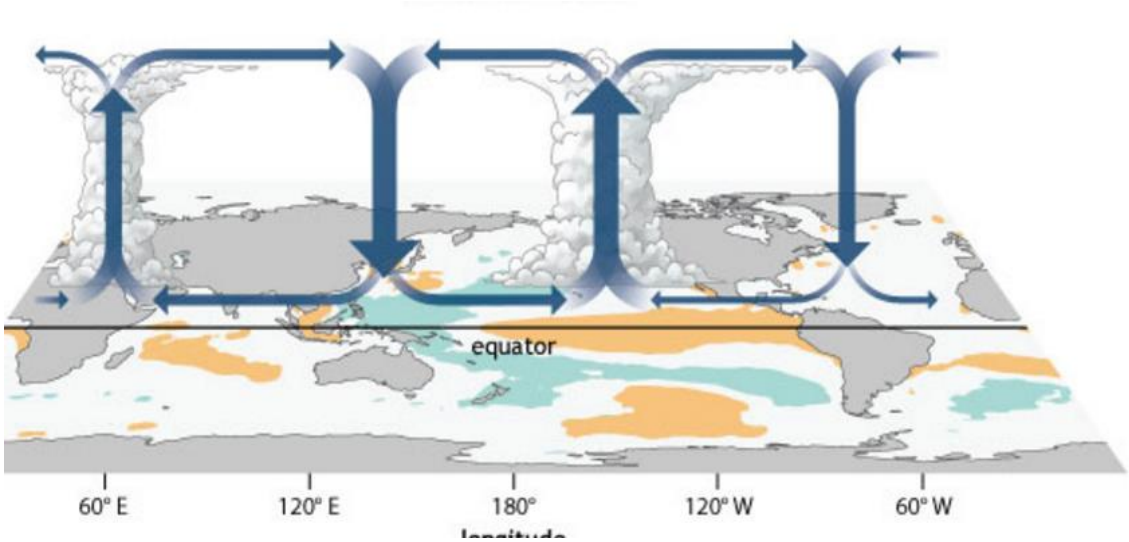

Figure 3.6. Pacific Walker circulation during DJF ENSO conditions. Figure taken from NOAA Climate.gov: https://www.climate.gov/news-features/blogs/enso/walker-circulation-ensos-atmospheric-buddy. For the case of the negative phase of ENSO, the anomalous Walker circulation would be the opposite.

3.3.2 Linear theory of Rossby wave dispersion.

Tropical – extratropical atmospheric teleconnections are mainly understood in terms of the linear theory of Rossby wave dispersion. The generation of Rossby waves is physically associated to the anomalous tropical mid-troposphere diabatic heating

consequence of the anomalous latent heat released during the water vapor condensation. The anomalous divergent flow in upper levels related to the anomaly in deep convection induces an anomalous meridional displacement of the air parcels that, by conservation of the absolute vorticity, generates a Rossby wave.

Following James I, (1995, Chapter 8) let's consider the vorticity equation for a single level in the atmosphere (for example, 200mb):

$$\frac{d(f+\xi)}{dt} = \underbrace{-(f+\xi)\cdot\left(\frac{\partial u}{\partial x}+\frac{\partial v}{\partial y}\right)}_{\substack{vortex\\ stretching}} \underbrace{-\left(\frac{\partial w}{\partial x}\frac{\partial v}{\partial z}-\frac{\partial w}{\partial y}\frac{\partial u}{\partial z}\right)}_{tilting} + \underbrace{\frac{1}{\rho^2}\left(\frac{\partial \rho}{\partial x}\frac{\partial P}{\partial y}-\frac{\partial \rho}{\partial y}\frac{\partial P}{\partial x}\right)}_{solenoidal} \quad (3.1)$$

whereξ, f, u, v, w and Prepresents the relative and planetary vorticity, the zonal, meridional and vertical wind component and the pressure, respectively. The first term of the right hand side of eq. (3.1) is known as the stretching, the second one as the tilting term and the third one as the solenoidal term.

The friction term is missing on eq. (3.1) because it is assumed negligible in upper levels. Through a synoptic scale analysis, the most relevant term on eq. (3.1) at first order is the stretching, and thus eq. (3.1) can be approximated as:

$$\frac{\partial \zeta}{\partial t} + v \cdot \nabla \zeta = -\zeta \cdot D \quad (3.2)$$

Where $D = (u, v)$ represents the horizontal divergence and the ζ absolute vorticity. Equation (3.2) indicates that changes in the ζ are associated with the stretching/flattening of the atmospheric column as a consequence of the divergence/convergence in upper/lower levels (or vice versa). At a surface level, one can think that the left - hand - side of eq. (3.2) describes the propagation of Rossby waves, while the term on the right side represents the forcing of such waves.

In the tropics, the mid-troposphere diabatic heating is mainly balanced by the vertical velocity, so those regions of large latent heat release associated with tropical convection

will force large ascent at mid-levels, and hence divergent flow at upper tropospheric levels. Thus, a Rossby wave is generated by conservation of absolute vorticity. Focusing on eq. (3.2), in the tropics $\zeta$is generally small and near of the Equator it changes the sign. If one consider that the Rossby wave sources are given by $-\zeta \cdot D$, it would seem that, despite the clear evidence the observed tropical-extratropical teleconnection patterns, the anomalies of heating in the tropics should be ineffective in exciting waves and creating teleconnections to higher latitudes.

The solution to this apparent incoherence involves a more careful look at the vorticity equation, eq. (3.2). According to Helmholtz's theorem, the velocity field can be decomposed into a purely divergent part, $\vec{v}_\varphi$, and a purely rotational part, $\vec{v}_\psi$:

$$\vec{v}_\psi = k \wedge \nabla\psi \quad (3.3)$$
$$\vec{v}_\varphi = \nabla\varphi \quad (3.4)$$

where ψ and φ represent the streamfunction and velocity potential, respectively. From (3.3) and (3.4) one can define the relative vorticity as $\xi = \nabla^2\psi$ and the horizontal divergence as $D = \nabla^2\varphi$. Assuming $\vec{v} = v_\psi + v_\varphi$, eq. (3.2) can be rewritten as:

$$\frac{\partial\zeta}{\partial t} + \vec{v}_\psi \cdot \nabla\zeta = -\zeta \cdot D - \vec{v}_\varphi \cdot \nabla\zeta \quad (3.5)$$

Equation (3.5) represents the correct partitioning between Rossby wave propagation terms, which involve just the rotational part of the wind field (on the left hand side) and the forcing terms, involving the divergent part of the wind (on the right side). Therefore, the Rossby wave propagation is the result of the advection of absolute vorticity by the rotational part of the wind field. The extra-term, $\vec{v}_\varphi \cdot \nabla\zeta$represents the absolute vorticity advection by the divergent part of the wind and is not necessary small, although generally $|\vec{v}_\varphi| << |\vec{v}_\psi|$. The reason behind $\vec{v}_\varphi \cdot \nabla\zeta$ and $\vec{v}_\psi \cdot \nabla\zeta$being comparable is because the rotational part of the wind $\vec{v}_\psi$ is generally parallel to contours of constant ζ, therefore,

perpendicular to $\nabla\zeta$. The forcing terms are jointly referred to the "Rossby source term" S, which may be rewritten as:

$$S = -\nabla \cdot \left(v_\varphi \zeta\right) \quad (3.6)$$

One can now clearly see that the tropical diabatic heating can excite a Rossby wave even when ζ is often small in the surrounding of the tropical heating.

As an example, shaded regions on Figure 3.7 show the mean vertical integral of the diabatic heating during the austral summertime. The divergent flow is largest around the edge of the heating region (brownish colors on Figure 3.7), outside the region where divergence is large. The gradients of ζbecome large as one approach the subtropics (see contours on Figure 3.7), where S can be large. As result the Rossby waves are generated in the subtropics one or two thousands kilometers from its forcing (the released diabatic heating in the tropics). This is a consequence of the absolute vorticity spatial distribution and the divergent part of the flow (James I, 1995; Chapter 8).

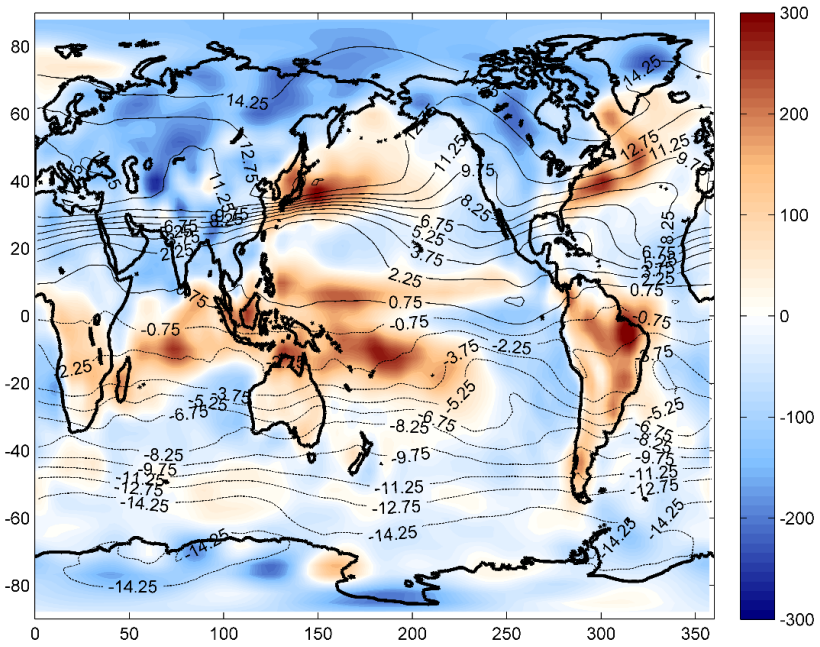

Figure 3.7. Mean vertical integral of the diabatic heating (W/m^2) during the austral summertime (DJF) over the period 1979-2001 (shaded regions). Data from NOAA NCEP

CDAS-1 (Kalnay et al., 1996). Mean absolute vorticity during the austral summer over the period 1979-2006 (contours). It is computed from the daily horizontal wind field from ERA Interim reanalysis data (Dee et al., 2011).

4| Complex network's analysis of oceans' influence on spring time rainfall variability over SESA during the 20th century[1]

The goal of this chapter is to investigate how the sea surface temperature (SST) anomalies in different basins can interact with each other and, in turn, collectively induce precipitation (PCP) variability over SESA. To address this issue we focus on the detection of periods where the tropical oceans and SESA PCP were most connected (synchronization periods) during the last century. We also compare them and hypothesize the possible physical mechanism through which the tropical oceans interact among them and influence SESA PCP.

This chapter is organized as follow: on section 4.1, we present a review of the main physical mechanisms for tropical and extratropical climate teleconnections. On section 4.2, we introduce the methodology applied and the data considered to address this work. On section 4.3, we show the characteristics of the climate network constructed, compare

[1] This work has been published on International Journal of Climatology under the reference: Martín-Gómez, V., and Barreiro, M. (2016). Analysis of oceans' influence on spring time rainfall variability over Southeastern South America during the 20th century. *International Journal of Climatology*, *36*(3), 1344-1358.

simulated and observed results and focus on the detection of synchronization periods. On section 4.4, we discuss possible physical mechanisms that characterized the interaction among the oceans and their influence over SESA PCP during each synchronization period, and finally, on section 4.5 we summarize the main results.

4.1. A review of the tropical and extratropical teleconnections.

Several studies have already shown that SESA PCP variability is influenced by the tropical Pacific, Atlantic and Indian oceans and that about 40% of SESA annual mean PCP variability is caused by variations in the tropical SST (Seager *et al*., 2010). As it was previously mentioned, the tropical oceans influence rainfall variability in the subtropics through different mechanisms, including the generation of quasi-stationary Rossby waves that propagates to higher latitudes (e.g. Vera et al., 2004) and anomalous changes in the Hadley and Walker regional cells (Ambrizzi et al., 2004).

The link between El Niño-Southern Oscillation (ENSO) and PCP over SESA is historically strongest in austral spring, weaker in summer and stronger again in fall (Grimm *et al*., 2000; Barreiro, 2010). The mechanisms through which El Niño influences SESA PCP involve both upper and lower-level atmospheric circulation anomalies. During El Niño the strengthening and meandering of the subtropical jet in upper-levels due to Rossby wave trains propagating from the equatorial Pacific increases the baroclinicity and the advection of cyclonic vorticity over SESA (Yulaeva and Wallace, 1994; Grimm *et al*., 2000). In lower-levels the northerly flow from the Amazon basin strengthens, increasing the availability of moisture south of 20ºS (Silvestri, 2004). This configuration enhances PCP over SESA during a warm ENSO event. During high austral summer the subtropical jet moves poleward, weakening the upper level mechanism and the signal weakens. In the later austral summer the signal strengthens again and, if only El Niño events that last until the following May are considered, there is a significant

positive anomaly in the region during fall that induces floods of the Parana river (Camilloni and Barros, 2003).

Some studies have presented evidence of a possible connection, which is not yet fully understood, between the tropical South Atlantic Ocean and PCP over SESA. Diaz *et al*., 1998 found a simultaneous correlation between increased PCP anomalies over SESA and warm anomalies off southeastern Brazil and the equatorial Atlantic during late spring and early summer. However, Robertson *et al*., 2003 found a very weak response on PCP and surface temperature over SESA using model simulations forced with prescribed patterns of south Atlantic SST anomalies. More recently, Barreiro 2010 showed for first time that the south Atlantic can play a secondary role in affecting climate anomalies over SESA through the modulation of the persistence on the ENSO influence. He found that the ocean off Brazil and Uruguay responds to ENSO signal by warming (cooling) during warm (cold) ENSO events through changes in the surface heat fluxes. This oceanic warming alters the evolution of the atmospheric anomalies through a thermodynamic feedback, resulting in increased persistence of the original atmospheric disturbance and thus affecting predictability over SESA.

According to some studies, the tropical Atlantic influences PCP over SESA mainly on multidecadal time scales while the tropical Pacific dominates the interannual band, together explaining most of the interannual to multidecadal variations (Seager *et al*., 2010). However, assuming linearity in the response, coexistence of an anomalously warm (cold) equatorial Pacific together with an anomalously cold (warm) Topical North Atlantic may interact constructively to intensify persistent wet spells (drought periods) over SESA and central Argentina (Mo and Berberly, 2011; Barreiro *et al*., 2014).

Other studies have shown that the Indian Ocean can also affect rainfall over South America (SA). For example, Chan et al., 2008 showed that PCP over subtropical La Plata

Basin during austral spring increases when the Indian Ocean Dipole (IOD) is in positive phase, a connection mediated through a mid-latitude wave train that emanates from the tropical Indian Ocean and propagates to SESA. The authors propose that the associated low-level anomalous anticyclone located off the coast of Brazil intensifies the tropical easterlies and strengthens the South American Low-Level Jet, increasing the availability of moisture, thus favoring the anomalously high PCP over Uruguay and northern Argentina.

In addition to influencing PCP over SESA, these tropical oceans interact among each other inducing SST anomalies in remote basins through atmospheric and oceanic teleconnections. In the case of the Pacific-Atlantic teleconnection, there are observational (Enfield *et al*., 1996; Enfield and Mayer, 1997) and modeling studies (Harzallah *et al*., 1996) which showed that ENSO has a significant remote influence on tropical Atlantic variability. The atmospheric teleconnection is established through anomalous surface heat fluxes as consequence of the changes in the trade winds and in the air-sea temperature difference associated with ENSO (Chiang and Sobel, 2002), in such a way that a warm tropical north Atlantic can be associated with positive SST anomalies in the eastern equatorial Pacific. The changes in the winds are established through the PNA teleconnection pattern induced by the tropical Pacific (e.g., Nobre and Shukla, 1996) and the largest response occurs during boreal spring (e.g., Enfield and Mayer, 1997; Saravannan and Chang, 2000). The influence of the tropical Pacific on the Atlantic is, however, fragile and depends on the pre-existing SST conditions in the latter basin (Chang *et al*., 2006). In turn, there are many studies suggesting a link in the opposite direction, that is, that temperature changes in the Atlantic Ocean can influence the equatorial Pacific (e.g., Dommenget *et al*., 2006; Rodriguez-Fonseca *et al*., 2009; Frauen *et al*., 2012; Yoo et al., 2013).

The interaction between El Niño-Southern Oscillation and the IOD is a controversial topic among the research community (Allan *et al*., 2001). Some studies established that IOD events are a physical entity inherent to the Indian Ocean and can evolve without external forcing from the equatorial Pacific (Saji *et al*., 1999; Webster *et al*., 1999), but there are also other studies which showed that some IOD events can co-occur with El Niño and even be triggered by Pacific forcing (Meyers *et al*., 2007; Annamalai *et al*., 2003; Wang and Wang, 2014). These latter studies showed that the weakening of the Walker circulation induced by El Niño generates anomalous surface easterly winds which shallow the thermocline off Java-Sumatra and enhance the SST cooling via upwelling of anomalous cold water (Annamalai *et al*., 2003; Wang and Wang, 2014).

There are also studies that investigate the impact of different El Niño events on the IOD separating El Niño into canonical El Niño (when the maximun SST anomalies are located in the eastern equatorial Pacific), El Niño Modoki I and II (when the maximun SST anomalies are in the central equatorial Pacific). They show that while the canonical Niño and El Niño Modoki I are related to a positive IOD, El Niño Modoki II is associated with a negative IOD, because different El Niños induce distinct changes (Wang and Wang, 2014). It is also important to note that besides El Niño, there are other external drivers that can also induce an IOD event, such as the Southern Annular Mode (Lau and Nath, 2004) and the monsoon (Fisher *et al*., 2005).

To our knowledge there are no studies in the literature that show a direct influence of the tropical north Atlantic SST anomalies on the tropical Indian Ocean. However, there are studies which analyze the influence of SST anomalies in the Atlantic Ocean on the ENSO-Indian monsoon interaction (Kucharski *et al*., 2007; Wang *et al*., 2009) and directly on the Indian monsoon. For example, Goswami *et al*., (2006) showed that the increase of the meridional temperature gradient over the northern hemisphere during the positive phase

of the Atlantic Multidecadal Oscillation (AMO) may extend the Indian monsoon, causing an increase of the seasonal mean Indian summer rainfall. The tropical SST expression of the AMO plays the dominant role in this teleconnection (Li *et al*., 2008). At the same time, Li *et al*. (2003) showed that a strong Indian monsoon may change surface winds leading to cold SST anomalies in the western Indian Ocean (through enhanced surface evaporation, ocean mixing, and coastal upwelling) and warm SST anomalies in the eastern Indian Ocean. Thus, the tropical north Atlantic may influence the Indian Ocean through changes in the monsoon.

All the aforementioned studies focus on the impact of a particular ocean basin (or a combination of two basins) on PCP over SESA or on the surface ocean conditions of another basin, no existing, to our knowledge, a study that addresses how the SST anomalies in different basins interact to induce PCP anomalies over SESA and neither how the interaction among oceans and their influence on PCP variability has evolved with time. Thus, the main goal of this chapter is to investigate the collective influence of the three tropical oceans (characterized by interannual phenomena) on PCP over SESA and how this influence has evolved during the 20th century. We focus on austral spring season because, as mentioned above, several previous studies have shown that rainfall is influenced by the tropical oceans exhibiting large variability on interannual to interdecadal time scales (e.g. Seager et al., 2010).

To address this issue we consider the interaction among oceans and their influence on SESA PCP from a complex network perspective. We construct a climate network following the methodology of Tsonis *et al*. 2007 considering different indices that characterize the tropical oceans: El Niño/Southern Oscillation (Niño3.4), the Tropical North Atlantic (TNA), and the Indian Ocean Dipole (IOD) as well as an index that characterizes PCP over SESA. These four climate indices will make up the nodes of the

climate network (see Figure 4.1). We investigate the collective behavior of the four network's nodes focusing on detection of synchronization events (when the network's nodes are most connected) and how this 'collective behavior' has evolved with time. The synchronization events are defined considering the mean distance of cross – correlation. Thus, this methodology allows to detect periods when the tropical oceans are more connected and active in influencing PCP over SESA.

4.2. Data and methodology

4.2.1 Data

We define the different tropical oceanic indices considering the monthly mean SST data from 1901 to 2005 of two different datasets: ERSSTv3b (Extended Reconstructed Sea Surface Temperature; Smith *et al.*, 2008; and Xue *et al*., 2003) with a resolution of 2º x 2º, and HadSST (Hadley Center Sea Surface Temperatures; Rayner *et al*., 2003) with a resolution of 1º x 1º. The PCP index is defined using the monthly mean observed data during the same period mentioned above from the GPCCv5 database (Global Precipitation Climatology Center; Schneider *et al*., 2011) with a resolution of 1º x 1º. Table 4.1 summarizes the indices considered in this study.

We also consider the simulated PCP field from an Atmospheric General Circulation Model (AGCM) forced with observed SST. In particular, we use the ICTP-AGCM (Kucharski *et al*., 2006; Molteni 2003) and construct an ensemble of 9 runs initializing the model with different atmospheric conditions, but all having the same SST as boundary conditions. The PCP index is considered as the ensemble mean PCP over the region of interest (see Table 4.1) and by construction it will mainly represent the oceanically-forced rainfall variability since, as several previous studies have shown, taking an ensemble of about 10 members is enough to filter out internal variability in most places (Saravanan

and Chang, 2000; Barreiro and Tippman, 2008; Barreiro, 2010). The ICTP-AGCM is forced with observed SST from the ERSSTv2 dataset. Smith *et al.*, 2008 showed that ERSSTv2 and ERSSTv3 are very similar, which is further substantiated by the strong similarity of the indices used in this study according to Table 4.2. Thus, the main difference in the networks constructed using observed and simulated data will arise due to differences in the evolution of PCP.

Given the larger similarity between ERSSTv2 and ERSSTv3b, the network constructed using the simulated rainfall will be mainly compared with the observed one constructed with ERSSTv3b. The network constructed with HadSST will be used to test the sensitivity of the network distance to observed SST.

Index short name	Long name index	Earth's region	
		Latitude range	Longitude range
NINO3.4	Niño3.4	5ºN-5ºS	170ºW-120ºW
TNA	Tropical North Atlantic	10ºN-30ºN	60ºW-30ºW
IOD	Indian Ocean Dipole	10ºS-10ºN 10ºS-0ºN	50ºE-70ºE 90ºE-110ºE
PCP	Precipitation Southeastern South America (only land areas are considered)	40ºS-25ºS	60ºW-50ºW

Table 4.1. Geographical regions of each index that make up our network's nodes. The indices are constructed averaging the SST or PCP anomalies in the specified regions. In the Indian Ocean Dipole case, the index is constructed as from the difference between the average in the western region and the average in the eastern region. Regions are plotted in Figure 4.1.

Pearson Correlation between each index from ERSSTv3b and the same index from ERSSTv2	Nino3.4	TNA	IOD
Pearson Correlation coefficient	0.99	0.99	0.98

Table 4.2. Pearson correlation coefficients between oceanic indices computed using ERSSTv3b and ERSSTv2 datasets during the period 1901-2005.

4.2.2. Methodology

The methodology consists of several steps:

First, we construct the climate indices by latitudinal and longitudinally averaging SST and PCP in the different regions considered (see Table 4.1 and Figure 4.1). We also eliminate the trend of the four time series and compute monthly anomalies, removing the climatological cycle from 1901 to 2005. In the case of the IOD index, we subtract the average between the two boxes to construct the index. The indices are normalized by their respective standard deviations computed considering the period 1901-2005.

Second, we consider individual trimesters to construct the networks: September – November (SON) for the case of El Niño index and October – December (OND) for the rest of the indices (TNA, IOD and PCP). Before taking a 3-months mean and in order to avoid aliasing effects, we first apply a low-pass Lanczos Filter (Duchon, 1979) with cutoff frequency of 1/12 to the monthly mean time series. Therefore, the time series have 105 values, one per year.

As mentioned in the introduction, SESA PCP in OND shows large variability on different time scales including interannual to interdecadal (Seager et al., 2010). Also, it is during this season when the teleconnection between Niño3.4 and SESA PCP is well established and when the IOD takes place and influences SESA PCP variability (Barreiro, 2010; Li *et al*., 2003 and Chan *et al*., 2008). The literature mentioned in the introduction reveals that ENSO could induce SST anomalies in other tropical basins with a lag that varies from

1 to several months. Thus, we established a lag of one month between the Niño3.4 index and the rest of the network nodes to allow the Atlantic and Indian Oceans to respond to the atmospheric anomalies generated by the equatorial Pacific. At the same time, results are not very sensitive to the election of Niño3.4 calculated on SON or OND because the index is computed by averaging the SST anomalies of three consecutive months. Monthly persistence is very large so that changes between SST in September and December in that region of the Pacific Ocean are small, and there is no change in the phase of El Niño phenomenon. Therefore, El Niño index in SON is very similar to that one in OND.

Third, following the methodology of Tsonis *et al.* 2007 we construct the network considering the mean network distance as synchronization measure. Mathematically, the mean network distance is defined as:

$$d(t) = \frac{2}{N(N-1)} \sum_{i<j} \sqrt{2\left(1 - \left|\rho_{ij}^{t}\right|\right)} \quad (4.1)$$

where t denotes the time in the middle of a sliding window of width Δt=11 years, N represents the number of network's nodes that we take into account to construct the climate network (in our case N=4, TNA, IOD, PCP and Niño3.4) and ρ_{ij}^{t} is the cross correlation coefficient between nodes i and j in the interval $[t - \frac{\Delta t}{2}, t + \frac{\Delta t}{2}]$. Note that to compute the mean network distance, for each sliding window we introduce the six values of the correlation coefficients that correspond to the six possible pairs of network's nodes, independently of whether they are significant or not because all of them contribute to the degree of synchronization of the network with higher or lower values of the distance. The time step for the sliding window is 1 year. The window length selected here is a compromise between being long enough to estimate correlations, but not too long for

interdecadal variability modes to influence the behavior. The observed synchronization periods are not very sensitive to a window size in the range of 9 to 13 years.

Climate teleconnections may in principle have a non-linear nature. Nevertheless, Donges et al., 2009 and Arizmendi et al., 2014 showed that linear similarity measures give very close results to nonlinear measures, such as mutual information, when characterizing atmospheric teleconnection phenomena. Moreover, in our case, the length of the sliding window precludes the computation of mutual information with enough reliability. Nonetheless, as a first order to test for nonlinearity, the network distance was also computed considering Spearman rank correlation. We found that the network distance is similar independently on the correlation used except during the last decade of the 20th century, when the network distance computed with Spearman correlation does not show statistically significant synchronization among the network's nodes (Figure 4.2). This period includes the strong El Niño of 1997 which acts as an outlier strongly influencing Pearson correlation. The similarity in the evolution of both network distances during the first 90 years of the last century suggests that Pearson correlation is a valid measure of interdependence to represent climate teleconnections, and our study will be based on this correlation coefficient.

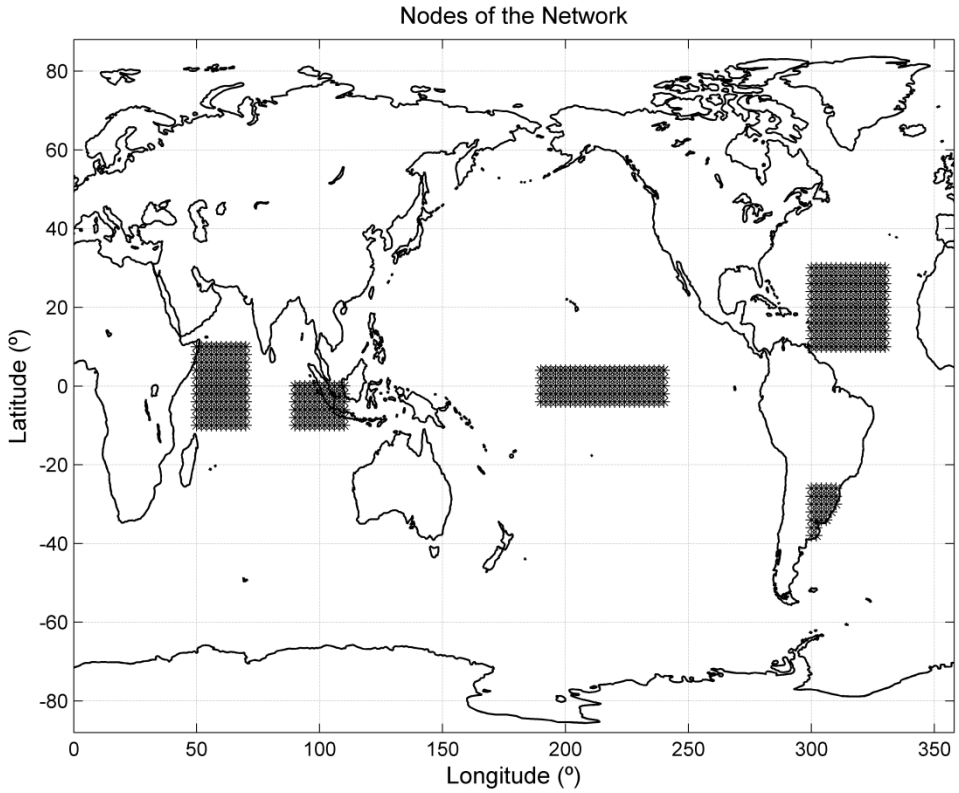

Figure 4.1. Regions that represents the climate indices: Indian Ocean Dipole (IOD) over the Indian Ocean, Niño3.4 over the central equatorial Pacific Ocean, the Tropical North Atlantic (TNA) and the PCP over SESA.

The mean network distance as a measure of synchronization is useful to study and describe the variations in the network's features. Note that the network is completely synchronized when the distance is zero and disconnected when the distance is $\sqrt{2}$ (uncorrelated nodes). In turn, equation (4.1) uses the absolute value of cross correlation because we are interested in the intensity of the interaction between the two nodes, which is independent of the correlation sign.

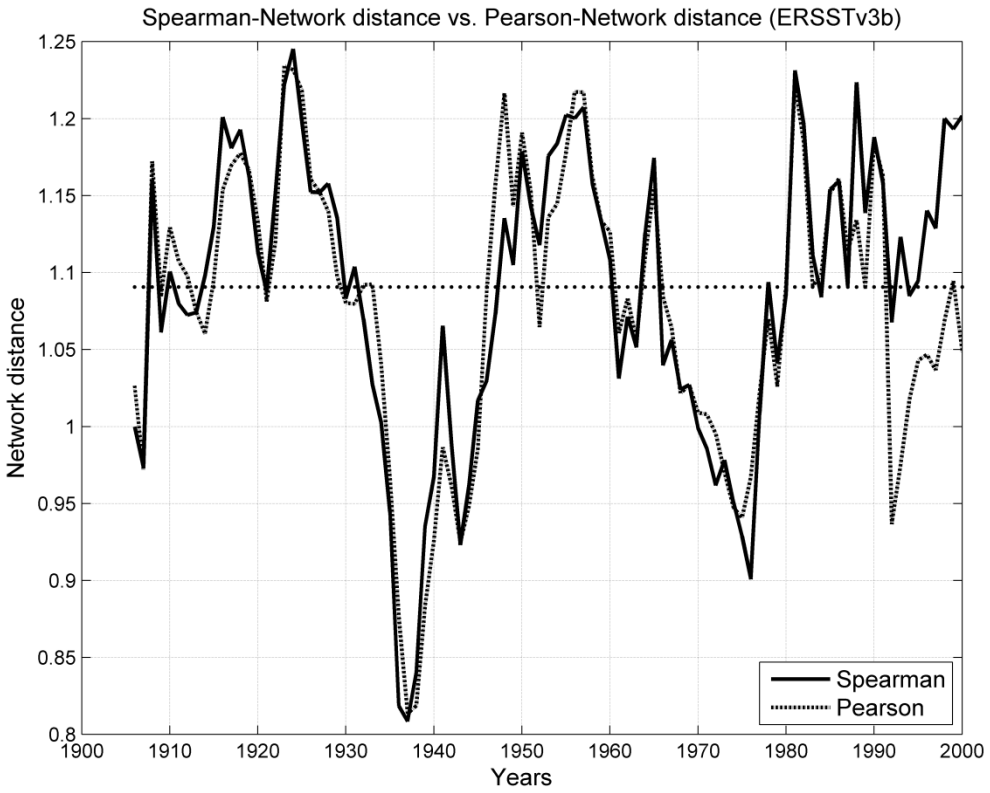

Figure 4.2. Network distance computed considering Spearman rank (continue line) and Pearson (dot line) correlations coefficients from ERSSTv3b indices. For each time step, the network distance is calculated considering the definition given by Tsonis *et al*., (2007) and a sliding window of 11 years length. El Niño index in centered on September-October-November (SON), and the rest of the indices on October-November-December (OND).

Fourth, to compute the statistical significance of the mean network distance we consider a Monte Carlo method employing the following criterion. We first compute the autocorrelation coefficient at 1 year lag of each index (remember that each index has one value per year and represents the seasonal mean), and consider as red noise those with autocorrelation coefficient significant at 95% level in a one-tailed t-test (white noise in the opposite case). Following this criterion, only the TNA can be considered as red noise, while the rest of the indices are white noise. Then, we generate 1000 surrogate time series

of each index under these null hypotheses and compute the network distance time series considering a sliding window of 11-years length, as done for the observed indices. In this way, we construct 1000 surrogate time series of the mean network distance, which allows determining the 5% level. We consider that there is a statistically significant synchronization event when the mean network distance is below this threshold. This procedure is carried out considering the observed PCP and the two observed SST datasets (ERSSTv3b and HadSST), as well as for the ICTP-AGCM's ensemble mean rainfall. We will see below that the network constructed with the model's output can reproduce the observed synchronization events. This means that the model reproduces well the observations and its output can be used to study the global circulation anomalies in each synchronization period.

4.3 Network's characteristics

In this section, we describe the main features of the network, compare the observed and simulated results, and define the synchronization periods that characterized the last century. Lastly, we determine which nodes had a statistically significant influence on SESA PCP variability and how this changed from one synchronization period to another. The characteristics of the network are studied using the time series of the mean network distance plotted in Figure 4.3. The blue, red and green lines represent the mean network distance computed from ERSSTv3b, HadSST and ICTP-AGCM's outputs, respectively, and the horizontal black dot line is the threshold level.

4.3.1 Variability of the network distance and synchronization periods

The network distance is characterized by large interannual and interdecadal variability, existing three periods in which the observed (ERSSTv3b and HadSST) and simulated (ICTP-AGCM) network distances computed using Pearson correlation evolve similarly

and present synchronization (Figure 4.3). Focusing on the ERSSTv3b network distance it is possible to distinguish that the first period occurs from 1933 to 1945 and the second period covers 1966-1978. The last synchronization period (during the ‘90s) is discarded since the mean network distance computed using the Spearman correlation does not show synchronization among the network’s components (Figure 4.2, black dot line).

To establish the synchronization periods we selected a period of years that fulfill two criteria: (1) the mean network distance is under the threshold level and (2) if we move the true window that represents the synchronization period one year to the left and one year to the right, the interacting nodes do not change (that is, the correlation coefficients that are statistically significant in the centered-window, remain statistically significant for the right/left moved-windows).

The fact that the two observed networks (red and blue curves on Figure 4.3) evolve in a similar way during most of the period of study guarantees that the synchronization events are independent of the chosen dataset. Nevertheless, the strength of the synchronization depends on the SST dataset used, being stronger for the ERSSTv3b (see first and second synchronization periods in Figure 4.3). Finally, it must be noted that during the first thirty years, the two observed datasets evolve dissimilarly, which can be due to the scarcity of observations.

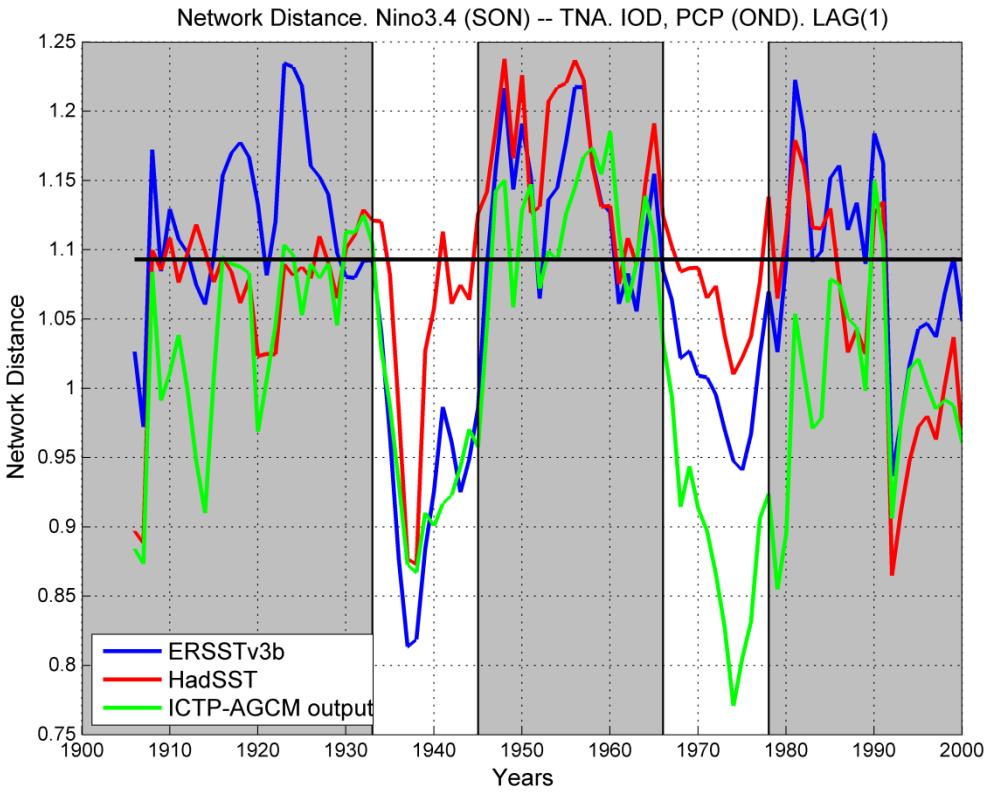

Figure 4.3. Network distance time serie during the last 20th century. Blue, red and green lines represent the mean distance computed from ERSSTv3b, HadSST and ICTP-AGCM's output, respectively. The horizontal black dot - line represents the threshold level. Whereas the ERSSTv3b and HadSST network distances are computed from the observed PCP index, the ICTP-AGCM network distance is computed from the PCP ensemble mean. For each time step, the network distance is calculated considering the definition given by Tsonis *et al*., (2007) and a sliding window of 11 years length. El Niño index in centered on September-October-November (SON), and the rest of the indices on October-November-December (OND). The synchronization periods are marked by the white regions.

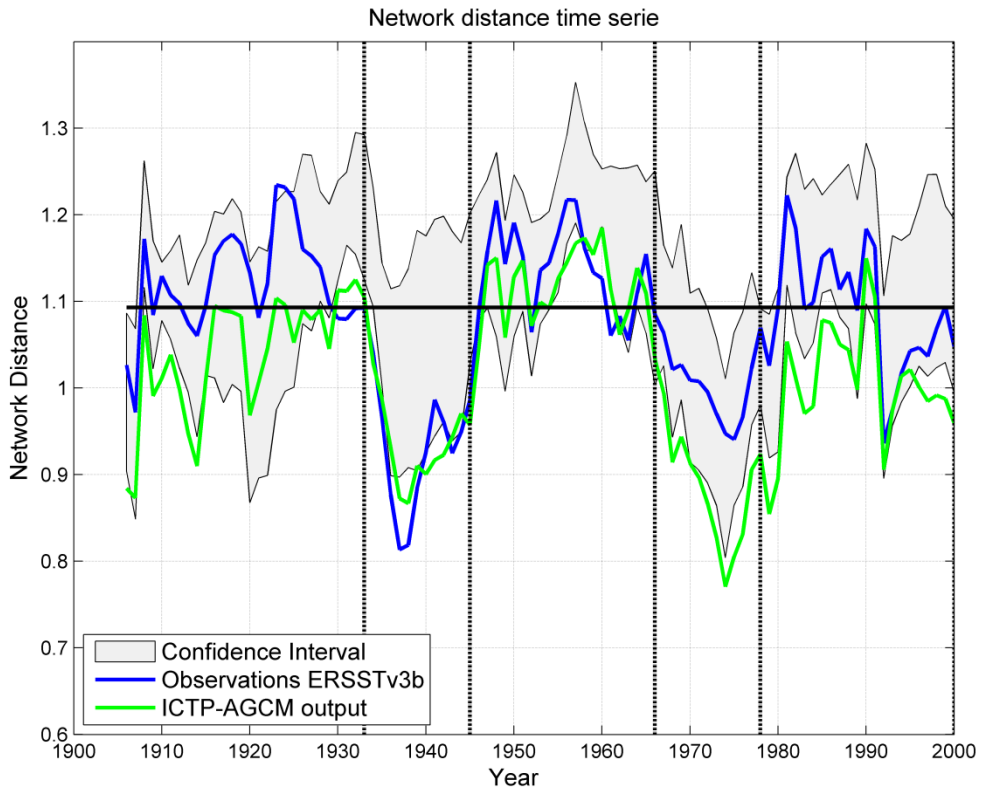

Figure 4.4. Simulated confidence interval for the network distance time series from 1901 to 2006. The blue and green lines represent the observed and simulated network distance time series respectively. The observed network distance is calculated from ERSSTv3b dataset and the simulated considering the PCP from the ensemble mean.

4.3.2 Relative weight of the nodes in synchronization periods

The time behavior of the network distance calculated using simulated PCP tends to follow the one constructed with observed PCP (green and blue lines, Figure 4.3). However, while there are periods in which the amplitude of the simulated network distance (green line) is very similar to that using observations (for example, first synchronization period), there are others in which this is not the case (for example, the second synchronization period). As noted before, the main difference between the observed and simulated network distances should arise due to the PCP index, because whereas in the simulated case the PCP index contains mainly the oceanically-forced component, the observed PCP index

contains both, the internal variability and oceanically-forced signals. Moreover, model biases may also induce differences between observed and simulated PCP.

To further analyze the representation of the network distance by the model, we compute the network distance for each one of the 9 PCP ensemble members of the experiment and define a confidence interval given by the maximum and minimum values for each 11 years window (Figure 4.4). Focusing on the ERSSTv3b-network distance (blue line on Figure 4.4), overall the observed network distance falls within the confidence interval except during the first synchronization period, but even then, it is possible to see that the observed and ensemble-mean simulated network distances are very close to each other. A similar situation occurs during 1957-1962. The only point where the behavior could be considered different is 1923 when the observed network distance is out of the confidence interval and does not coincide with the simulated network distance. In any case, it is only one point and one that is not that important for our study because is not within a synchronization period.

Figure 4.4 also shows that in both synchronization periods the magnitude of the simulated network distance (green line) is just outside the confidence interval, suggesting that large internal atmospheric variability within the ensemble is filtered out in the average procedure. By construction, the simulated network distance (green line) can stay inside or under the confidence interval, but never above. This is because the ensemble mean PCP index has filtered most of the internal atmospheric variability signal, which would act as noise in the PCP time series decreasing in average the cross-correlation between the PCP index and any of the oceanic indices.

Looking more closely at the synchronization periods, in the first one the amplitude of the simulated and observed network distances is very similar. Such a result could be a consequence of SESA PCP not being influenced by the tropical oceans. In this situation,

the correlation coefficients between the tropical ocean indices and the PCP would be close to zero and the similarity is obvious given that both (observed and simulated network distances) use observed SSTs. To check whether this is the case, we computed relative weights in order to determine the importance of individual nodes in the network. For example, for rainfall we define the relative PCP weight (RPW) as:

$$\mathrm{RPW} = \frac{\frac{\sqrt{2}}{2} - d_{\mathrm{pcp}}}{\sqrt{2} - d} \quad (4.2)$$

where d_{pcp} represents the network distance calculated considering only the correlation coefficients between the PCP index and the tropical ocean indices in equation (4.1). The maximum and minimum values of the RPW are one and zero respectively. Higher values of the RPW will be associated with larger influence of the tropical oceans on rainfall. RPW=1 takes place when d_{pcp}=0 (correlation coefficient between each one of the oceanic indices and the PCP index are 1 or -1) and the tropical oceans are completely disconnected among them. RPW=0 means that SESA PCP is completely disconnected from the tropical ocean indices$\left(d_{\mathrm{pcp}} = \frac{\sqrt{2}}{2}\right)$. Analogously, it is possible to construct time series that describe the relative weight of each oceanic index.

Figure 4.5 shows the relative weight of each one of the network's nodes. The RPW is represented by a blue line and shows relatively large values during the first synchronization period (1933-1945), suggesting that the tropical oceans influence SESA PCP. In fact, the mean value of the RPW=0.58 represents the second largest value of node's relative weights during this period (after Niño3.4 index, see Table 4.3). Comparing the values of the relative weight of each index during this period it is clear that Niño 3.4 was the most connected node of the network, followed closely by SESA PCP (see Table 4.3). Thus, PCP has high correlation values with the other network's nodes and the fact

that the magnitude of the network distance simulated by the model follows the observed ones (see Figure 4.3 or 4.4) suggests that the oceanically-forced signal on rainfall was strong during this period and the ensemble mean PCP represents it correctly.

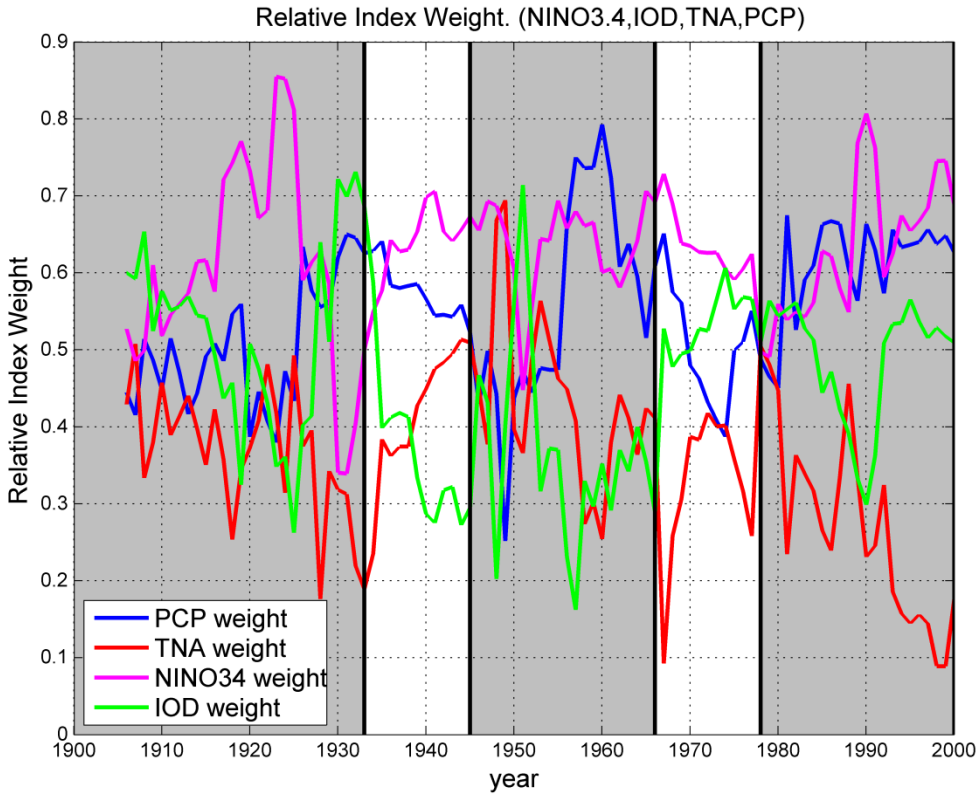

Figure 4.5. Relative Index time series. This parameter indicates the importance of the each node in the network and is enclosed between zero and one. Higher values of the relative weight are associated with higher importance of the particularly index in the network. We compute this parameter considering the observed data from ERSSTv3b. The synchronization periods are marked with the white regions.

During the second synchronization period observed and simulated network distances have different magnitudes. In this period the observed network distance is well within the confidence interval, suggesting a weak oceanically-forced signal embedded in large internal atmospheric variability. As before, Niño3.4 is the most connected network's node, but now the IOD is as important as the PCP index (see Table 4.3). In comparison

with the ‘30s, the connectivity of SESA PCP index decreases in the ‘70s (and the RPW shows a relative minimum, Figure 4.5). Also, we can see that whereas the IOD has high weight in the network during the second synchronization period, the weight of the TNA is slightly larger in the first period (see Table 4.3). Finally, if we focus on the mean values of the relative weights computed over the whole 20th century, Niño3.4 was the most connected network’s node, followed by the PCP, IOD and TNA indices (see Table 4.3), suggesting that ENSO has a vital importance in the global network. In turn, from the correlation values of the tropical ocean indices and SESA PCP it is clear that the equatorial Pacific is the node that had strongest influence on rainfall variability over SESA during the last century (see Table 4.4) which is consistent with the literature.

Relative Weight	**mean 30s**	**std 30s**	**mean 70s**	**std 70s**	**mean 20th**	**std 20th**
PCP	0.58	0.04	0.51	0.08	0.55	0.10
TNA	0.41	0.10	0.35	0.10	0.36	0.12
IOD	0.39	0.13	0.52	0.08	0.46	0.12
NINO3.4	0.61	0.06	0.63	0.06	0.63	0.09

Table 4.3. Mean of the relative weight during ‘30s, ‘70s and whole the 20th century together with the corresponding standard deviations for each network’s node.

	NINO3.4-PCP	**TNA-PCP**	**IOD-PCP**
Pearson correlation	0.64	0.14	0.38

Table 4.4. Pearson correlation values between each one of the oceanic indices and SESA PCP over whole the 20th century. At 95% significant level in a one-tailed t-test, the threshold level is: 0.16.

Lastly, it is important to note that a large relative weight of rainfall does not necessarily translate into a small network distance, as happened during 1955-1965. This suggests that during this period the interaction among the oceans is weak.

4.3.3 Node connection during synchronization periods

Up to this point we have found that during the 20th century there were two synchronization periods: (1933-1945) and (1966-1978). The following step is to determine which nodes were "actually connected", that is, interacting among each other during each synchronization period. Although the mean network distance was computed considering the correlation of the six possible pairs of network's nodes, because all of them contribute to the degree of synchronization of the network, this does not mean that the six possible pairs always present statistically significant correlations. Two nodes will be "actually connected", and therefore interacting between each other, if the correlation coefficient is statistically significant. Therefore, to determine which nodes were actually interacting, we compute the Pearson correlation coefficients between each pair of network's nodes during each synchronization period considering model simulations and check their statistical significance using a Monte Carlo method based on the generation of 10000 surrogates time series. Surrogates of each index are constructed by random permutation taking blocks of one element (value) of the time series for the case of the Niño3.4, IOD and PCP, and blocks of two values of the time series for the case of the TNA index in order to maintain the observed serial autocorrelation (i.e., to preserve the observed red noise behavior of the TNA index). The criterion that establishes if two network nodes are interacting is the following: (1) We first take a period ("window") that corresponds with the years in which the network distance is under the threshold level in Figure 4.4 and compute all the correlation coefficients between the network's nodes. (2) Afterwards, we move the centered-window one year to the left and one year to the right, and compute again the correlation coefficients among the nodes for each moved-window (see tables 4.5 and 4.6). We say that two nodes are interacting if the three values of the cross-correlation remain statistically significant. According to this procedure for the second

synchronization period we will not consider the interaction of PCP-TNA as a network link, since the interaction between both nodes does not remain significant for the 3 windows considered (see Table 4.6).

Tables 4.5 and 4.6 show that even though all nodes have at least one connection in each synchronization period, the characteristics of the network are different. During the '30s, Niño3.4 is connected to all the rest of the nodes and there is a link between PCP and TNA. During the '70s, Niño3.4 is also connected to all the nodes, but the PCP became connected to the IOD. From the point of view of PCP over SESA, during the '30s the equatorial Pacific and the tropical north Atlantic dominated the oceanically-forced component of the variability. On the other hand, during the '70s the TNA does not play a role, and the Indian Ocean becomes connected to rainfall over SESA, in addition to the Pacific. This result can also be observed in Figures 4.6 (a) and (c), which represent the correlation map between the PCP index and the SST anomalous field in each synchronization period, indicating the regions of the ocean that influence rainfall variability over Southeastern South America.

Pearson Correlation Threshold: 0,48	(1932-1944)	(1933-1945)	(1934-1946)
NINO3.4-PCP	0.68	0.70	0.69
NINO3.4-TNA	0.68	0.68	0.67
NINO3.4-IOD	0.72	0.72	0.57
IOD-TNA	0.19	0.18	-0.04
IOD-PCP	0.12	0.11	-0.02
PCP-TNA	0.92	0.93	0.87

Table 4.5. Pearson correlation coefficients for the different windows that represent the first synchronization period. Threshold level: 0.48 at 95% significant level in a Monte Carlo test based on the generation of 10000 surrogate time series.

Pearson Correlation Threshold: 0,48	(1965-1977)	(1966-1978)	(1967-1979)
NINO3.4-PCP	0.86	0.88	0.88
NINO3.4-TNA	0.60	0.57	0.59
NINO3.4-IOD	0.56	0.61	0.61
IOD-TNA	0.35	0.36	0.38
IOD-PCP	0.65	0.66	0.66
PCP-TNA	0.47	0.46	0.51

Table 4.6. Same as Table 4.5, but for the second synchronization period.

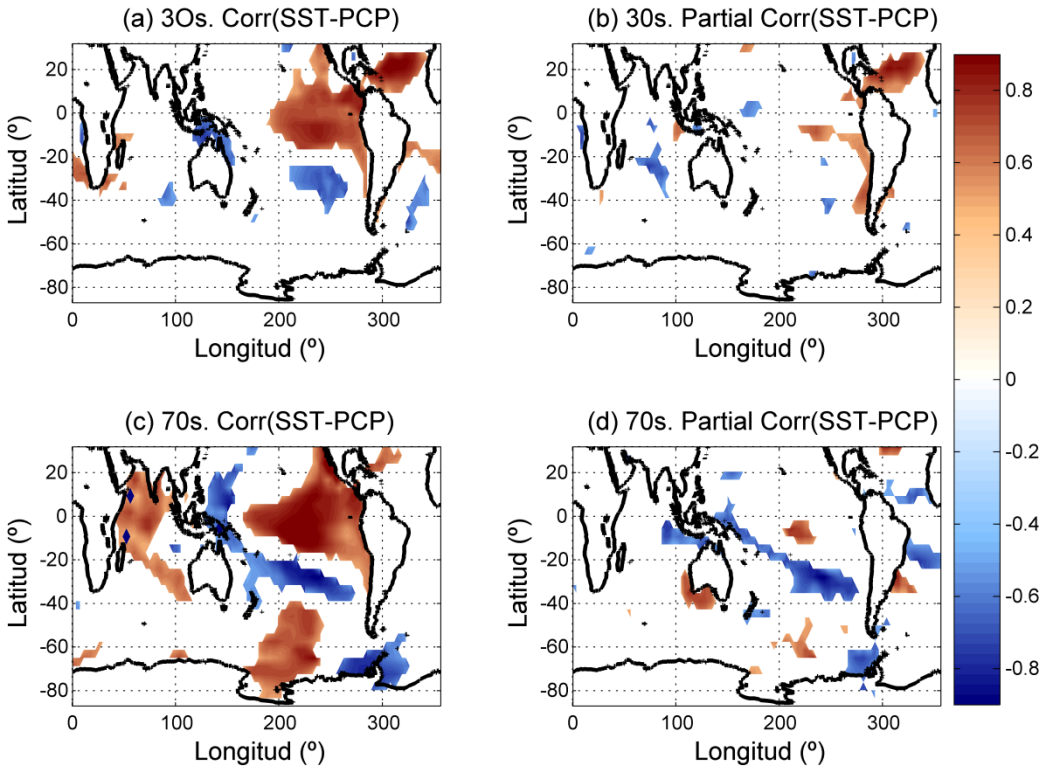

Figure 4.6. Correlation maps between PCP index (OND) and the SST anomalies centered on OND: (a) in the 30s and (c) in the 70s. Partial cross correlation maps between PCP index (OND) and the SST anomalies centered on OND maintaining Niño3.4 index (SON) constant: (b) in the 30s and (d) in the 70s.These maps were computed considering ICTP-AGCM output. Shown values exceed 95% level of confidence from one tailed t-test.

In the following section we hypothesize the possible physical mechanisms that characterized the interaction among the nodes of the network important for rainfall over SESA during synchronization periods based on the literature. We employ the ICTP-AGCM's output since, as we saw, this model reproduces well the observations and allows to better characterize the oceanically-forced atmospheric circulation anomalies.

4.4 Discussion of teleconnections in synchronization periods

4.4.1 Period (1933-1945)

The oceanic nodes that had an important role on rainfall variability during the period 1933-1945 are Niño3.4 and the Tropical North Atlantic (see Figure 4.6(a)).

Link Niño3.4-TNA: There are two different processes through which a warm anomaly in the equatorial Pacific can influence the TNA: a weakening of the trades which decreases the oceanic heat loss (e.g. Enfield and Mayer, 1997) and the tropospheric temperature warming bridge (Chiang and Sobel, 2002). The regression maps onto Niño3.4 show a small warming of the tropical north Atlantic accompanied by weak decreased trades (Figures 4.7 (a) and (c)). The small TNA response might be a consequence of the small time lag allowed for the ocean response (1 month), instead of a typical scale of one season (e.g. Enfield and Mayer, 1997; Saravanan and Chang, 2000).

Link Niño3.4-PCP: As mentioned in the introduction, the mechanisms through which El Niño influences SESA involve both upper and lower-level atmospheric circulation anomalies. In upper-levels the Rossby wave trains propagating from the equatorial Pacific increase the baroclinicity and the advection of cyclonic vorticity over the region (Yulaeva and Wallace, 1994; Grimm *et al.*, 2000). This can be observed in the regression map of the geopotential height onto the Niño3.4 index (Figure 4.7 (b)), which shows the presence of a through-ridge system over subtropical South America. At the same time, in lower-

levels there is an increase of the northerly transport of moisture into the region because of a strengthening of the southward wind (Figure 4.7 (d), in agreement with Silvestri, 2004). The combination of these two factors favors an increase of PCP over SESA.

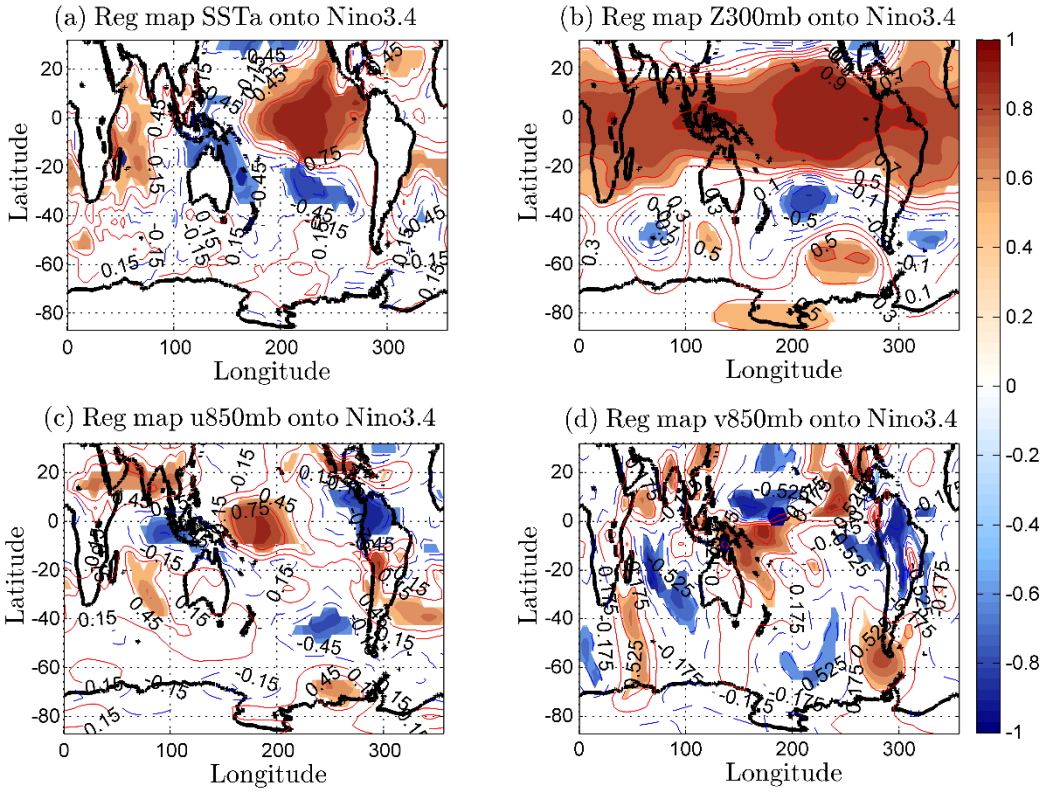

Figure 4.7. Regression map of the El Niño3.4 index (centered on SON) with: (a) SST anomalies, (b) geopotential height 300mb (Z300mb), (c): zonal wind anomalies in 850mb (u850mb) and (d) meridional wind in 850mb (v850mb). The SST, Z300mb, u850mb and v850mb are centered on OND. First synchronization period (1933-1945). Shaded regions represent values higher than 95% confidence level for one tailed t-test. Maps computed from the ICTP-AGCM outputs.

Regarding the interaction between the TNA and PCP, it is important to note that the correlation is approximately 0.9, larger than the one between PCP and Niño3.4. Also even after El Niño signal is removed (Figure 4.6 (b)), the SST anomaly in the TNA is still significantly correlated with rainfall over SESA. This suggests that the link between TNA

and PCP is direct and that the SST anomalies in the TNA cannot be completely explained by ENSO forcing. To look at the influence of TNA directly onto SESA we performed partial regression maps of velocity potential at 300mb, and meridional wind at 850mb onto the TNA index maintaining Niño3.4 index constant (Figures 4.8 (b) and (c), respectively). On Figure 4.8 (b) we found that the velocity potential in upper-levels shows an anomalous convergence over the northeast Amazon Basin. At the same time, Figure 4.8 (c) shows strong northward anomalous winds over the TNA and southward low-level winds over subtropical South America, which increases the northerly transport of moisture toward SESA. This result is in agreement with Yoon and Zeng (2010), who suggested that a warm TNA induces anomalous convergence of low-level winds and upward vertical motion. This divergent circulation results in anomalous divergence at low-levels over the Amazon basin that reduces rainfall there and strengthens the southerly winds that transport moisture toward SESA (Figure 2.5 from Yoon and Zeng (2010)). However, in our results the changes in the meridional wind component and the velocity potential at 300mb over the Amazon region are not significant and further work is needed to understand the influence of the TNA on rainfall over SESA.

Finally, regarding the combined influence of these two tropical indices (Niño3.4 and TNA) on SESA PCP, we hypothesize that during the first synchronization period a warm TNA in conjunction with a warm equatorial Pacific favors a larger increase in the northerly winds that bring moisture from the Amazon toward SESA, thus further increasing rainfall there.

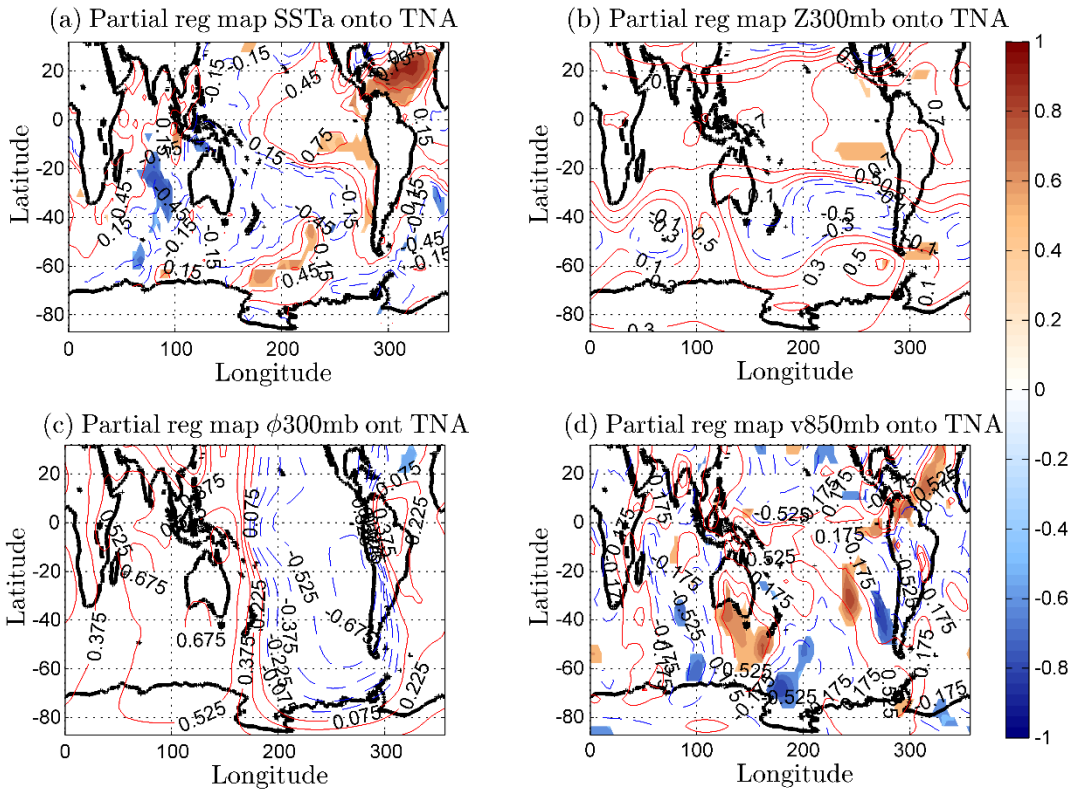

Figure 4.8. Regression map of the TNA index (centered on OND) with: (a) SST anomalies, (b) geopotential height 300mb (Z300mb), (c) velocity potential at 300mb (φ300mb), (d): meridional wind at 850mb (v850mb). The SST, Z300mb, φ300mb and v850mb are centered on OND. First synchronization period (1933-1945). Shaded regions represent values higher than 95% confidence level for one tailed t-test. Maps computed from ICTP-AGCM output.

4.4.2 Period (1966-1978)

In this case, the oceanic nodes that had an important role on rainfall variability are Niño3.4 and the Indian Ocean Dipole (see Figure 4.6 (c)).

Link Niño3.4-PCP: The interaction between El Niño and the precipitation over SESA is similar to the previous case since the two favorable conditions to the increase for precipitation over the region of study are present (Figures 4.9 (b) and (d)).

Link IOD-PCP: In this period the Indian Ocean Dipole appears like an important network's node, having a significant link with the PCP node (Figure 4.6 (c)). This link would suggest an influence of the Indian Ocean on rainfall in SESA. However the partial cross - correlation map between the PCP index and the SST field maintaining the Niño3.4 index constant (Figure 4.6 (d)), shows that the correlation between the PCP and SST over the Indian Ocean is not significant, suggesting that the appearance of this link could be due to the fact that both nodes have a common forcing: El Niño. Another possibility is that the Indian Ocean warming, as consequence of the Pacific forcing, influenced the rainfall over SESA through the eastward propagation of Rossby waves, a mechanism already proposed by Saji *et al*., (2005) and Chan *et al*., (2008). In fact, the regression map of 300mb geopotential height shows significant anomalies in the southeastern Indian Ocean and the extratropical atmosphere (Figure 4.9 (b)) that were barely present in the '30s (Figure 4.7 (b)). This Rossby wave train may interact with the one forced by the tropical Pacific, and together may favor better conditions for increased PCP over SESA (in agreement with the previous works of Saji *et al*., 2005 and Chan *et al*., 2008).

Link Niño3.4-IOD: The connection between both oceans (equatorial Pacific and Indian) is established through anomalous winds (Annamalai *et al*., 2003; Wang and Wang, 2014). During the '70s, the regression map of the Niño3.4 index and the 850mb zonal wind (Figure 4.9(c)) shows negative anomalies of the zonal wind over the western shore of Sumatra that favors upwelling and contributes to decreasing the SST, and positive anomalies over the Arabian Sea and Bay of Bengal facilitating the homogeneous increase of the SST there. Nevertheless, during this period the Indian Ocean warms rather homogeneously presenting a weak east-west SST gradient (Figure 4.9 (a)).

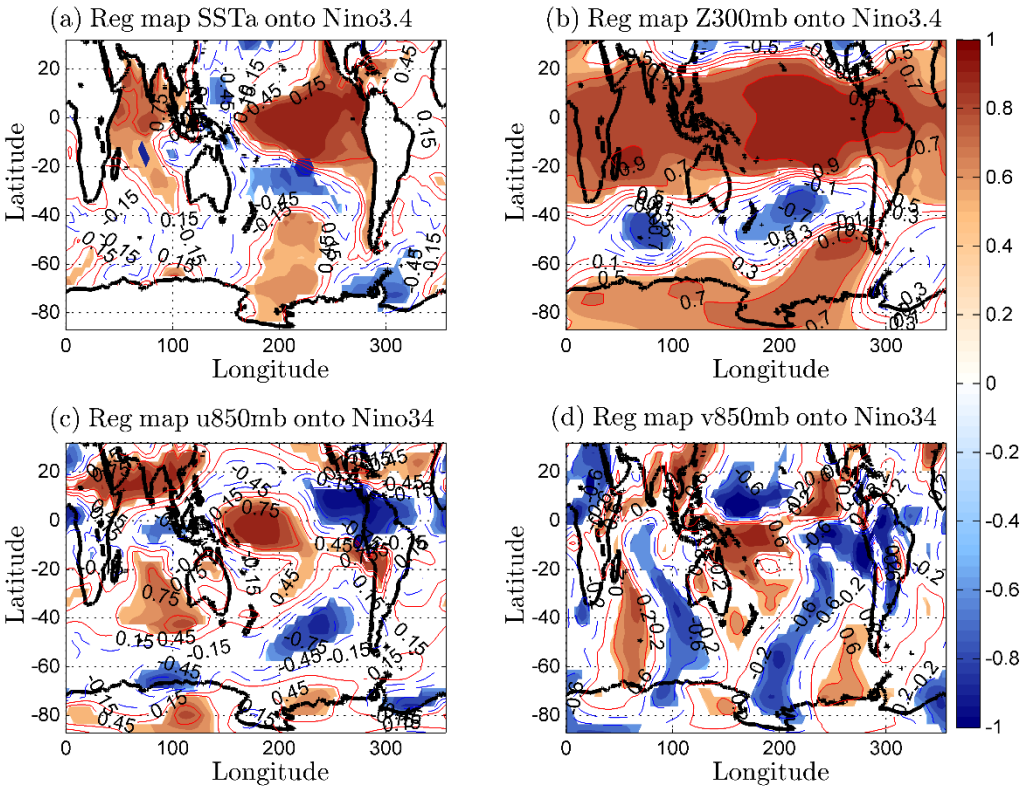

Figure 4.9. Regression map of the El Niño3.4 index (centered on SON) with: (a) SST anomalies, (b) geopotential height 300mb (Z300mb), (c) zonal wind anomalies in 850mb (u850mb) and (d) meridional wind in 850mb (v850mb). The SST, Z300mb, u850mb and v850mb are centered on OND. Second synchronization period (1966-1978). Shaded regions represent values higher than 95% confidence level for one tailed t-test. Maps computed from the ICTP-AGCM outputs.

4.5 Summary

Several studies have shown that the tropical Pacific, Atlantic and Indian oceans influence rainfall variability over Southeastern South America. Furthermore, these tropical oceans interact with each other forcing SST anomalies in remote basins through atmospheric and oceanic teleconnections. However, it is not yet clear how these SST anomalies in different basins interact together to induce austral spring rainfall variability over SESA and neither

how the interaction among the tropical oceans and their influence on rainfall variability has evolved with time. This work addresses these issues studying the collective behavior of the tropical oceans and PCP over Southeastern South America and how this behavior has evolved during the last century.

Following the methodology of Tsonis *et al*., 2007 we have constructed a network considering as nodes three oceanic indices that characterize the interannual variability of the tropical oceans (Niño3.4, IOD and TNA) as well as an index that characterizes the PCP over Southeastern South America (PCP). We studied the network's charcteristics and the collective behavior of the nodes through the detection of synchronization events considering the mean network distance as a measure of synchronization among the nodes.

We computed the network distance considering two different observed datasets (ERSSTv3b and HadSST) to guarantee that the observed synchronization events do not depend on the chosen dataset. In addition, after checking that the ICTP-AGCM reproduces well the observed behavior, we considered its output to study the global circulation anomalies that connect the different oceans and rainfall in the region of interest.

The main results of the study are as follows:

(1) Overall, we were able to show that the network distance presents interannual and interdecadal variability and could identify two synchronization periods during the last century. The first is from 1933 to 1945 ('30s) and the second covers 1966-1978 ('70s). A third potential synchronization period was detected during the '90s, but its existence depends on the correlation measure used and was not further studied.

(2) The connectivity among the nodes in the network changed with time. Whereas in the first synchronization period the nodes with significant influence on PCP in SESA were the El Niño and the TNA, in the second they were the El Niño and the IOD. Moreover, it was shown that a positive phase of the Indian Dipole and positive SST anomalies in the equatorial Pacific and tropical north Atlantic oceans induce positive SESA PCP anomalies (tables 4.5 and 4.6, Figure 4.6 (a) and (c)).

(3) ENSO is shown to influence SESA PCP variability during the two synchronization periods. The influence is such that the positive phase of ENSO induces positive rainfall anomalies over SESA and it could be understood through an increase of the northerly transport of moisture in lower-levels and the advection of cyclonic vorticity in upper-levels (in agreement with Silvesti et al., 2004, Yulaeva and Wallace, 1994 and Grimm et al., 2000).

(4) Regarding the interaction between the TNA and PCP during the '30s, it is important to note that even after the El Niño signal is removed, the TNA is significantly correlated with rainfall over SESA. This suggests that the link between TNA and PCP is direct and the SST anomalies in the TNA cannot be completely explained by ENSO forcing. The TNA could impact PCP over SESA through changes in the regional divergent circulation and northerly surface winds as proposed by Yoon and Zeng (2010). Interestingly, the standard deviation of the TNA (not shown) shows that the period of maximum value coincides with the first synchronization period. Nevertheless, regression maps onto TNA do not show significant low-level circulation anomalies, so further work is needed to elucidate the influence of the TNA on rainfall over SESA.

(5) There are two possible, not mutually exclusive ways, of interpreting the interaction between the IOD and PCP. One possibility is that the appearance of

this link is due to the fact that both nodes (IOD and PCP) are forced by El Niño. Another possibility is that the Indian Ocean warming increases rainfall over Southeastern South America through the eastward propagation of Rossby waves (in agreement Saji *et al*., 2005 and Chan *et al*., 2008).

(6) Finally, regarding the combined influence of the tropical oceans on SESA PCP during each synchronization period, we hypothesize that during the first synchronization period a warm TNA in conjunction with a warm equatorial Pacific favors a larger increase in the northerly winds that bring moisture from the Amazon toward SESA, thus further increasing rainfall there. As for the second synchronization period, we hypothesize that a Rossby wave train induced by the Indian Ocean could interact with the one forced by the tropical Pacific, so that together may favor better conditions for increased PCP over SESA through, for example, an increase in the advection of cyclonic vorticity in upper levels.

5| Effect of the future climate change on the coupling between the tropical oceans and precipitation over Southeastern South America[2]

The goal of this chapter is to investigate the possible changes in the collective behavior of the three tropical oceans and precipitation (PCP) variability over Southeastern South America (SESA) during the 21st century as consequence of an anthropogenic forcing. To address this issue, we construct a climate network following the same methodology than in section 4.2, but considering the SST and PCP output data from seven different CMIP5 models and two different scenarios of climate change.

5.1. Data and Methodology

5.1.1 Data

We consider the monthly means of SST and PCP data from all ensemble members of seven CMIP5 models (see Table 5.1). Note that the number of ensemble members depends on model and run considered. The election of the models is based on the good performance in simulating PCP over tropical South America (Yin et al., 2013) and ENSO teleconnections (Weare 2013; Langenbrunner and Neelin 2013). The horizontal

[2] Work accepted for publication in Climatic Change under the reference: Martín-Gómez V and Barreiro M (2017). Effect of the future climate change on the coupling between the tropical oceans and precipitation over Southeastern South America.

resolution of the SST and PCP fields is (1.25º x 1.25º) and (2ºx1.5º) respectively. For the PCP case, the data were interpolated from the original model grid to (2º x 1.5º) in order to better compare results from different models. SST fields were not interpolated because all of the CMIP5 models have the same spatial resolution (1.25º x 1.25º).

CMIP5-Model	**Runs**	**Ensemble size**	**Model reference**
BCC-CSM1.1	HISTORICAL	3	Xiao-Ge et al. 2013 http://forecast.bcccsm.ncc-cma.net/web/channel-43.htm
	RCP4.5	1	
	RCP8.5	1	
CCSM4	HISTORICAL	5	Gent et al. 2011
	RCP4.5	5	
	RCP8.5	6	
CSIRO-Mk3.6.0	HISTORICAL	9	Jeffrey et al. 2013 https://wiki.csiro.au/display/CSIROMk360/Home
	RCP4.5	10	
	RCP8.5	9	
GFDL-CM3	HISTORICAL	5	Delworth et al. 2006
	RCP4.5	1	
	RCP8.5	1	
HadGEM2-ES	HISTORICAL	4	Collins et al. 2011
	RCP4.5	4	
	RCP8.5	4	
IPSL-CM5A-LR	HISTORICAL	6	http://icmc.ipsl.fr/index.php/icmc-models/icmc-ipsl-cm5
	RCP4.5	4	
	RCP8.5	4	
MPI-ESM-LR	HISTORICAL	3	http://www.mpimet.mpg.de/en/science/models/mpi-esm/
	RCP4.5	3	
	RCP8.5	3	

Table 5.1 CMIP5 models used in this study to construct the climate network. SST and PCP fields considered to define the climate indices (and therefore the network) are from these seven different CMIP5 models. SST field has a horizontal resolution of (1.25ºx1.25º) in all the models. However, the spatial resolution of the PCP field depends

on the model. In order to better compare results from different models, PCP was interpolated to a new grid with a horizontal resolution of (2ºx1.5º).

For all the CMIP5 models, we consider the historical runs (20th century runs) from 1901 to 2005 in order to check whether the models reproduce the statistics of synchronization events observed during the 20th century found by Martín-Gómez and Barreiro, 2015. It is only possible to focus on the statistics of synchronization events because models generate their own internal dynamics so that simulated events will not temporally coincide with those found in observations. We also consider the RCP 4.5 and 8.5 scenarios, which covers the period from 2005 to 2100 for all the cases except for the HadGEM2-ES model, which only covers from 2005 to 2098.

Regarding observations we consider the monthly mean SST data from 1901 to 2005 of ERSSTv3b (Smith et al. 2008 and Xue et al. 2003) with resolution 2º x 2º, and the monthly mean PCP field from the GPCCv5 (Schneider et al. 2011) with a resolution of 1º x 1º.

5.1.2 Methodology

As in the previous chapter, we first define the climate indices by latitudinal and longitudinally averaging SST and PCP in the different regions considered (see Table 4.1 and Fig 4.1). We also eliminate the linear trend of the time series and compute the monthly anomalies removing the climatological cycle from 1901 to 2005 for the case of the historical run and observations, and from 2005-2100 for the 21st century runs (RCP 4.5 and 8.5) for all the models except for HadGEM2-ES. The latter we considered period 2005-2098. Finally, when defining the indices, in the case of the Indian Ocean Dipole we subtract the average between the two boxes to construct the index. All indices are normalized.

Second, we consider the same individual trimesters than in chapter 4 to construct the networks: September – November (SON) for the case of Niño3.4 index and October – December (OND) for the rest of the indices (TNA, IOD and PCP). Before taking 3-months mean and in order to avoid aliasing effects, we first apply a low-pass Lanczos Filter (Duchon 1979) with cutoff frequency of 1/12 to the monthly mean time series. Therefore, the time series have 105 values (one per year) for the case of 20th century runs, 96 values for the cases of the 21st century runs (94 for HadGEM2-ES).

Third, we construct a climate network using the mean network distance (equation 4.1) as a measure of synchronization among the network components and considering the indices computed from the output of the CMIP5 models specified on Table 5.1 (for all the runs, historical and future climate projections) and from the observations. The statistical significance of the mean network distance was computed following exactly the same methodology than in chapter 4.

After constructing the evolution of the mean network distance for each ensemble member of the models and for all the runs (historical, 21st century RCP 4.5 and 8.5 and runs), we then evaluate the skill of the models in reproducing the synchronization characteristics of the 20th century. This is done focusing on six different features of the network distance: frequency (number of synchronization periods), time lapse (model ensemble average of the total number of synchronized years considering all the synchronization years), maximum value of the network distance, minimum value of the network distance, amplitude (difference between maximum and minimum values of the network distance), and the number of links that each node has (nodes' connectivity). Physically, the amplitude of the mean network distance would measure how the degree of synchronization (or intensity of collective interaction) among the network's components changes along the century. High values of the amplitude are associated with a network in

which the intensity of collective interaction among the nodes is very variable with time. Low values of the amplitude are associated with a network in which the degree of collective interaction does not change too much with time. Note that although in latter case the collective interaction does not change too much, there could be changes in the intensity of the individual interaction between each pair of network's nodes that could counteract among them keeping constant the mean network distance.

To quantify the number of nodes' links we compute the Spearman correlation coefficients between each pair of network's nodes (Niño-TNA, Niño-PCP, Niño-IOD, TNA-PCP, IOD-PCP and TNA-IOD) for each synchronization period and check the statistical significance considering a Monte Carlo method based on the generation of 1000 surrogate time series of each index. Surrogates of each index are constructed by random permutation of nodes' time series that behave as white noise, and by random permutation taking blocks of two elements (two consecutive values of the time series) for the nodes with a red noise behavior. The criterion that establishes if two network nodes are interacting is the following: (1) We take a period ("window") that corresponds to the years in which the network distance is under the threshold level and compute all the correlation coefficients between the network's nodes. (2) Afterwards, we move the centered-window one year to the left and one year to the right, and compute again the correlation coefficients among the nodes for each moved-window. We say that two nodes are interacting if the three values of the Spearman correlation remain statistically significant.

All the aforementioned network's parameters are calculated for each ensemble member and the results represent the average of the ensemble members of each model. Finally, it must be mentioned that we only take as synchronization periods those with a number of consecutive synchronized years larger than or equal to 11. We select 11 years-length

because this is the length of the movie window we used to compute the network distance and analyze its interdecadal variability changes.

5.2 Model evaluation

In this section we show a comparison between the 20th century run of the seven CMIP5 models and the results obtained from observations. Figure 5.1 shows the mean network distance computed using the 5 different GFDL-CM3 historical runs (5 (a) to (e)) and the 20th century observations (5 (f)). Model results stress the high degree of variability in the network distance computed for just one model. Focusing on the results from observations, Figure 5 (f) shows that during the last century there were two synchronization periods with an average duration of 13 years each. Table 5.2 presents a summary of some of the observed and simulation statistics (number of synchronization periods, number of synchronized years, number of years per synchronization period, maximum and minimum value of the network distance, and the amplitude). These statistics were computed by averaging all the ensemble members. For example, table 5.2 suggests that GFDL-CM3 establishes the existence of 0.8 synchronization periods during the last century. This value was obtained averaging the 1, 0, 0 ,2 and 1 synchronization periods that presents the first, second, third, fourth and fifth historical runs (Figures 5.1 (a) to (f)).

According to Table 5.2, models capture reasonably well the minimum and maximum values of the network distance as well its amplitude. Differences are lower than 13% (8%) for the case of the maximum (minimum) network distance. The main differences between the observations and the models arise in the number of synchronization periods and number of synchronized years per century. Overall, while CCSM4 overestimates them, the rest of the CMIP5 models underestimate them. There also seem to be agreement in the mean time - length of the synchronization period. Table 5.2 shows a value of 13 years for 20th century observations, while in the models it oscillates around 9.70 years, being BCC-CSM1.1 the model closer to observations. CSIRO-Mk3.6.0 and MPI-ESM-LR do not seem to reproduce the atmospheric teleconnections during the 20th century as they

show no synchronization periods in any of the ensembles of the historical runs. If we disregard these two models, the mean simulated time-length of the synchronization periods increases from 9.70 to 13.57, suggesting a good agreement with observations. It is worth nothing that there is not one best model that reproduces most of the observed statistics. Instead, different models are closer to observations depending on the statistics considered (Table 5.2). Thus CMIP5 grand ensemble average becomes the best estimate of simulated statistics.

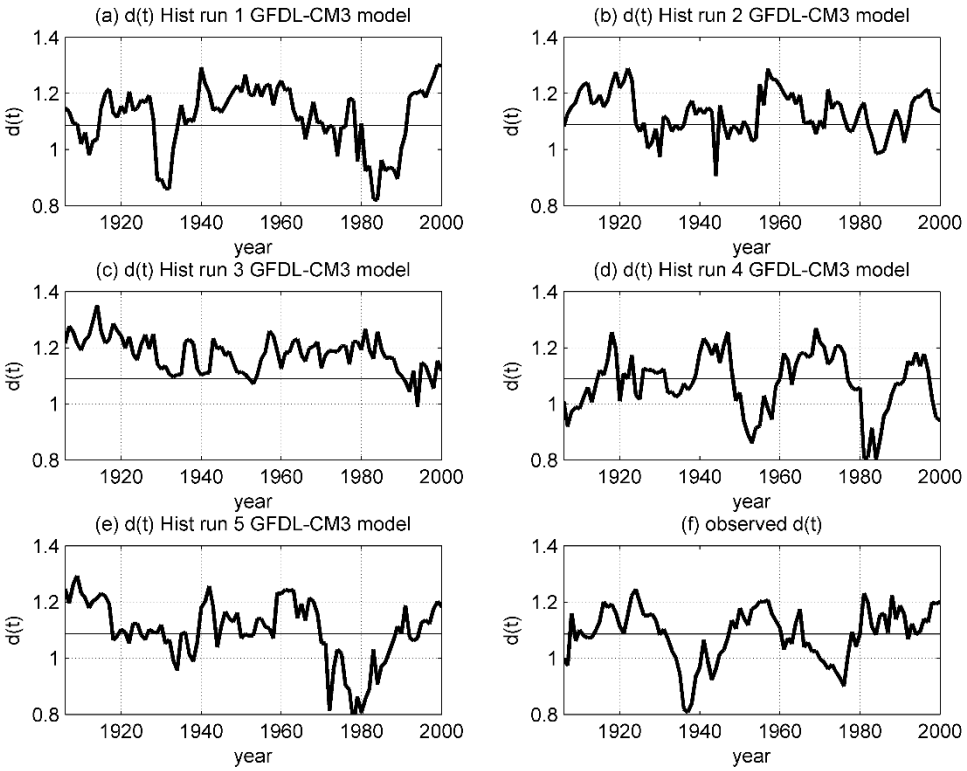

Figure 5.1 Mean network distance time series during the 20th century computed considering the first (a), second (b), third (c), forth (d) and fifth (e) historical run form GFDL-CM3 model, and the 20th century observations (SST from ERSSTv3b and PCP from GPCCv5) on figure (f). Mean network distance computed following Martín-Gómez and Barreiro, 2015. The horizontal black line represents the threshold level.

20th century	Number of synchronization periods	Number of synchronized years	Number of years per synchronization period	Minimun value network distance	Maximun value network distance	Amplitude
OBSERVATIONS	2	26	13	0.814	1.344	0.421
BCC-CSM1.1	0.33	4.33	13	0.946	1.325	0.379
CCSM4	2.80	46.20	16.50	0.725	1.230	0.504
CSIRO-Mk3.6.0	0	0	0	0.994	1.324	0.330
GFDL-CM3	0.80	11.80	14.75	0.855	1.301	0.447
HadGEM2-ES	0.50	4.80	9.6	0.912	1.297	0.385
IPSL-CM5A-LR	0.67	9.33	14	0.903	1.318	0.414
MPI-ESM-LR	0	0	0	0.980	1.320	0.339
Model closer to observations	CCSM4	GFDL-CM3	BCC-CSM1.1	GFDL-CM3	BCC-CSM1.1	IPSL-CM5A-LR
"CMIP5 models mean"	0.73	10.92	9.70	0.902	1.303	0.400

Table 5.2. Main features of the mean network distance for: observations during the 20th century (second row. Values obtained from Figure 5.1(f)), models simulations for 20th century (third to tenth rows). For the cases of the models, the value of the variables are computed considering the average of the ensemble members in order to better compare with 20th century observations.

Regarding teleconnections, Tables 5.3 and 5.4 suggest that models have a hard time reproducing with accuracy the observed teleconnections in the atmosphere during the 20th century. Most of them tend to underestimate the connectivity of the network's nodes, being CCSM4 the model closer to observations and the best at reproducing the atmospheric teleconnections of El Niño phenomenon (see table 5.4). On the other hand, CCSM4 significantly overestimates the correlation between the TNA and IOD (Table 5.3), as well the connectivity of the TNA, PCP and IOD (Table 5.4).

As a result, the grand CMIP5 ensemble mean underestimate overall the nodes connectivity (see Table 5.4). On the positive side, it represents adequately that TNA is

less connected than Niño3.4 and PCP (Table 5.4). However, on the negative side, the IOD connectivity is overestimated showing too many connections with TNA (see Table 5.3 and 5.4).

	NINO-IOD			NINO-PCP			NINO-TNA			IOD-PCP			IOD-TNA			PCP-TNA		
20th century observations	2			2			2			1			0			1		
CMIP5 Model	**H**	**RCP 4.5**	**RCP 8.5**	**H**	**RCP 4.5**	**RCP 8.5**	**H**	**RCP 4.5**	**RCP 8.5**	**H**	**RCP 4.5**	**RCP 8.5**	**H**	**RCP 4.5**	**RCP 8.5**	**H**	**RCP 4.5**	**RCP 8.5**
BCC-CSM1.1	0.33	0	0	0	0	0	0	0	0	0	0	0	0	0	0	0	0	0
CCSM4	1.20	1.80	2	2.60	2	2	1	1.20	0.83	2	1.20	1.50	1.80	1.20	1.33	1	1	0.33
CSIRO-Mk3.6.0	0	0	0	0	0.10	0	0	0	0	0	0	0	0	0	0	0	0.10	0
GFDL-CM3	0.40	2	1	0.40	3	1	0.20	1	0	0.40	2	0	0.40	2	0	0.20	1	0
HadGEM2-ES	0.25	0.25	0	0.25	0.25	0	0	0	0	0.25	0	0	0	0	0	0	0	0
IPSL-CM5A-LR	0.50	0	0.50	0.33	0.25	0.50	0.17	0	0.75	0.33	0	0	0.17	0	0.50	0	0	0.25
MPI-ESM-LR	0	0	0	0	0.33	0.33	0	0	0.33	0	0.33	1.33	0	0.33	0	0	0.33	0.67
Historical run closer to observations	CCSM4			CCSM4			CCSM4			GFDL-CM3			BCC-CSM1.1, CSIRO-Mk3.6.0 HadGEM2-ES, MPI-ESM-LR			CCSM4		
CMIP5-mean	0.38	0.58	0.50	0.51	0.84	0.55	0.20	0.31	0.27	0.43	0.51	0.41	0.34	0.51	0.26	0.17	0.35	0.18

Table 5.3. Number of link that each pair of nodes had during the 20th (in observations and in the seven CMIP5 historical runs) and 21st centuries. The number of links was computed averaging all the ensemble members that each one of the models has. H means historical run.

	NINO			TNA			PCP			IOD		
20th century observations	6			3			4			3		
CMIP5 Model	**H**	**RCP 4.5**	**RCP 8.5**	**H**	**RCP 4.5**	**RCP 8.5**	**H**	**RCP 4.5**	**RCP 8.5**	**H**	**RCP 4.5**	**RCP 8.5**
BCC-CSM1.1	0.33	0	0	0	0	0	0	0	0	0.33	0	0
CCSM4	4.80	5	4.83	3.80	3.40	2.50	5.60	4.20	3.83	5	4.20	4.83
CSIRO-Mk3.6.0	0	0.10	0	0	0.10	0	0	0.20	0	0	0	0
GFDL-CM3	1	6	2	0.80	4	0	0.80	6	1	1.20	6	1
HadGEM2-ES	0.50	0.25	0	0	0	0	0.50	0.25	0	0.50	0.25	0
IPSL-CM5A-LR	1	0.25	1.75	0.33	0	1.50	0.67	0.25	0.75	1	0	1
MPI-ESM-LR	0	0.33	1.67	0	0.67	1	0	1	3.33	0	0.67	1.33
CMIP5-mean	1.09	1.70	1.46	0.71	1.17	0.71	1.08	1.70	1.27	1.15	1.59	1.17
Historical run closer to 20th century observations	CCSM4			CCSM4			CCSM4			CCSM4		

Table 5.4. Number of links that each node presents when considering all the synchronization periods of the 20th (in observations and in the seven CMIP5 historical runs) and 21st centuries. The number of links is computed as the average of its ensemble members. H means historical run.

5.3 Changes in the network for the 21st century

In this section we first analyze the changes in the network during the 21st century under the RCP 4.5 and 8.5 scenarios of global warming and then we compare results from both climate change scenarios.

5.3.1 21st century runs under a global warming scenario RCP 4.5

Tables 5.3, 5.4 and 5.5 present a comparison of the main characteristics of the climate network for the 20th and 21st century runs considering the seven CMIP5 models' outputs. The grand CMIP5 ensemble mean suggests that the amplitude, maximum and minimum values of the mean network distance will not change significantly (see Table 5.5). On the other hand, the number of synchronized years and the mean length of synchronized periods will increase (see Table 5.5). At the individual model level, most models also

agree that the mean time-length of the synchronization periods will increase under a global warming scenario RCP 4.5. On the average, while for the 20th century run the number of years synchronized is 9.70 approximately per synchronization period, for the 21st century increases to 15.79 years (see Table 5.5).

Regarding the connectivity of the network, Table 5.3 presents the number of times that the link between two nodes appears in the network during the 20th and 21st centuries. The grand CMIP5 ensemble mean suggests an increase in the connectivity of all pairs of network's nodes as consequence of anthropogenic forcing, and therefore an increase in the connectivity of each node (Tables 5.3 and 5.4). The largest increase occurs for TNA – PCP where the number of links double. Also the link between Niño3.4 and the others three nodes of the network increase by about 50%. As result, Niño3.4 shows 50% more links in scenario RCP4.5 than in historical run. SESA PCP shows a similar increase, indicating a stronger influence of the tropical oceans, and then suggests enhanced seasonal predictability for the next decades.

Focusing on Table 5.4, at individual model level there is a large disparity regarding the connectivity increase/decrease of each network's node introducing significant uncertainty in the results. In particular, while the CMIP5-ensemble mean suggests an increase of 56% in El Niño connectivity, only 2 out of 7 models (MPI-ESM-LR and GFDL-CM3) present an increased connectivity larger than that given by the CMIP5-mean, and other 3 (IPSL-CM5A-LR, HadGEM2-ES and BCC-CCSM1.1) show decreased connectivity. Moreover, CCSM4 and CSIRO-Mk3.6.0 do not show significant changes in El Niño connectivity.

Regarding TNA, PCP and IOD indices, the CMIP5-mean depicts an increased connectivity of 65%, 57% and 38%, respectively. At individual model level, in the TNA case 2 out of 7 models (GFDL-CM3 and MPI-ESM-LR) show an increased connectivity larger than in CMIP5-mean, and two (IPSL-CM5A-LR and CCSM4) a decrease in

connectivity. The rest of the models (CSIRO- Mk3.6.0, HadGEM2-ES and BCC-CSM1.1) do not present changes in the connectivity. Similar results are seen for the PCP and IOD indices, except for HadGEM2-ES which shows decreased connectivity.

5.3.2 21st century runs under a global warming scenario RCP 8.5

Comparing RCP 8.5 climate projection and the historical run on Table 5.5, the grand CMIP5 ensemble mean suggests an increase in the number of synchronization periods and synchronized years, while the maximum and minimum values of the mean network distance do not change appreciably. Also, the mean time length of the synchronization periods is similar to that of the historical run. However, once again, the lack of agreement among the climate models regarding the increase or decrease in these variables as consequence of an anthropogenic forcing, introduce large uncertainty in the conclusions obtained from the grand CMIP5 ensemble mean.

Finally, regarding the connectivity of the network, the grand CMIP5 ensemble mean suggests an increase of the connectivity of NINO and PCP nodes while TNA and IOD do not change significantly (Table 5.4). Table 5.3 shows that NINO increases its links with all three nodes, and PCP only increases its connectivity with Niño. This, implies enhanced predictability to rainfall anomalies in SESA due to stronger connection to the equatorial Pacific. On the other hand, the connectivity of TNA and IOD do not increase because the interaction between them decreases under RCP 8.5 climate scenario (Table 5.3 and 5.4). Focusing on Table 5.4, once again, at individual model level results shows a large disparity regarding the connectivity increase/decrease of each network's node, introducing a large uncertainty in the results. In particular, El Niño connectivity in RCP8.5 increase approximately 34% in CMIP5-mean. Just 3 out of 7 models (GFDL-CM3, IPSL-CM5A-LR and MPI-ESM-LR) present an increase in El Niño connectivity larger than 34%. On the other hand, 2 out of 7 models (BCC-CSM1.1 and HadGEM2-

ES) suggest a significant decreased connectivity, while the rest of the models (CCSM4 and CSIRO-Mk3.6.0) do not suggest significant changes in El Niño connectivity under rcp8.5.

Finally, focusing on SESA PCP connectivity, only 2 out of 7 models (MPI-ESM-LR and GFDL-CM3) present an increase larger than 18% (percentage increase in CMIP5-men). CCSM4 and HadGEM2-ES show decreased connectivity, and the rest of the models (3 out of 7) do not suggest significant changes in PCP connectivity under rcp8.5.

CMIP5 Model	Number of synchronization periods			Number of synchronized years			Mean length of synchronized periods			Minimun value network distance			Maximun value network distance			Amplitude		
	H	RCP 4.5	RCP 8.5	H	RCP 4.5	RCP 8.5	H	RCP 4.5	RCP 8.5	H	RCP 4.5	RCP 8.5	H	RCP 4.5	RCP 8.5	H	RCP 4.5	RCP 8.5
BCC-CSM1.1	0.33	0	0	4.33	0	0	13	0	0	0.95	1.01	1.03	1.33	1.28	1.29	0.38	0.46	0.26
CCSM4	2.80	2	2	46.20	48.60	38.18	16.5	37	19	0.73	0.73	0.80	1.23	1.24	1.24	0.50	0.43	0.44
CSIRO-Mk3.6.0	0	0.10	0	0	1.30	0	0	13	0	0.99	1.01	0.95	1.32	1.34	1.33	0.33	0.38	0.35
GFDL-CM3	0.80	3	1	11.80	51	16	14.75	17	16	0.86	0.62	0.90	1.30	1.20	1.24	0.45	0.51	0.34
HadGEM2-ES	0.50	0.25	0	4.80	3.50	0	9.6	14	0	0.91	0.96	0.97	1.30	1.30	1.32	0.38	0.40	0.35
IPSL-CM5A-LR	0.67	0.25	1	9.33	3	1	14	12	17	0.90	0.91	0.85	1.32	1.31	1.31	0.41	0.45	0.45
MPI-ESM-LR	0	0.67	1.67	0	11.67	25.33	0	17.5	15	0.98	0.90	0.78	1.32	1.29	1.26	0.34	0.43	0.48
CMIP5-mean	0.73	0.90	0.81	10.92	17.01	13.79	9.7	15.79	9.57	0.90	0.88	0.90	1.30	1.28	1.28	0.40	0.44	0.38

Table 5.5. Main statistics of the mean network distance for 20th century model simulations (historical runs) and 21st century model simulations under RCP 4.5 and 8.5 scenarios. The value of the variables are computed considering the average of the ensemble members. H means historical run. The values for the historical runs (H) are the same as Table 5.2 and are included to facilitate comparison.

5.3.3 Comparison between the global warming scenarios.

Focusing on the grand CMIP5 ensemble mean, both global warming scenarios show an increase in the number of synchronization periods and number of synchronized years (see Table 5.5). Increases are larger for RCP4.5 than RCP8.5. They also show an increase in the nodes' connectivity with the exceptions of the TNA and IOD in RCP8.5 (see Table

5.4). The increased connectivity for the SESA PCP case would imply enhanced seasonal predictability for the next decades, being stronger for RCP 4.5 scenario than for RCP 8.5. The fact that TNA and IOD do not increase their connectivity in RCP 8.5 seems to be associated with a reduction of their interaction (see Table 5.3 and 5.4). For the case of the IOD there is also a decrease in the IOD-PCP interaction (see Table 5.3).

On the other hand, the mean time-length of the synchronization periods increases under RCP4.5 scenario, but in RCP8.5 is similar to that of the historical run (see Table 5.5). These results together with the fact that increases of the nodes' connectivity is higher for the scenario 4.5 (than 8.5), suggest a non-linear response of the atmospheric teleconnections to an increase of the GHG emissions. Atmospheric teleconnections involve dynamical mechanism like Rossby wave propagation, which in turn depends on the position of the jets and thermodynamic processes that link atmospheric warming to SST anomalies through changes in the convection (eg, Chiang and Sobel 2002). It is expected that an increase in GHG will alter both the position of the jet through modifications of the Hadley cell as well as the thermodynamic atmosphere-ocean coupling through changes in the vertical stability of the atmosphere. Ours results suggest that these teleconnections processes will strongly depend on the amount of the anthropogenic forcing through changes in the main state.

5.4 Summary and discussion.

In this work we have analyzed the possible consequences of an anthropogenic forcing over the collective oceanic influence on springtime PCP in southeastern South America using a methodology from complex networks. To do so we have used the output of seven state-of-the-art CMIP5 models (see Table 5.1).

The evaluation of the CMIP5 models during the 20th century shows that they have a hard time simulating the observed number of synchronization periods, the number of

synchronized years and the connectivity of the network's nodes. With the exception of CCSM4, the rest of the models tends to underestimate the number of synchronization periods, years of synchronization per century and nodes' connectivity. The lack of consensus among the models regarding the statistics used here to characterize the impact of the oceans on SESA PCP is likely the result of the difficulty of the models in representing adequately all atmospheric teleconnection processes probably because of biases in the main state and representation of the main modes of the ocean variability.

In spite of this inter-model discrepancy in representing 20th century observations, most of the CMIP5 models agree in the time-length of the synchronization periods, which takes values around 13.5 years (excluding CSIRO-Mk3.6.0 and MPI-ESM-LR), really close to the 13 years obtained in observations. Also, models reproduce correctly the minimum, maximum and amplitude of the network distance.

Focusing on the grand CMIP5 ensemble mean, results suggest that an anthropogenic forcing would increase the number of synchronization periods, years synchronized, and nodes' connectivity with the exception of TNA and IOD for RCP 8.5. This increment seems to be higher for the scenario RCP 4.5 than for the RCP 8.5. Latter results together with the fact that the mean time – length of a synchronization period increases under RCP4.5 but stays constant in RCP8.5, suggest a non-linear response of atmospheric teleconnections to a global warming scenario. The stronger connectivity of SESA PCP node as a consequence of anthropogenic forcing suggests enhanced seasonal predictability for the next decades due to the increase of the tropical oceanic influence on rainfall over SESA. Moreover, this increase seems to be higher under RCP4.5 than RCP8.5. TNA and IOD would decrease their connectivity under RCP 8.5 global warming scenario as consequence of the reduction of the interaction between them.

All these conclusions are suggested considering results from the grand CMIP5 ensemble mean. However, the large uncertainty associated with inter-models differences regarding the increase or reduction of the statistics under a global warming scenario makes it difficult to make robust predictions. Future studies should address the physical mechanisms through which the node's connectivity increase or decrease in individual models and its sensitivity to different radiative forcing scenarios.

6| Interdecadal changes in SESA's moisture sources and rainfall during the austral summertime[3]

The extratropical circulation anomalies generated by tropical sea surface temperatures (SST) anomalies can induce changes in the intensity and position of rainfall moisture sources. Focusing on austral summer, in this chapter we extend the network constructed previously introducing indices that characterize surface temperature variations over the Tropical South Atlantic and the equatorial Atlantic and evaluate the interdecadal changes in moisture sources over Southeastern South America (SESA).

This chapter is organized as follows: in section 6.1 we present the current state-of-the-art regarding studies on moisture sources of SESA. In section 6.2 we introduce the methodology employed to construct the climate network and to find the moisture sources of SESA. In section 6.3 we present the results regarding the synchronization among the network's components. In section 6.4 we compare moisture sources of SESA during

[3] This work has been published on Journal of climate under the reference: Martín-Gómez, V., Hernández-Garcia, E., Barreiro, M., & López, C. (2016). Interdecadal Variability of Southeastern South America Rainfall and Moisture Sources during the Austral Summertime. *Journal of Climate*, *29*(18), 6751-6763.

periods with a different degree of synchronization, and finally, in section 6.5 we summarize the main conclusions of this work.

6.1 A review of the SESA's moisture sources literature

Moisture that could lead to future precipitations (PCP) over the region can come from two different sources: (i) water vapor advection from others regions, and/or (ii) local recycling. While the advection of water vapor depends on the atmospheric circulation and can have two different origins (continental or oceanic), the recycling is the process by which evapotranspiration from a particular continental region returns as PCP to it shelf (Brubaker et al. 1993).

Previous moisture studies have focused mainly on the whole La Plata Basin (LPB) and are described below for reference. According to Martinez and Dominguez, 2014, approximately 63% of the mean PCP over LPB comes from South America and the remaining 37% comes mostly from southern Pacific and Atlantic Oceans. Studies have also shown that the main continental moisture source of LPB is the Amazon Basin (e.g., Martinez and Dominguez 2014; Zemp et al. 2014; Drumond et al. 2014; Dirmeyer et al. 2009; Berbery and Barros, 2002), contributing with 24% of the annual mean PCP over LPB (Martinez and Dominguez, 2014). Using the concept of cascading moisture recycling, which represents the moisture transport between two locations on the continent that evolves one or more re-evaporation cycles along the way, Zemp et al. 2014 showed that the southern Amazon could act not only as the main direct continental moisture source of LPB, but also as an intermediate region that distributes moisture originating from the entire Amazon basin during the wet season (December to March). The transport of the southern Amazonian moisture toward LPB takes place throughout the year, being a quasi-permanent source with a maximum during the austral summer season (Berbery and Barros, 2002; Martinez and Dominguez 2014). The transport is carried out via the

South American Low Level Jet along the Andes (Marengo 2005; Martinez and Dominguez, 2014).

Another continental type of moisture source but without advection from other regions is the local recycling. For LPB, it represents the 23.5% of its total annual mean PCP and becomes its maximum during the austral summer season due to the enhancement of the large-scale convergence and net radiation, which increases the atmospheric instability, PCP and evaporation (Martinez and Dominguez 2014).

The Atlantic and Pacific oceans are the main oceanic moisture sources of LPB and are seasonally dependent (Drumond et al. 2008; Martinez and Dominguez 2014). Drumond et al. 2008 used a Lagrangian particle dispersion model to compute the trajectories of the particles in the atmosphere backwards in time. They focused mainly on SESA and found that its main oceanic moisture sources are the southwestern South Atlantic, the tropical north Atlantic and the surrounding Atlantic Ocean located eastern to central Brazil. While the two latter remain as moisture sources throughout the year, the moisture from the tropical north Atlantic only reaches LPB during the austral summer season. This is associated with the development of a cross equatorial flow carrying moisture from the north Atlantic that penetrates into South America. Over the continent, the presence of the Andes forces the flow to become northerly, and is channeled southwards reaching LPB (Drumond et al. 2008; Martinez and Dominguez 2014; Viviane et al. 2012).

Regarding the Pacific Ocean, Martinez and Dominguez, 2014 showed that the subtropical and extratropical part of the south Pacific contributes to LPB PCP with a 7.1% of the total annual mean PCP, being its contribution more important during the austral winter.

It is well known that the atmospheric circulation is sensitive to the ocean surface conditions in the tropics. Anomalies in the SST over the tropical oceans are able to induce

changes in the meridional circulation and generate stationary Rossby waves that propagate toward extratropical latitudes, processes that induce variations in the regional circulation patterns associated to rainfall. For the particular case of SESA, several previous studies have shown that the SST anomalies in the tropical Pacific, Atlantic and Indian oceans can influence PCP variability (e.g., Seager et al. 2010; Barreiro et al., 2014; Grimm et al. 2000; Silvestri 2004; Barreiro 2010; Diaz et al. 1998 and Chan et al. 2008) and also the moisture transport (e.g., Silva et al. 2009; Martinez and Dominguez 2014; Castillo 2014).

El Niño-Southern Oscillation (ENSO) is one of the interannual variability phenomena that has been shown to influence the moisture transport from the Amazon Basin toward LPB through changes in the intensity of the SALLJ (Silva et al. 2009; Martinez and Dominguez 2014). The physical mechanism through which the positive phase of El Niño induces an increase of the moisture of Amazonian origin in LPB involves a weakening of the Walker circulation that increases anomalous subsidence over Brazil, which subsequently enhances upward motion over Southeastern South America (Andreoli and Kayano 2005). This weakening in the local Hadley circulation between tropical and subtropical South America turns into a strengthens of the southward transport of moisture in lower levels from Brazil toward SESA, which is related to a larger number of SALLJ intensification events during the positive phase of ENSO (Silva et al. 2009).

Moreover, the warm phase of this equatorial Pacific phenomenon has been shown to increase the moisture from the southern Pacific in LPB (Martinez and Dominguez 2014). Martinez and Dominguez, (2014) suggest that this could be due to the anomalous upper-level circulation pattern during the Niño events, where stronger subtropical westerlies occur together with an anomalous cyclone located over the southern Pacific along with

an anomalous anticyclone over the southern Atlantic (Andreoli and Kayano 2005; Vera et al. 2004; Ropelewski and Halpert 1987).

Finally, as it was seen on chapter 4, the tropical oceans can not only influence SESA PCP, but can also interact with each other inducing SST anomalies in remote basins through atmospheric and oceanic teleconnections (e.g., Alexander et al. 2002; Enfield and Mayer 1997; Saravannan and Chang 2000; Rodriguez-Fonseca et al. 2009). On chapter 4, we analyzed how the tropical oceans can collectively interact among them to induce rainfall variability over SESA from a complex network perspective. We constructed a climate network considering El Niño3.4, the Tropical North Atlantic, the Indian Ocean Dipole and SESA PCP as networks' nodes and focused on the detection of synchronization periods, understanding synchronization as those periods along the 20th century in which several (or in the best case all) of the networks' component were significantly interacting among them. We were able to detect two different synchronization periods with a distinct combination of tropical oceans inducing SESA PCP anomalies. We also described the possible physical mechanism through which SST anomalies in the tropical oceans could generate changes in the regional circulation over SESA and therefore, induce rainfall anomalies. Thus, the relevance of studying the synchronization periods resides in the fact that, if SESA PCP is an interactive node, the tropical oceans induce SESA PCP variability and enhance its predictability. Moreover, different periods with different degree of synchronization (for example, a synchronized period versus a non-significant synchronized period) could have associated different atmospheric circulation patterns that induce changes in the moisture sources. Here we extend the study focusing on summer season and find that there is a strong decadal variability in the impact of the oceans on SESA rainfall accompanied by large changes in moisture sources.

This study comprehends two parts: a first one in which considering the same methodology as in chapter 4, we construct a climate network in order to detect different synchronization periods among the tropical oceans and PCP over SESA. In the second part, we select two periods with different degree of synchronization and, employing a Lagrangian particle dispersion model, we analyze the spatial distribution of the moisture sources of SESA and their changes.

6.2 Data and Methodology

6.2.1 Data and methodology for constructing the climate network and detecting synchronization periods.

Here, focusing on summertime, we extend the climate network constructed on chapter 4 considering the following six different indices (see Fig. 6.1 an Table 6.1): El Niño3.4, Tropical North Atlantic (TNA), Tropical South Atlantic (TSA), Equatorial Atlantic (ATL3), Indian Ocean Dipole (IOD), and PCP over SESA (SESA PCP). The election of the indices takes into account all the tropical basins that are known to influence SESA PCP during the austral summertime. The oceanic indices are defined considering the monthly mean SST from the Extended Reconstructed Sea Surface Temperature database (ERSSTv3b; Smith et al. 2008; and Xue et al. 2003) with a resolution of 2º x 2º. The PCP index is defined using the monthly mean observed data from the GPCCv5 (Global Precipitation Climatology Center; Schneider et al. 2011) with a resolution of 1º x 1º. The period of study is 1901-2005.

The climate indices are defined by spatially averaging the SST or PCP anomalies in the respective regions (Table 6.1) within individual trimesters: September – November (SON) for the case of El Niño3.4 index and December – February (DJF) for the other indices (TNA, TSA, ATL3, IOD and PCP). The anomaly values of the indices were

computed as the deviation from the monthly climatological mean during the period (1901-2005). Therefore, our time series have 105 values, one per year. Each time series will be a node in a climate network. The lag time of 3 months among El Niño3.4 and the rest of the nodes was established in order to allow them to respond to the atmospheric anomalies generated by the equatorial Pacific.

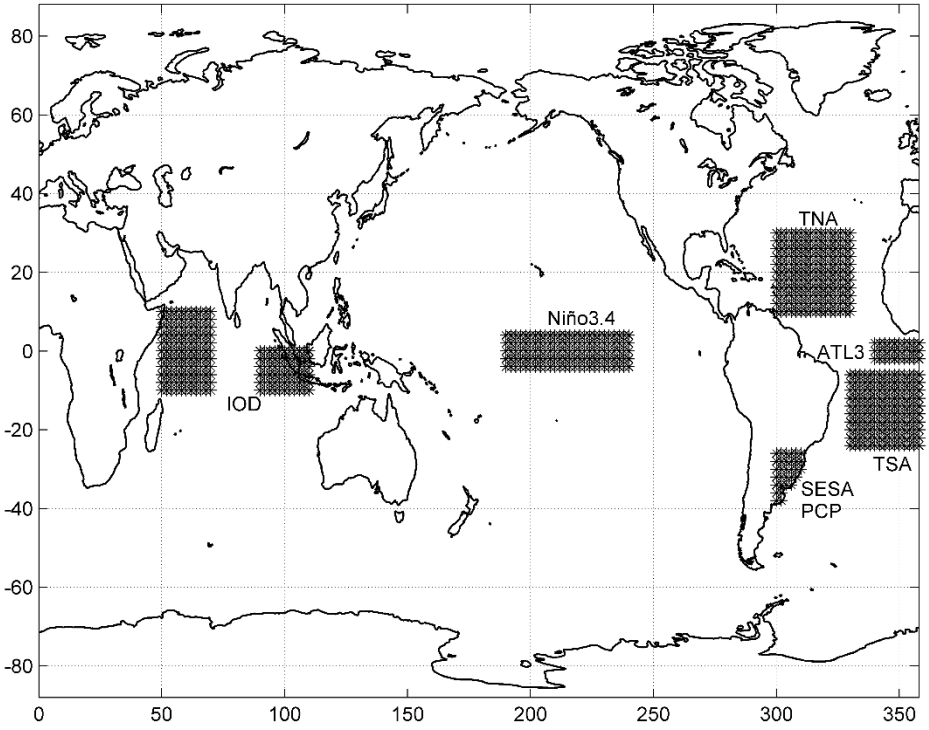

Figure 6.1. Regions that represent the spatial domain over which the SST anomalies (over the oceans) and PCP anomalies (over the continent) are averaged to define the climate indices (or network's nodes).

Index short name	Index long name	Earth's regions	
		Latitude	**Longitude**
NINO3.4	El Niño3.4 (Trenberth KE, 1997)	5ºN-5ºS	170ºW-120ºW
TNA	Tropical North Atlantic	10ºN-30ºN	60ºW-30ºW
TSA	Tropical South Atlantic	5ºS-25ºS	330ºE-358ºE
ATL3	Equatorial Atlantic (Zebiak, 1993)	3ºN-3ºS	0ºW-20ºW
IOD	Indian Ocean Dipole (Saji et al. 1999)	10ºS-10ºN 10ºS-0ºN	50ºE-70ºE 90ºE-110ºE
PCP	SESA Precipitation	25ºS-40ºS	60ºW-50ºW

Table 6.1. Geographical regions of each index that make up our network's nodes. The indices are defined considering the spectral average of the sea surface temperature (for TNA, NINO3.4, TSA, ATL3 and IOD) and precipitation (for PCP) anomalies in the specified regions. In the Indian Ocean Dipole case, the index is computed from the difference between the 2-D average SST in the west region and the 2-D average in the east region. Land areas are only considered for the case of the PCP index over SESA (PCP).

The climate network is constructed considering the Spearman correlation coefficient ρ_{ij}^{t}among each pair i,j of time series in the interval $[t-\frac{\Delta t}{2}\ ,\ t+\frac{\Delta t}{2}]$ within the mean network distance definition given by equation (4.1). The statistical significance of the mean network distance is computed following exactly the same criterion than in chapter 4. We consider that there is a statistically significant synchronization event when the mean network distance is below this threshold more than 7 consecutive years.

We also consider the monthly mean values of the vertical integral of the horizontal divergence of the moisture flux from ECMWF ERA-Interim reanalysis data, of the winds

at 850hPa and of the geopotential at 200hPa obtained from ECMWF data server (Dee et al. 2011). These fields are used to diagnose circulation anomalies and understand the changes in the moisture sources for SESA in different periods. The available data span the period 1979-to present, so to compute the anomaly values of all the products from ERA-Interim employed in this work (vertical integral of the horizontal divergence of the moisture flux, winds at 850hPa and geopotential at 200hPa), we consider the climatological mean from the common period (1979-2005).

6.2.2 Lagrangian Model and Identification of moisture sources.

To get information about the spatial distribution of the moisture sources of SESA, we consider a Lagrangian particle dispersion model (FLEXPART, Stohl et al. 2005) driven by the 6 hours forecast from Climate Forecast System Reanalysis (NCEP-CFSR, Saha et al. 2010) with a resolution of 0.5º x 0.5º during the period 1979 to 2000. We consider the NCEP-CFSR data because this reanalysis is able to reproduce correctly the lower and upper-level atmospheric circulation patterns and PCP distribution over South America during the austral summer season (Viviane et al. 2012; Quadro et al. 2013).

FLEXPART is a Lagrangian Particle dispersion model able to calculate and track the trajectories of the atmospheric moisture running forward and backward in time while dividing the atmosphere into a large number of particles (Stohl et al. 2005). Each particle represents a mass of air with a given mass (m) which is transported by the 3D wind field which includes modelled turbulence. In our work, the vertical distribution of the particles in the atmosphere is proportional to the air density and the moisture sources are computed through the net budget of evaporation minus PCP obtained from the changes in the moisture along the particles trajectories. As in Stohl and James (2004, 2005) and in Drumond et al. (2008), the steps are:

1) We select the vertical atmospheric column located over SESA (see spatial domain on table 6.1), from where we release 50.000 particles per simulation with a vertical distribution proportional to the air density. We perform 5 simulations per month (December – January – February) releasing the particles the days: 12nd, 16th, 20th, 24th and 28th of each month. All these particles are transported by FLEXPART backwards in time for 10 days and tracked recording their positions and specific humidity every 6 hours. We limit the transport of the particles to 10 days because it represents the average time that the water vapor resides in the atmosphere (Numagutti 1999). In turn, we establish a lag time between consecutive simulations of 4 days in order to assure that the obtained particle trajectories are different in consecutives simulations, since the life-time of the synoptic perturbation is around 5 days. We have checked in specific date ranges that performing daily releases instead of the selected five releases per month does not alter our results.

2) The net budget evaporation (e) minus precipitation (p) of each particle *i* with mass 'm' was computed through changes in the specific humidity (q) along its trajectory:

$$(e-p)_i = \left(m \cdot \frac{\mathrm{dq}}{d\tau}\right)_i, \quad (6.1)$$

The $(e-p)_i$ parameter was calculated for specific days. We called $(e-p)_{i,n}$ to the net budget evaporation minus PCP of the particle *i* during the *n*-th day of trajectory. Remember that we release the particles the 10th day of trajectory and run the model back in time, so for example $(e-p)_{i,1}$ will represent the net budget evaporation minus PCP of the particle *i* during the first day of trajectory, which is developed from day 10th to the day 9th. In general terms, this can be mathematically expressed as:

$$(e-p)_{i,n} = \left(m \cdot_i \frac{q_{i,\text{day}=(10-n+1)} - q_{i,\text{day}=(10-n)}}{\Delta\tau}\right) \quad (6.2)$$

where $\Delta\tau = 1\text{day}$.

3) We define a (1º x 1º) grid and per each day of trajectory, we add $(e-p)_{i,n}$ for all the particles *'i'* of the vertical column located over an area A, obtaining the net budget $(E-P)_n$ for the whole vertical column of area A in each grid point and during the *n*-th day of trajectory:

$$(E-P)_n = \frac{\sum(e-p)_{i,n}}{\sigma \cdot \text{Area}_{\text{column}}}, \quad (6.3)$$

Where σ represents the density of the water. The expression (6.3) gives the net budget as equivalent height of water per unit of time.

4) Finally, we take the average of the 10 net budgets $(E\text{-}P)_n$, and call it $(E\text{-}P)^{10}$. Per each grid cell, the parameter $(E\text{-}P)^{10}$ will represent the net budget evaporation minus PCP in the whole vertical column located over an area A (the area of the grid cell) averaged over the 10 days of trajectory of the particles going toward SESA (see equation (6.4)). The positive (negative) values of $(E\text{-}P)^{10}$ will represent the regions where particles when passing gain (loss) moisture in average over the 10 days of trajectory toward SESA, and therefore, these regions will represent sources (sinks) of moisture.

$$(E-P)^{10} = \frac{1}{10}\sum_{n=1}^{10}(E-P)_n\,, \quad (6.4)$$

6.3. Results.

6.3.1. Climate network and synchronization periods.

Figure 6.2 shows the network distance (solid black line) and the PCP index on DJF (dashed black line) during the last century. Regarding the mean network distance, the major features are:

1) The network distance is characterized by interannual and interdecadal variability.
2) During the last century there were three synchronization periods (distance smaller than the significance level): (1934-1946), (1965-1975) and (1992-2000), marked by white bands in Figure 6.2.

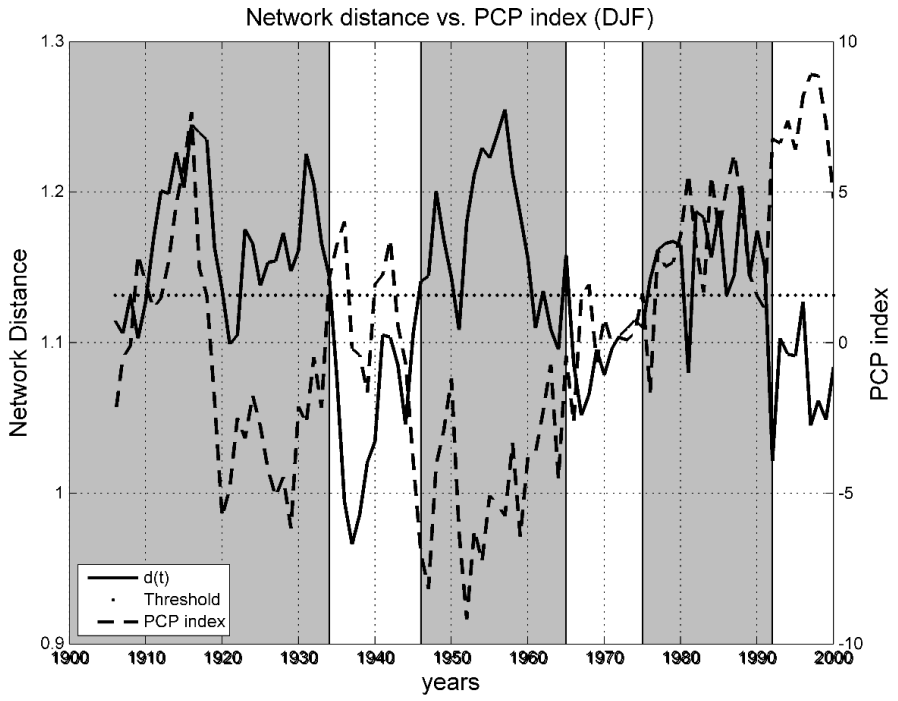

Figure 6.2. Mean network distance time series during the 20th century computed from Eq. (1) (solid black curve). To compute this time series, Niño3.4 is centered on SON (September-October-November); TNA, TSA, ATL3, IOD and PCP are centered on DJF (December-January-March). The continue black line represents the PCP index over

SESA in austral summer (DJF) and the horizontal black dot line represents the 5% significance level below which the distance identifies significant synchronization. Each point of the network distance time series represents the value of the mean network distance computed considering a sliding window of 11 years length $[t - \frac{\Delta t}{2}\ ,\ t + \frac{\Delta t}{2}]$ centered on year t.

The existence of synchronization periods indicates that several of the nodes in the network (or in the best case all) are interacting among them. However, this does not assure that during these periods the oceans are influencing rainfall over SESA. To address this question we compute the Spearman correlation coefficient between the mean network distance and a PCP index over SESA constructed taking averages of 11 years sliding windows from SESA PCP index. The resulting correlation coefficient, -0.25, is statistically significant at 5% significance level in one sided t-test (threshold level is 0.17), suggesting that an increase of the network distance (a decrease in the synchronization among the network's nodes) is associated with less PCP over SESA. The anti-correlation is evident in Figure 6.2. However, this result does not completely ensure the increment of SESA PCP as a consequence of enhancing the degree of synchronization of the network. To further address this issue we compute the Spearman correlation coefficient between the RPW and the mean network distance. The obtained value, -0.22, is statistically significant at 5% significance level in a one sided t-test, suggesting that a larger connectivity of the PCP index is associated with a smaller network distance (larger synchronization of the network). On the other hand, we also computed the correlation coefficient between the RPW and the PCP, obtaining the value 0.24, also statistically significant at 5% significance level in a one sided t-test. These results suggest that an increment of the PCP in SESA is related to a larger influence of the tropical oceans on SESA, which in turn, is associated with more degree of synchronization.

So, one could conclude that more synchronization of the network is associated with an increase of the PCP over SESA. Nevertheless, we note that there are periods in which PCP is above normal but the network does not show significant synchronization, e.g. during the decades of 1910s and 1980s.

6.3.2. Moisture sources of SESA during '80s and '90s.

Given the availability of ERA Interim and NCEP-CFSR data, we focus our discussion on the differences between the '80s (1979-1991) and '90s (1992-2000), a period of non-significant synchronization and another of statistically significant synchronization among network's components, respectively. Note that in Figure 6.2 SESA PCP anomalies were computed as its departure from the climatological mean of the period (1901-2005) obtaining positive values in both '80s and '90s decades. If we consider only period (1979-2000), the '80s have rainfall below the mean, while the '90s have rainfall above the mean in SESA.

We first analyze SST and circulation anomalies in the two periods. The Spearman correlation map between the SESA PCP index and the SST anomalies for the two periods, '80s and '90s, are shown in Figure 6.3. The shaded regions are statistically significant at 5% significance level in a MonteCarlo test based on the generation of 100 surrogate time series. The first distinctive feature between these two decades is that while in the '90s the equatorial Pacific dominates, during the '80s the equatorial Atlantic shows stronger correlation. The net value of the areal vertical integral of moisture flux divergence, $-2.66 \cdot 10^{-4}$ $kgm^{-2}s^{-2}$ ($1.29 \cdot 10^{-4}$ $kgm^{-2}s^{-2}$), is consistent with the increased (decreased) rainfall over SESA during the 90s (80s). See Figures 6.4(a) and (d).

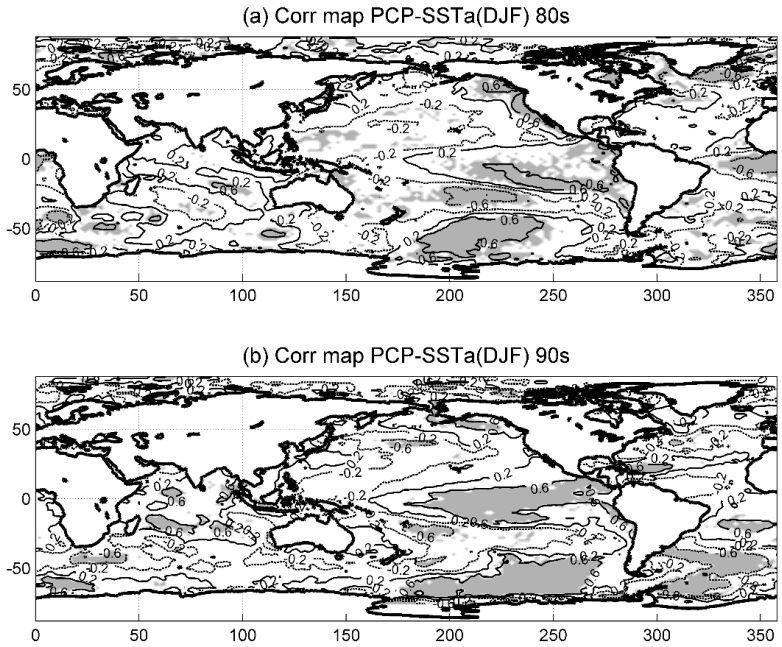

Figure 6.3. Spearman correlation maps between the PCP index over SESA and the SST anomalies centered on the austral summer season (December-January-February) for (a) '80s decade and (b) '90s decade. The anomaly values were computed considering the deviation from the climatological period (1901-2005). The colored domains represent those regions which are statistically significant at 95% significance level in a MonteCarlo test based on the generation of 100 surrogate time series. The Spearman correlation map between SST anomalies on SON and SESA PCP on DJF was also computed, but given that the same conclusions can be obtained by comparing SON and DJF figures, here we only show DJF map.

Figures 6.4 (b) and (e) show the anomalous eddy geopotential at 200mb during '80s and '90s, respectively. The '80s are characterized by an anomalous anticyclone located southeast of South America over the Atlantic Ocean and an anomalous cyclone over southern South America (Figure 6.4(b)). This situation does not favor the convergence of moisture over SESA and inhibits vertical ascent motions. However, during the '90s the

subtropical dipole of cyclonic-anticyclonic circulation anomalies in subtropical South America favors the advection of cyclonic vorticity and ascent motion over SESA, and therefore, the increase of the PCP. The low level wind anomalies are consistent with this picture, showing mainly divergence (convergence) over SESA during the 80s (90s) (see Figures 6.4(c) and (f)).

Figures 6.5 (a) and (b) represent the 10 days average of the net budget evaporation minus PCP ($(E\text{-}P)^{10}$) over the periods (1979-1991) and (1992-2000), respectively. Regions with positive (negative) values of this variable are associated with a net profit (loss) of moisture of the particles when passing by along their trajectories toward SESA, and therefore, these regions will represent the main moisture sources (sinks) of SESA. From Figures 6.5 (a) and (b) we can see that the main moisture source regions (with positive values of the $(E\text{-}P)^{10}$) are: the recycling over SESA, the central-eastern shore of Brazil together with its surrounding Atlantic ocean, and the South Atlantic Ocean surrounding SESA shore. Results are almost in agreement with Figure 1 (d) from Drummond et al., 2008. The main difference arises over the central Brazil/Amazon basin, a region that in the previously mentioned study is characterized by positive values of the $(E\text{-}P)^{10}$ budget while in our case takes negative values. The difference could be associated with the reanalysis data employed to drive the FLEXPART model: while we consider the NCEP-CFSR reanalysis, Drumond et al. (2008) employed a reanalysis from ECMWF. Other factors that can introduce differences are that the selected domain for SESA is not exactly the same and that we consider Dec-Jan-Feb, while Drumond et al., 2008 consider Jan-Feb-Mar season.

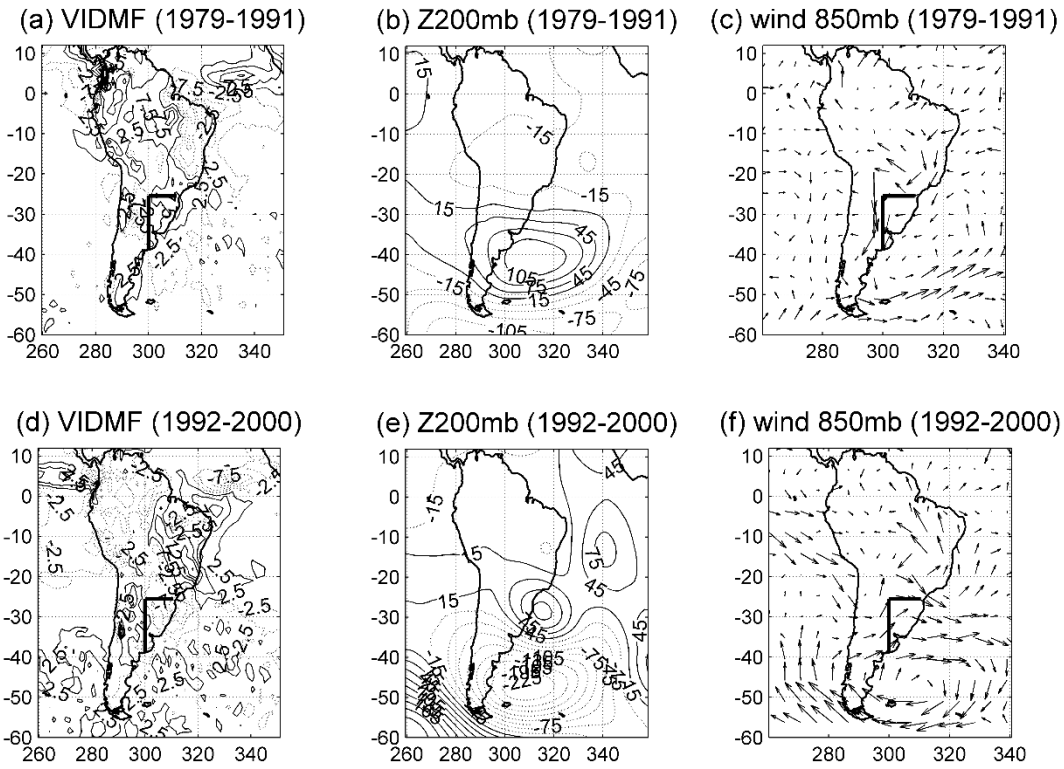

Figure 6.4. Anomaly vertical integral divergence moisture flux (VIDMF) in $kg \cdot m^{-2}s^{-2}$ (the values are divided by the scale factor 10^{-6}) for: (a) (1979-1991) and (d) (1992-2000). Anomaly eddy geopotential (Z) at 200mb in m^2s^{-2} for: (b) (1979-1991) and (e) (1992-2000). Anomaly winds at 850mb in m/s for (c) (1979-1991) and (f) (1992-2000). To compute (b) and (e) maps, we first remove the climatology of the period (1979- 2005) and apply the low-pass the Lanczos filter to the time series. After that we remove the zonal average of the geopotential at 200mb. From this anomalies values we finally select DJF season and make an average over the periods: (1979-1991) and (1992-2000). To compute the (a), (d), (c) and (f) maps we remove the climatology mean from 1979 to 2005 and apply the Lanczos filter to the time series Then we compute the DJF average for each period to obtain the anomalies. The marked region over South America represents the domain where the PCP over SESA index was defined.

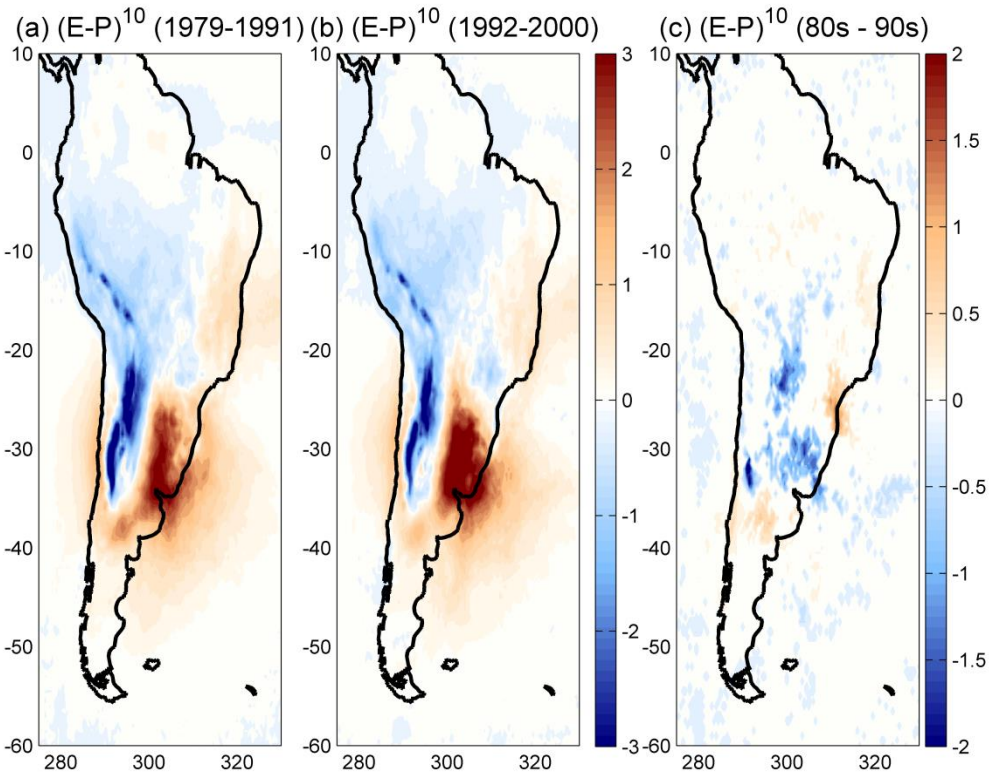

Figure 6.5. (a) 10 days average of the net budget evaporation minus precipitation ($(E-P)^{10}$) during the 80s (1979-1991) in DJF, (b) the same in the 90s (1992-2000) . (c) Difference between the 80s and 90s. Only locations with difference significant at 90% confidence level considering a Monte Carlo approach are colored. Units: mm/day

Figure 6.5 (c) shows the differences in $(E-P)^{10}$ during the 80s and 90s that are significant at 10% level. It suggests that during the 80s the central-eastern shore of Brazil acted as a stronger moisture source, while during the 90s the intensity of the recycling was larger. Moreover, during the 90s the region at 60W between 20-25S acted as a moisture source, not clearly present during the 80s. The stronger intensity of the recycling over SESA during the 90s would be in agreement with the positive PCP anomalies observed on Figure 6.2 and the anomalous vertical integral of the moisture convergence shown in Figure 6.4(d).

To interpret the changes in the moisture sources we compute the Empirical Orthogonal Functions (EOFs) for the net budget $(E-P)^{10}$. Figure 6.6 (a) shows the first EOF pattern that explains the 16.5% of the $(E-P)^{10}$ variance. Its associated principal component (PC) is plotted in Figure 6.6(b). The EOF1 pattern shows a dipole-like structure with two centers of action, one located over the central-eastern and southeast Brazil, and another one with opposite sign in the subtropical region located to the east of the Andes (20-35)ºS, (295-305)ºE. The associated PC1 shows a clear jump between both decades of study, '80s and'90s (see Figure 6.6(b)). Positive (negative) values of the PC1 tend to prevail before 1991 (after 1991) , suggesting that the center located over the central-eastern and southeast Brazil would take positive (negative) values, and therefore, the particles that pass through that region along their trajectory toward SESA will load more (less) moisture. This center of action is associated with the statistically significant positive signal observed on Figure 6.5(c) over the central-eastern and southeast Brazil. The other center of action of the EOF1 pattern has the opposite sign and could be related to the two statistically significant negative signals observed in Figure 6.5(c) over the subtropical region located to the east of the Andes. Comparing Figures 6.4(c) and (f) suggests that during the 80s the northerly anomalies along the coast of central-east and south Brazil associated with a cyclonic circulation at (15S, 50W) help the transport of moisture toward SESA. During the 90s the situation is the opposite: a low-level anti-cyclonic circulation developed over central-east Brazil that does not favor the advection of moisture from the central-east shore of Brazil toward SESA, decreasing the contribution of this region as a moisture source. Instead, it favors the transport of moisture from the Amazon basin and can explain the extension of the region acting as moisture source toward the north of SESA in that decade. Note that the development of this low-level cyclonic (anti-cyclonic) anomaly circulation over the central-east Brazil during the '80s ('90s) is, in turn,

consistent with the observed convergence anomaly of the vertical integral of moisture flux over the region shown in Figure 6.4(a) (Figure 6.4(d)).

Thus, during the 90s there is an increase in cyclonic vorticity advection in upper levels and enhanced low level convergence, resulting in a larger PCP in SESA with respect to the 80s.

We also perform the composite maps of the EOF1, the eddy geopotential high at 200mb and the low-level winds constructed as the difference between extreme-PC1-years (we take as extreme positive (negative) PC1-years those ones with standardized PC1 more (less) than 0.5 (-0.5)), and neutral years (see Figure 6.7). Results show that the circulation patterns obtained from the composite analysis (both, positive and negative extremes composite analysis) are similar to those ones shown on figures 6.4(b) and (e). There are some differences between the patterns of Figures 6.4 and 6.7 but the main spatial structures are easily distinguished and, thus, EOF1 represents well the changes observed during both decades.

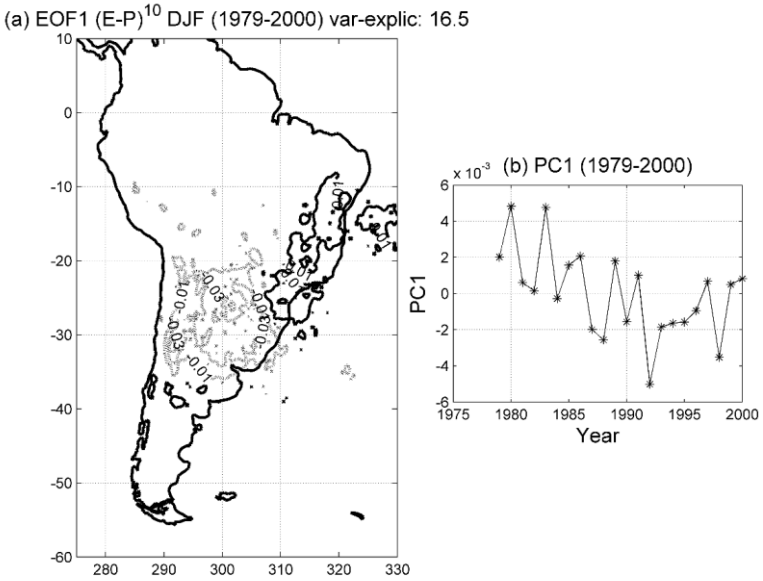

Figure 6.6. (a) First EOF of $(E-P)^{10}$ and (b) its associated PC1. Period (1979-2000).

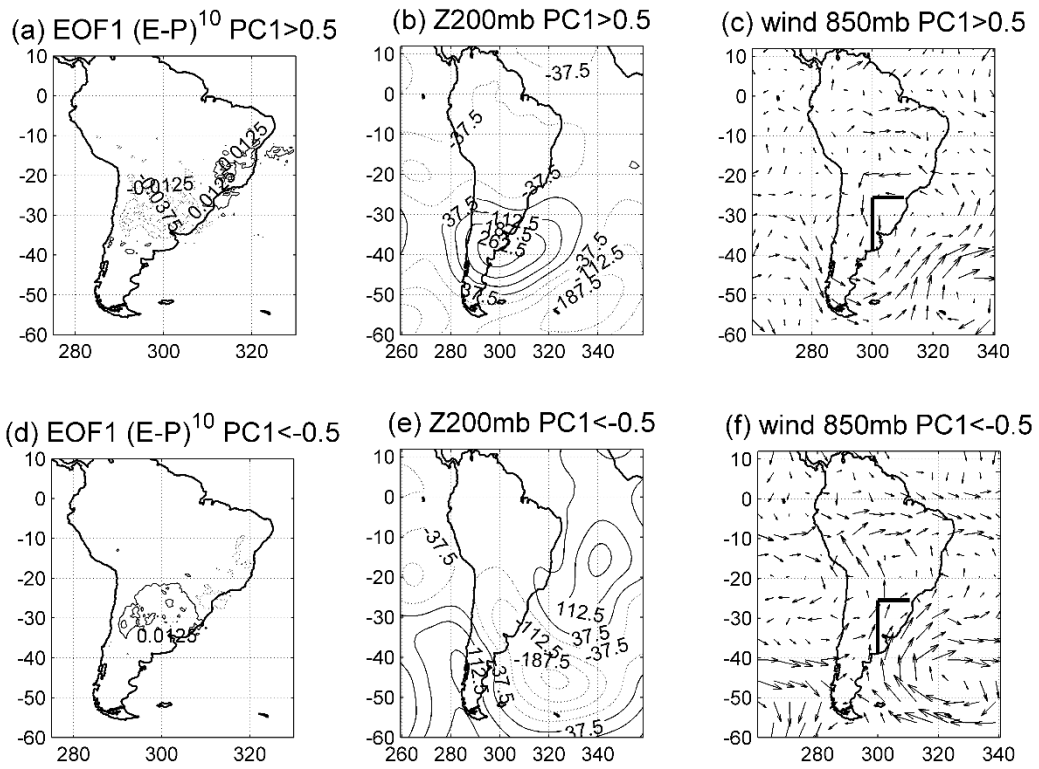

Figure 6.7. Composite maps of the EOF1 ((a) and (b)), eddy geopotential high (Z) at 200mb ((b) and (e)) and low-level winds at 850mb ((c) and (f)). Composites (a), (b) and (c) were constructed as the difference between extreme positive PC1-years (those ones with standardized PC1> 0.5) and the neutral years. Composite (d), (e) and (f) were calculated as the difference between extreme negative PC1-years (those ones with standardized PC1<-0.5) and the neutral.

6.4. Conclusions

The atmosphere is sensitive to the ocean surface conditions in the tropics in such a way that SST anomalies over the tropical oceans are able to generate quasi-stationary Rossby waves that propagate from the tropics toward extratropical latitudes inducing regional circulation anomalies that can not only induce rainfall variability, but also changes in the sources of moisture. The work reported here has two complementary parts: in the first part we construct a climate network to detect synchronization periods among the tropical

oceans and the PCP over SESA during the austral summer season. Afterwards, taking into account these results, we select two periods with different degree of synchronization to compare the spatial distribution of the moisture sources. To do so we employ a Lagrangian particle dispersion model, that allows the calculation and tracking of the trajectories of atmospheric moisture.

Results show that during the last century the network distance was characterized by interannual and interdecadal variability having three synchronization periods among the tropical oceans and the PCP over SESA, which developed during the '30s, '70s and '90s decades. The relationship between the mean network distance and the PCP over SESA is such that a larger degree of synchronization among the network's component (smaller mean network distance) is associated with an increase of the oceanic influence on SESA PCP.

We then focus on the differences between the '80s (1979-1991) and the '90s (1992-2000), one period of non-synchronization and another of statistically significant synchronization among the tropical oceans and SESA PCP. The comparison yielded the following conclusions:

1) When the synchronization of the network is statistically significant ('90s) there is convergence of moisture and favoring conditions for ascent motions over SESA, allowing an increase of the SESA PCP. The opposite conditions can be observed in the period of non-synchronization ('80s) resulting in reduced rainfall.

2) The main moisture sources of SESA are the recycling over the region, the central-eastern shore of Brazil together with its surrounding Atlantic

Ocean, and the southwestern south Atlantic surrounding the SESA domain.

3) The main differences between the two selected decades are in the intensity of the recycling, in the intensity of the central-eastern shore of Brazil and in a region centered at (20ºS, 300ºE). The latter is a moisture source for SESA only during the ‘90s and is associated with the development of a low-level anti-cyclonic anomaly circulation over central-east Brazil which favors the transport of moisture from that region toward SESA. On the other hand, during the ‘80s a low-level cyclonic anomaly circulation developed over central-east Brazil favors a stronger advection of moisture from the central-eastern shore of Brazil.

7| Summary and open questions

Sea surface temperature (SST) anomalies over the tropical oceans induce anomalous extratropical atmospheric circulation patterns that can generate changes in precipitation (PCP) over Southeastern South America (SESA) and its moisture sources. Most of the studies already existent focus on the impact that one particular basin (or the combination of two) exerts on another tropical basin and/or on SESA PCP. However, to our knowledge there are no studies which consider the interaction among the three tropical oceans and analyze: (1) how the three basins can interact with each other and, in turn, collectively induce PCP variability over SESA, (2) how this collective interaction (among the tropical oceans and SESA PCP) could change during the next century as consequence of an anthropogenic forcing, and (3) how different periods in terms of degree of synchronization among the tropical oceans and SESA PCP could induce changes in the moisture sources over SESA. Therefore, the main goal of this thesis has been to investigate the collective behavior of the three tropical oceans and SESA PCP during the extended warm season, focusing on the detection of periods when the oceans act in concert to impact rainfall over SESA (synchronized periods) and proposing associated possible physical mechanisms. Furthermore, we analyze the variability of the moisture sources over the region considering different periods in terms of the degree of synchronization.

We first focus on spring and analyzed the collective behavior of the three tropical oceans and SESA PCP during the last and the 21st centuries in order to further understand the collective interaction of the tropical oceans on SESA PCP and to determine how it could

change during the next century under different scenarios of anthropogenic forcing. We then analyze the summer season, and determine how moisture sources for PCP over SESA change for periods of different degree of synchronization.

To achieve our goals we use a new tool from complex networks that allowed to gain new insights about the collective behavior of the tropical oceans and SESA PCP (network nodes), showing that during the last century and focusing on springtime: (1) the degree of synchronization among the network's components presents large interannual and interdecadal variability, (2) there were two statistically significant synchronization periods: one over the 30s and another one over the 70s, and (3) the tropical oceans which were statistically significant interacting between each other, and in turn, influencing SESA PCP depend on the synchronized period considered. While during the 30s the tropical oceanic nodes which were interacting among them and influencing SESA PCP were TNA and Nino3.4, during the 70s they were the IOD and Nino3.4. However, several new questions arise from this analysis. On the one hand, it is not clear why synchronized periods exist. The large interdecadal variability observed in the mean network distance time series would suggest that the origin of this non-stationary behavior in the degree of synchronization could be related to multidecadal changes in the ocean mean state, and in particular with modes such as PDO or AMO. An initial analysis regarding the role of these interdecadal basin-wide climate variability modes in the behavior of the network distance was made by computing the correlation coefficient between these phenomena and the network distance obtained using the ERSSTv3b dataset. We used the monthly values of the PDO and AMO indices from 1901 to 2005 obtained from http://jisao.washington.edu/pdo/ and http://www.esrl.noaa.gov/psd/data/timeseries/AMO/, respectively. As done for the oceanic and rainfall indices, we removed the trend, computed monthly anomalies and

applied a Lanczos filter to the time series of PDO and AMO. Afterwards, we average the values of October – November – December to obtain the PDO and AMO indices 105 years long. Finally, we took a sliding window of 11 years length and calculate the average of the PDO and AMO values inside each sliding window. This procedure results in two time series (one for PDO index and another for AMO index) of 95 values which are correlated with the ERSSTv3b network distance. It was found that the behavior of the mean network distance is not significantly correlated with AMO, but it presents significant correlation with the PDO at the 95% significance level based on a Monte Carlo approach (correlation value is -0.22 and the threshold level is 0.21). This result suggests that the non-stationary behavior of the degree of synchronization among the network's components has a certain dependency with the evolution of PDO.

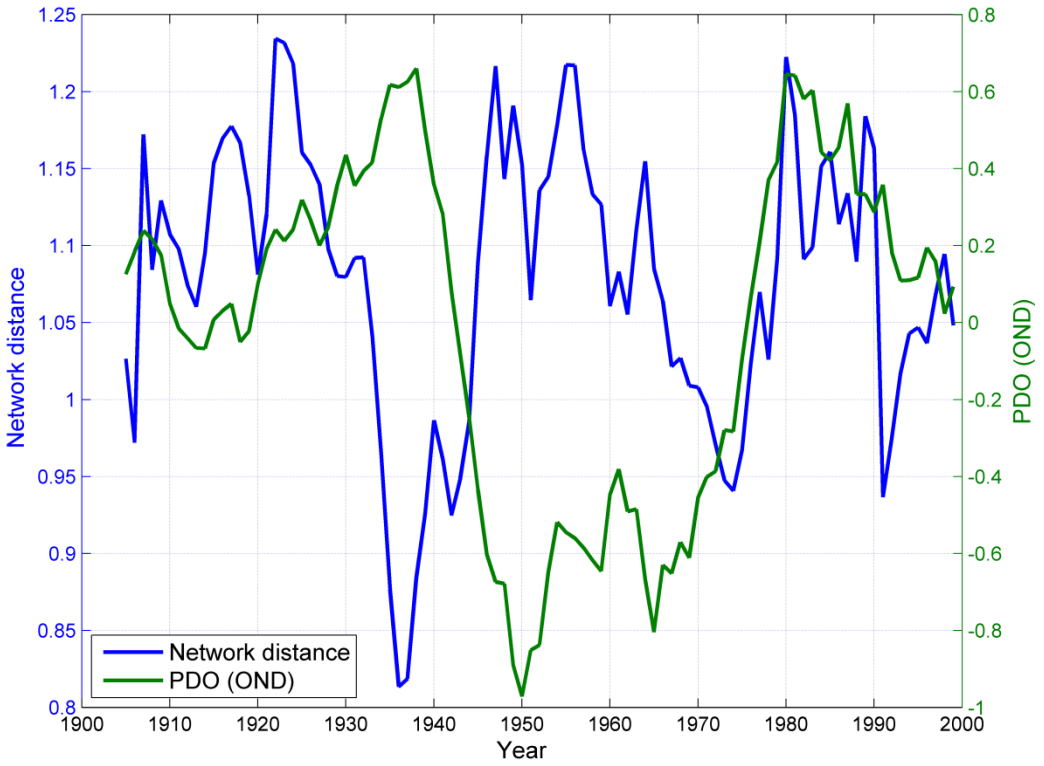

Figure 7.1. Evolution of the network distance time series computed from the observed ERSSTv3b dataset (blue line) and PDO index (green line) during the last century.

Figure 7.1 represents the mean network distance centered on OND (blue line) together with the evolution of the PDO index (green line). From visual inspection, it is possible to distinguish two distinct periods of different behavior between the PDO and the network distance: whereas before the mid-70s both time series evolved with opposite phases, after the mid-70s they evolved in phase. If we consider the first seventy years of the period, the cross-correlation between PDO and the mean network distance is -0.37, statistically significant at 95% significance level based on a Monte Carlo approach. The correlation coefficient for the last thirty years is not computed given the uncertainty in the behavior of the network distance in the '90s (Figure 4.2). Note that the first synchronization period (1933-1945) coincides with a maximum of the PDO index, while the second period does not seem to coincide with extremes in the PDO. Thus, it is not clear at this time if there are any physical mechanisms that underlie behind the interdecadal variability in the degree of synchronization among the network's components, or the oceans evolve mostly independently and synchronize with PCP by chance. Another related question is why the interacting network's nodes change from one synchronized periods to the other one. Further research is necessary to elucidate these issues.

Some these questions could be addressed through the use of climate models as one would have longer periods to analyze and better statistics. However, the CMIP5 models used in this study present a large inter-model dispersion concerning the number of synchronization periods, number of synchronized years and connectivity of the network's nodes, revealing the different behavior of oceanic and climate variability modes in each model. This makes it difficult to use only one model in this type of study to better understand the behavior during the 20th century and to get robust conclusions about the changes in the collective behavior of the tropical oceans and SESA PCP during the next century as consequence of an anthropogenic forcing. Thus, focusing on the grand CMIP5

ensemble mean, which overall behaves close to observations, results suggest that an anthropogenic forcing would increase the number of synchronization periods, years synchronized, and nodes' connectivity with the exception of TNA and IOD for RCP 8.5. This increment seems to be higher for the scenario RCP 4.5 than for the RCP 8.5. Latter results together with the fact that the mean time – length of a synchronization period increases under RCP4.5 but stays constant in RCP8.5, suggest a non-linear response of atmospheric teleconnections to a global warming scenario. The stronger connectivity of SESA PCP node as a consequence of anthropogenic forcing suggests enhanced seasonal predictability for the next decades due to the increase of the tropical oceanic influence on rainfall over SESA. These results should be taken with caution given the large uncertainty associated with inter-model differences regarding the increase or reduction of the statistics under a global warming scenario. Future studies should address the physical mechanisms through which the node's connectivity increase or decrease in individual models and its sensitivity to different radiative forcing scenarios.

Finally, focusing on summertime and taking into account that SST anomalies over the tropical oceans induce anomalous extratropical atmospheric circulation patterns that can also change the moisture sources of a particular region, we also analyzed the possible changes in the SESA's moisture source patterns associated to two different periods characterized by different degree of synchronization. We first constructed a climate network to detect synchronization periods and found that, as for springtime, the network distance shows large interdecadal variability. An initial analysis of the possible role of the interdecadal variability modes such as PDO and AMO on the non-stationary behavior of the mean network distance shows that none of both modes would be affecting the degree of synchronization, arising again the question about the origin of this non-stationary behavior. After that, we selected two periods with different degree of

synchronization (a non-synchronized period: 80s, and a synchronized period: 90s) and employed a Lagrangian particle dispersion model to calculate the spatial distribution of the moisture sources in each one of these periods. Results suggest that the main moisture sources of SESA are the recycling over the region, the central-eastern shore of Brazil together with its surrounding Atlantic Ocean, and the southwestern south Atlantic surrounding the SESA domain (in agreement with Drummond et al., 2008). In turn, the comparison of both periods suggests that when synchronization exists (90s) there is convergence of moisture and favoring conditions for ascent motions over SESA, allowing an increase of the SESA PCP. The opposite conditions can be observed in the period of non-synchronization (‘80s) resulting in reduced rainfall. Regarding moisture sources, the main differences between the two selected decades are in the intensity of the recycling, in the intensity of the central-eastern shore of Brazil and in a region centered at (20ºS, 300ºE). The latter is a moisture source for SESA only during the ‘90s and is associated with the development of a low-level anti-cyclonic anomaly circulation over central-east Brazil which favors the transport of moisture from that region toward SESA. On the other hand, during the ‘80s a low-level cyclonic anomaly circulation developed over central-east Brazil favors a stronger advection of moisture from the central-eastern shore of Brazil. Finally, as in the previous cases, one would like to know whether the changes in the main mode of variability associated with the $(E\text{-}P)^{10}$ is influenced by global modes such as PDO and AMO. A correlation analysis revealed no statistical significant correlations between the PC1 and AMO or PDO, suggesting that these two interdecadal variability modes do not seem to affect the interdecadal changes of the moisture sources. Nevertheless, due to the shortness of the time series (PC1 has only just 22 values), a further analysis would be needed to elucidate this issue.

References

Alexander M, Blade AI, Newman M, Lanzante JR, Lau NC and Scott JD (2002). The atmospheric bridge: the influence of ENSO teleconnections on air–sea interaction over the global oceans. J Climate 15:2205–2231.

Andreoli RV and Kayano MT, (2005). ENSO-related rainfall anomalies in South America and associated circulation features during warm and cold Pacific decadal oscillation regimes. International Journal of Climatology, 25(15), 2017-2030.

Allan RJ, Chambers D, Drosdowsky W, Hendon H, Latif M, Nicholls N, Smith I, Stone R, and Tourre Y, (2001). Is there an Indian Ocean dipole, and its independent of the El Niño-Southern Oscillation? Clivar Exchanges. **6**(3):18:22.

Ambrizzi T, de Souza EB and Pulwarty RS, (2004). The Hadley and Walker regional circulations and associated ENSO impacts on South American seasonal rainfall. In *The Hadley circulation: present, past and future* (pp. 203-235). Springer Netherlands.

Annamalai H, Murtugudde R, Potemra J, Xie SP, Liu P and Wang B, (2003). Coupled dynamics over the Indian Ocean: spring initiation of the zonal mode. *Deep Sea Research II:Tropical Studies in Oceanography,* **50**(12): 2305-2330.

Arizmendi F, Martí AC and Barreiro M, (2014). Evolution of atmospheric connectivity in the 20th century. *Nonlinear Processes in Geophysics*, *21*(4), 825-839.

Barreiro M, (2010). Influence of ENSO and the South Atlantic Ocean on climate predictability over Southeastern South America. *Climate dynamics*, *35*(7-8), 1493-1508.

Barreiro M, Giannini A, Chang P and Saravanan R, (2004). On the role of the South Atlantic atmospheric circulation in tropical Atlantic variability. Earth's Climate: The Ocean-Atmosphere Interaction, Geophys. Monogr, 147, 143-156.

Barreiro M and Tippmann A, (2008). Atlantic modulation of El Nino influence on summertime rainfall over Southeastern South America. *Geophysical. Research. Letters.*, ***3:*** *L16704, DOI:10.1029/2008GL035019.*

Barreiro M and Díaz N, (2011). Land–atmosphere coupling in El Niño influence over South America. *Atmospheric Science Letters*, *12*(4), 351-355.

Barreiro M, Diaz N and Remon M, (2014). Role of the oceans and land-atmosphere interaction on summertime interdecadal variability over northern Argentina. *Climate dynamics.* DOI: *10.1007/s00382-014-2088-6*

Berbery, E. H., and Barros, V. R. (2002). The hydrologic cycle of the La Plata basin in South America. *Journal of Hydrometeorology*, *3*(6), 630-645.

Bidegain M, Crisci C, del Puerto L, Inda H, Mazzeo N, Taks J, and Terra R, (2012). Clima de cambios: Nuevos desafíos de adaptación en Uruguay. *Project FAO-MGAP. TCP URU/3302 (http://www. fao. org/climatechange/80141/es/, accessed 24 April 2013)*.

Brubaker KL, Entekhabi D and Eagleson PS, (1993). Estimation of continental precipitation recycling. *Journal of Climate*, *6*(6), 1077-1089.

Camilloni IA and Barros VR, (2003). Extreme discharge events in the Parana River and their climate forcing. *Journal of Hydrololy* **278**(1): 94-106.

Campetella CM and Vera CS, (2002). The influence of the Andes mountains on the South American low-level flow. *Geophysical Research Letters*, *29*(17).

Castillo R, Nieto R, Drumond A and Gimeno L, (2014). The role of the ENSO cycle in the modulation of moisture transport from major oceanic moisture sources. Water Resources Research, 50(2), 1046-1058.

Chan SC, Behera SK and Yamagata T, (2008). Indian Ocean Dipole influence on South American rainfall. *Geophysical Research Letters* **35**(14). DOI: 10.1029/2008GL034204.

Chang P, Fang Y, Saravanan R, Ji L and Seidel H, (2006). The cause of the fragile relationship between the Pacific El Niño and the Atlantic Niño. *Nature*, **443**: 324-328. DOI:10.1038/nature05053.

Chiang JC and Sobel AH, (2002). Tropical tropospheric temperature variations caused by ENSO and their influence on the remote tropical climate. *Journal of Climate* **15:** 2616-2631.

Collins WJ, Bellouin N, Doutriaux-Boucher M, Gedney N, Halloran P, Hinton, T, et al. (2011). Development and evaluation of an Earth-system model–HadGEM2. Geoscientific Model Development, 4(4), 1051-1075.

Dee DP, Uppala SM, Simmons AJ, Berrisford P, Poli P, Kobayashi S, Andrae U, Balmaseda MA, Balsamo G, Bauer P, P.'Bechtold, Beljaars ACM, L. van de Berg, Bidlot J, Bormann N, Delsol C, Dragani R, Fuentes M, Geer AJ, Haimberger L, Healy SB, Hersbach H, Holm EV, Isaksen L, Kallberg P, Kohler M, Matricardi M, McNally AP, Monge-Sanz BM, Morcrette JJ, Park BK, Peubey C, deRosnay P, Tavolato C, Thepaut JN and Vitart F, (2011). The ERA-Interim reanalysis: Configuration and performance of the data assimilation system. *Quarterly Journal of the Royal Meteorological Society*, *137*(656), 553-597.

Delworth TL, Broccoli AJ, Rosati A, Stouffer RJ, Balaji V, Beesley JA, Durachta, JW, et al., (2006). GFDL's CM2 global coupled climate models. Part I: Formulation and simulation characteristics. Journal of Climate,19(5), 643-674.

Diaz AF, Studzinski CD and Mechoso CR, (1998). Relationships between precipitation anomalies in Uruguay and southern Brazil and sea surface temperature in the Pacific and Atlantic Oceans. *Journal of Climate*, *11*(2), 251-271.

Dirmeyer PA, Brubaker KL and DelSole T, (2009). Import and export of atmospheric water vapor between nations. *Journal of hydrology*, *365*(1), 11-22.

Dommenget D, Semenov V, and Latif M, (2006). Impacts of the tropical Indian and Atlantic Oceans on ENSO. *Geophysical Research Letters* **33**(11): L11701. DOI:10.1029/2006GL025871.

Donges JF, Zou Y, Marwan N and Kurths J, (2009). Complex networks in climate dynamics. The European Physical Journal-Special Topics, 174(1), 157-179.

Drumond A, Marengo J, Ambrizzi T, Nieto R, Moreira L, Gimeno L, (2014). The role of the Amazon Basin moisture in the atmospheric branch of the hydrological cycle: a Lagrangian analysis. *Hydrology and Earth System Sciences*, *18*(7), 2577-2598. doi:10.5194/hess-18-2577-2014

Drumond A, Nieto R, Gimeno L and Ambrizzi T, (2008). A Lagrangian identification of major sources of moisture over Central Brazil and La Plata Basin. J. Geophys. Res., 113, D14128, doi: 10.1029/2007JD009547.

Duchon CE, (1979). Lanczos Filtering in One and Two Dimensions. *Journal of Applied Meteorology*.**18:**1016–1022.

Enfield DB, (1996) Relationships of inter-American rainfall to tropical Atlantic and Pacific SST variability. *Geophysical Research Letters* **23**: 3305–3308. DOI: 10.1029/96GL03231.

Enfield DB and Mayer DA, (1997). Tropical Atlantic sea surface temperature variability and its relation to El Niño Southern Oscillation. *Journal of Geophysical Research: Oceans.* **102**: 929-945. DOI: 10.1029/96JC03296.

Figueroa, S. N., Satyamurty, P., & Da Silva Dias, P. L. (1995). Simulations of the summer circulation over the South American region with an eta coordinate model. *Journal of the atmospheric sciences*, *52*(10), 1573-1584.

Fisher AS, Terray P, Guilyardi E, Gualdi S, Delecluse P. 2005. Two Independent Tiggers for Indian Ocean Dipole Mode in a Coupled GCM. *Journal of Climate* **18**: 3428-3449.

Frauen C, Dommenget D. 2012. Influences of the tropical Indian and Atlantic Oceans on the predictability of ENSO. *Geophysical Research Letters.* **39**(2): L02276. DOI:10.1029/2011GL050520.

Gandu AW and Geisler JE, (1991). A primitive equations model study of the effect of topography on the summer circulation over tropical South America. *Journal of the atmospheric sciences*, *48*(16), 1822-1836.

Gent PR, Danabasoglu G, Donner LJ, Holland MM, Hunke EC, Jayne SR, Worley PH et al., (2011). The community climate system model version 4. *Journal of Climate*, *24*(19), 4973-4991.

Giannini A, Saravanan R and Chang P, (2004). The preconditioning role of tropical Atlantic variability in the development of the ENSO teleconnection: implications for the prediction of Nordeste rainfall. Climate Dynamics, 22(8), 839-855.

Gill A, (1980). Some simple solutions for heat-induced tropical circulation. *Quarterly Journal of the Royal Meteorological Society*, *106*(449), 447-462.

Goswami BN, Madhusoodanan MS, Neema CP and Sengupta D, (2006). A physical mechanism for North Atlantic SST influence on the Indian summer monsoon. *Geophysical Research Letters* **33**(2): L02706, DOI: 10.1029/2005GL024803.

Grimm AM, Barros VR and Doyle ME, (2000). Climate variability in Southern South America associated with El Niño and La Niña events. *Journal of Climate* **13**(1): 35-58.

Grimm AM, Pal JS and Giorgi F, (2007). Connection between spring conditions and peak summer monsoon rainfall in South America: Role of soil moisture, surface temperature, and topography in eastern Brazil. *Journal of Climate*, *20*(24), 5929-5945.

Grimm AM, (2010). Interannual climate variability in South America: impacts on seasonal precipitation, extreme events, and possible effects of climate change. *Stochastic Environmental Research and Risk Assessment*, *25*(4), 537-554.

Guo Z and Dirmeyer PA, (2013). Interannual variability of land–atmosphere coupling strength. *Journal of Hydrometeorology*, *14*(5), 1636-1646.

Guo Z, Dirmeyer PA, Koster RD, Sud YC, Bonan G, Oleson KW, McGregor JL., et al., (2006). GLACE: the global land-atmosphere coupling experiment. Part II: analysis. *Journal of Hydrometeorology*, *7*(4), 611-625.

Harzallah A, Rocha de Aragao JO and Sadourny R, (1996). Interannual rainfall variability in North-East Brazilo: Osbervation and model simulation. International Journal of climatology, **16**: 861-878.

Hidalgo C, and Taddei R, (2014). Sustainable decisions and provision of climate services to the agriculture and water sectors of southeastern South America. WCRP Conference for Latin America and the Caribbean: Developing, linking and applying climate knowledge. Montevideo, Uruguay. March 14-17.

James IN, (1995). *Introduction to circulating atmospheres*. Cambridge University Press. Chapter 8.

Jeffrey SJ, Rotstayn LD, Collier MA, Dravitzki SM, Hamalainen C, Moeseneder C, Wong KK. and Syktus JI, (2013). Australia's CMIP5 submission using the CSIRO

Mk3.6 model, Australian Meteorological and Oceanographic Journal, 63, 1–13, http://www.bom.gov.au/amoj/docs/2013/jeffrey_hres.pdf.

Junquas C, Li L, Vera CS, Le Treut H and Takahashi K, (2015). Influence of South America orography on summertime precipitation in Southeastern South America. *Climate Dynamics*, 1-23.

Kalnay E, Kanamitsu M, Kistler R, Collins W, Deaven D, Gandin L, Zhu Y, et al., (1996). The NCEP/NCAR 40-year reanalysis project. *Bulletin of the American meteorological Society*, *77*(3), 437-471.

Kodama YM, Sagawa T, Ishida S and Yoshikane T, (2012). Roles of the Brazilian Plateau in the Formation of the SACZ. *Journal of Climate*, *25*(5), 1745-1758.

Koster RD, Dirmeyer PA, Guo Z, Bonan G, Chan E, Cox P, and Liu P, et al., (2004). Regions of strong coupling between soil moisture and precipitation.*Science*, *305*(5687), 1138-1140.

Koster RD, Sud YC, Guo Z, Dirmeyer PA, Bonan G, Oleson KW, Kowalczyk E, et al., (2006). GLACE: the global land-atmosphere coupling experiment. Part I: overview. *Journal of Hydrometeorology*, *7*(4), 590-610.

Kucharski F, Molteni F, and Bracco A, (2006). Decadal interactions between the western tropical Pacific and the North Atlantic Oscillation. *Climate dynamics* **26**: 79-91.

Kucharski F, Bracco A, Yoo JH and Molteni F, (2007). Low-frequency variability of the Indian monsoon-ENSO relationship and the tropical Atlantic: The “weakening” of the 1980s and 199s. *Journal of Climate* **20**: 4225-4266.

Langenbrunner and J. David Neelin, (2013): Analyzing ENSO Teleconnections in CMIP Models as a Measure of Model Fidelity in Simulating Precipitation. J. Climate, 26, 4431-4446.

Lau NC and Nath MJ, (2004). Coupled GCM simulation of atmosphere ocean variability associated with the zonally asymmetric SST changes in the Tropical Indian Ocean. *Journal of Climate* **17**: 245-265.

Lau KM and Yang S, (2003). Walker circulation. *Encyclopedia of atmospheric sciences*, 2505-2510.

Lenters JD and Cook KH, (1997). On the origin of the Bolivian high and related circulation features of the South American climate. *Journal of the Atmospheric Sciences*, *54*(5), 656-678.

Li T, Wang B, Chang CP and Zhang Y, (2003). A Theory for the Indian Ocean Dipole-Zonal Mode. *Journal of the Atmospheric Science* **60**: 2119-2137.

Li S, Perlwitz J, Quan X and Hoerling MP, (2008). Modeling the influence of North Atlantic multidecadal warmth on the Indian summer rainfall. *Geophysical Research Letters*. **35**(5): L05804, DOI: 10.1029/2007GL032901.

Lorenz EN, (1963). Deterministic nonperiodic flow. *Journal of the atmospheric sciences*, *20*(2), 130-141.

Marengo JA, (2005). Characteristics and spatio-temporal variability of the Amazon River Basin Water Budget. *Climate Dynamics*, *24*(1), 11-22.

Marengo JA, Liebmann B, Grimm AM, Misra V, Silva Dias PL, Cavalcanti IFA. Saulo AC, et al., (2012). Recent developments on the South American monsoon system. *International Journal of Climatology*, *32*(1), 1-21.

Martín-Gómez V and Barreiro M, (2016). Analysis of oceans' influence on spring time rainfall variability over Southeastern South America during the 20th century. *International Journal of Climatology*, *36*(3), 1344-1358.

Martin-Gomez V, Hernandez-Garcia E, Barreiro M, Lopez C, (2016). Interdecadal Variability of Southeastern South America Rainfall and Moisture Sources during the Austral Summertime. *J. Climate, 29: 6751-6763.*

Martin-Gomez V and Barreiro M, (2017). Effect of future climate change on the coupling between the tropical oceans and precipitation over Southeastern South America. Climatic Change. Accepted.

Martinez JA and Dominguez F, (2014). Sources of Atmospheric Moisture for the La Plata River Basin*. *Journal of Climate*, *27*(17), 6737-6753.

Meyers G, Mcintosh P, Pigot L, and Pook M. 2007. The years of El Niño, La Niña and Interactions with the Tropical Indian Ocean. *Journal of Climate* **20**: 2872-2880.

Mo KC and Berbery EH, (2011). Drought and Persistence Wet Spells over South America Base on Observation and the U.S. CLIVAR Drought Experiments. *Journal of Climate.* **24**: 1801-1820. DOI: 10.1175/JCI3874.1

Molteni F, (2003). Atmospheric simulations using a GCM with simplified physical parameterizations. I: Model climatology and variability in multi-decadal experiments. *Climate Dynamics* **20**: 175-191.

Nobre C and Srukla J, (1996). Variations of sea surface temperature, wind stress and rainfall over the tropical Atlantic and South America. *Journal of Climate* **9**, 2464 – 2479.

Nobre P, Marengo JA, Cavalcanti IFA, Obregon G, Barros V, Camilloni I, Ferreira AG, et al., (2006). Seasonal-to-decadal predictability and prediction of South American climate. *Journal of climate*, *19*(23), 5988-6004.

Nogués-Paegle J, and Mo KC, (1997). Alternating wet and dry conditions over South America during summer. *Monthly Weather Review*, *125*(2), 279-291.

Numaguti A, (1999). Origin and recycling processes of precipitating water over the Eurasian continent: Experiments using an atmospheric general circulation model. *Journal of Geophysical Research: Atmospheres (1984–2012)*, *104*(D2), 1957-1972.

Podesta G, Letson D, Messina C, Royce, F, Ferreyra RA, Jones, J, Hansen J, Llovet I, Grondona M and O'Brien JJ, (2002). Use of ENSO-related climate information in agricultural decision making in Argentina: a pilot experience. *Agricultural Systems*, *74*(3), 371-392.

Quadro MF, Berbery EH, Dias MS, Herdies DL, Gonçalves LG, (2013). The atmospheric water cycle over South America as seen in the new generation of global reanalyses. In *AIP Conference Proceedings* (Vol. 732, pp. 732-735).

Rayner NA, Parker DE, Horton EB, Folland CK, Alexander LV, Rowell DP, Kent EC, Kaplan A, (2003). Global analyses of sea surface temperature, sea ice, and night marine air temperature since the late nineteenth century. *Journal of Geophysical. Research: Atmospheres (1984-2012)*, 108(D14). DOI: 10.1029/2002JD002670

Robertson, AW, Farrara JD, and Mechoso CR, (2003). Simulations of the atmospheric response to South Atlantic sea surface temperature anomalies. *Journal of Climate*, *16*(15), 2540-2551.

Robertson AW, and Mechoso, CR, (1998). Interannual and decadal cycles in river flows of southeastern South America. *Journal of Climate*, *11*(10), 2570-2581.

Rodriguez-Fonseca B, Polo I, Garcia-Serrano J, Losada T, Mohino E, Mechoso CR, and Kucharski F, (2009). Are Atlantic Niño enhancing Pacific ENSO events in recent decades? *Geophysical Research Letters*. **36**(20): L20705. DOI: 10.1029/2009GL040048.

Rodwell MJ, and Hoskins BJ, (2001). Subtropical anticyclones and summer monsoons. *Journal of Climate*, *14*(15), 3192-3211.

Ropelewski CF, and Halpert MS, (1987). Global and regional scale precipitation patterns associated with the El Niño/Southern Oscillation. *Monthly weather review*, *115*(8), 1606-1626.

Ruscica RC, Sörensson AA, and Menéndez CG, (2015). Pathways between soil moisture and precipitation in southeastern South America.*Atmospheric Science Letters*, *16*(3), 267-272.

Saha S, Moorthi S, Pan H, Wu X, Wang J, Nadiga S, Tripp P, Kistler R, Woollen J, Behringer D, Liu H, Stokes D, Grumbine R, Gayno G, Wang J, Hou Y, Chuang H, Juang HH, Sela J, Iredell M, Treadon R, Kleist D, Van Delst P, Keyser D, Derber J, Ek M, Meng J, Wei H, Yang R, Lord S, van den Dool H, Kumar A, Wang W, Long C, Chelliah M, Y. Xue, Huang B, Schemm J, Ebisuzaki W, Lin R, Xie P, Chen M, Zhou S, Higgins W, Zou C, Liu Q, Chen Y, Han Y, Cucurull L, Reynolds RW, Rutledge G, Goldberg M. (2010). NCEP Climate Forecast System Reanalysis (CFSR) 6-hourly Products, January 1979 to December 2010. *Research Data, The National Center for Atmospheric Research, Computational and Information Systems Laboratory, Boulder, Colo, USA*. http://dx.doi.org/10.5065/D69K487J.

Saji NH, Goswami, BN, Vinayachandra PN, Yamagata T, (1999). A dipole mode in the tropical Indian Ocean. *Nature*, **401**: 360-363.

Saji NH, Ambrizzi T, Ferraz SET, (2005). Indian Ocean Dipole mode events and austral surface air temperature anomalies. *Dynamics of Atmospheres and Oceans* **39**:87-101.

Saravanan R, and Chang P, (2000). Interaction between Tropical Atlantic Variability and El Niño – Southern Oscillation. *Journal of Climate* **13**: 2177-2194.

Satyamurty P, Nobre CA, and Dias PLS, (1998). South America. In *Meteorology of the southern hemisphere* (pp. 119-139). American Meteorological Society.

Schneider U, Becker A, Finger P, Meyer-Christoffer A, Rudolf B, Bruno Ziese M, (2011). GPCC Full Data Reanalysis Version 6.0 at 1.0: Monthly Land-Surface Precipitation from Rain-Gauges built on GTS-based and Historic Data. DOI: 10.5676/DWD_GPCC/FD_M_V6_100.

Seager R, Naik N, Baethgen W, Robertson A, Kushnir Y, Nakamura J, Jurburg S, (2010). Tropical Oceanic Causes of Interannual to Multidecadal Precipitation Variability in Southeast South America over the past Century. *Journal of Climate*. 23: 5517-5539. Doi: 10.1175/2010JCLI3578.1.

Seneviratne SI, Lüthi D, Litschi M, and Schär C. (2006). Land–atmosphere coupling and climate change in Europe. *Nature*, *443*(7108), 205-209.

Silva Dias PL, Schubert WH, and DeMaria M, (1983). Large-scale response of the tropical atmosphere to transient convection. *Journal of the Atmospheric Sciences*, *40*(11), 2689-2707.

Silva GA, Ambrizzi T, Marengo JA, (2009). Observational evidences on the modulation of the South American Low Level Jet east of the Andes according the ENSO variability. In *Annales geophysicae* 27(2), 645 – 657. Copernicus GmbH.

Silva VBS, and Kousky VE, (2012): The South American monsoon system: Climatology and variability. Modern Climatology, S.-Y. Wang, Ed., InTech, 123–152, doi:10.5772/38565.

Silvestri GE, (2004). El Niño signal variability in the precipitation over southeastern South America during the austral summer. *Geophysical Research Letters* **31**(18). DOI: 10.1029/2004GL020590.

Smith TM, Reynolds RW, Peterson TC, Lawrimore J, (2008). Improvements to NOAA's Historical Merged Land-Ocean Surface Temperature Analysis (1880-2006). *Journal of Climate.*, **21,** 2283-2296.

Sörensson AA, and Menéndez CG, (2011). Summer soil–precipitation coupling in South America. *Tellus A*, *63*(1), 56-68.

Stohl A, Forster C, Frank A, Seibert P, Wotawa G, (2005). Technical note: The Lagrangian particle dispersion model FLEXPART version 6.2. *Atmospheric Chemistry and Physics*, *5*(9), 2461-2474.

Stohl A, and James P, (2004). A Lagrangian analysis of the atmospheric branch of the global water cycle. part I: Method description, validation, and demonstration for the August 2002 flooding in central Europe, J. Hydrometeorol., 5, 656–678.

Stohl A, and James P, (2005). A Lagrangian analysis of the atmospheric branch of the global water cycle. part II: Earth's river catchments, ocean, ocean basins, and moisture transports between them, J. Hydrometeorol., 6, 961–984.

Trenberth KE, (1997). The definition of El Niño. Bull. Amer. Meteor. Soc., 78, 2771–2777, doi:10.1175/1520-0477(1997)078,2771: TDOENO.2.0.CO;2.

Trenberth Kevin, and National Center for Atmospheric Research Staff (Eds). (2016). "The Climate Data Guide: Nino SST Indices (Nino 1+2, 3, 3.4, 4; ONI and TNI)." Retrieved from https://climatedataguide.ucar.edu/climate-data/nino-sst-indices-nino-12-3-34-4-oni-and-tni.

Tsonis AA, Swanson K, and Kravtsov S. 2007. A new dynamical mechanism for major climate shifts. *Geophysical Research Letters* 34(13): L13705. DOI: 10.1029/2007GL030288.

Vera C, Silvestri G, Barros V, and Carril A, (2004). Differences in el nino response over the southern hemisphere. *Journal of climate*, *17*(9), 1741-1753.

Vera C, Higgins W, Amador J, Ambrizzi T, Garreaud R, Gochis D, Gutzler D, Lettenmaier D, Marengo J, Mechoso SR, Nogues-Peagle J, Silva Diasand PL and Zhang C, (2006). Toward a unified view of the American monsoon systems. *Journal of Climate*, *19*(20), 4977-5000.

Viviane BS, Silva and Vernon E. Kousky (2012). The South American Monsoon System: Climatology and Variability, Modern Climatology, Dr Shih-Yu Wang (Ed.), InTech, DOI: 10.5772/38565.

von Storch H, Zwiers FW, (2002). Statistical analysis in climate research.

Wang B, (1995). Interdecadal Changes in El Niño Onset in the last Four Decades. *Journal of Climate* **8**, 267-285.

Wang C, Kucharski F, Barimalala R, Bracco A, (2009). Teleconnections of the tropical Atlantic to the Indian and Pacific Oceans: A review of recent findings. *Meteologistche Zeitschrift* **18**: 445-454. DOI:10.1127/0941-2948/2009/0394.

Wang X, and Wang C, (2014). Different impacts of various El Niño events on the Indian Ocean Dipole. *Climate dynamics* **42**: 991-1005

Weare BC, (2013) El Niño teleconnections in CMIP5 models. Climate dynamics, 41(7-8), 2165-2177.

Webster PJ, (1972). Response of the tropical atmosphere to local steady forcing. *Mon. Wea. Rev*, *100*(7), 518-541.

Webster PJ, Moore AM, Loschnigg JP, Leben RP, (1999). Coupled ocean-atmosphere dynamics in the Indian Ocean during 1997-98. *Nature* **401**: 356-360.

Wu R, Kirtman BP, (2004). Understanding the impacts of the Indian Ocean on ENSO variability in a coupled GCM. *Journal of climate*, *17*(20), 4019-4031.

Xiao-Ge X, Tong-Wen W, and Jie Z, (2013). Introduction of CMIP5 experiments carried out with the climate system models of Beijing Climate Center. Advances in Climate Change Research, 4(1), 41-49.

Xue, Y, Smith TM, and Reynolds RW, (2003). Interdecadal changes of 30-yr SST normal during 1871-2000 *Journal of Climate*, **16**, 1601-1612.

Yin L, Fu R, Shevliakova E, and Dickinson RE, (2013). How well can CMIP5 simulate precipitation and its controlling processes over tropical South America?. Climate Dynamics, 41(11-12), 3127-3143.

Yoo GH, Kug JS, Park JY, and Jin FF, (2013). Sea surface temperature in the north tropical Atlantic as a trigger for El Niño/Southern Oscillation events. *Nature Geoscience* 6:112-116. Doi: 10.1038/NGEO1986.

Yoon JH, and Zeng N, (2010). An Atlantic influence on Amazon rainfall. *Climate dynamics*, *34*(2-3), 249-264.

Yulaeva E, and Wallace JM, (1994). The signature of the ENSO in global temperature precipitation fields derived from the Microwave Sounding Unit. *Journal of Climate* **7**:1719-1736.

Zebiak SE, (1993). Air-sea interaction in the equatorial Atlantic region. *Journal of Climate*, *6*(8), 1567-1586.

Zemp DC, Schleussner CF, Barbosa HMJ, Van der Ent RJ, Donges JF, Heinke J, Sampaio G, Rammig A, (2014). On the importance of cascading moisture recycling in South America. *Atmospheric Chemistry and Physics*, *14*(23), 13337-13359.

Zhou J, and Lau KM, (1998). Does a monsoon climate exist over South America?. *Journal of Climate*, *11*(5), 1020-1040.